

Accepted Manuscript

Constraints on paleofluid sources using the clumped-isotope thermometry of carbonate veins from the SAFOD (San Andreas Fault Observatory at Depth) borehole

P. Benjamin Luetkemeyer, David L. Kirschner, Katharine W. Huntington, Judith S. Chester, Frederick M. Chester, James P. Evans

PII: S0040-1951(16)30150-0
DOI: doi: [10.1016/j.tecto.2016.05.024](https://doi.org/10.1016/j.tecto.2016.05.024)
Reference: TECTO 127111

To appear in: *Tectonophysics*

Received date: 1 November 2015
Revised date: 12 May 2016
Accepted date: 12 May 2016

Please cite this article as: Luetkemeyer, P. Benjamin, Kirschner, David L., Huntington, Katharine W., Chester, Judith S., Chester, Frederick M., Evans, James P., Constraints on paleofluid sources using the clumped-isotope thermometry of carbonate veins from the SAFOD (San Andreas Fault Observatory at Depth) borehole, *Tectonophysics* (2016), doi: [10.1016/j.tecto.2016.05.024](https://doi.org/10.1016/j.tecto.2016.05.024)

This is a PDF file of an unedited manuscript that has been accepted for publication. As a service to our customers we are providing this early version of the manuscript. The manuscript will undergo copyediting, typesetting, and review of the resulting proof before it is published in its final form. Please note that during the production process errors may be discovered which could affect the content, and all legal disclaimers that apply to the journal pertain.



Constraints on paleofluid sources using the clumped-isotope thermometry of carbonate veins from the SAFOD (San Andreas Fault Observatory at Depth) borehole

P. Benjamin Luetkemeyer^a *corresponding author*

David L. Kirschner^a

Katharine W. Huntington^b

Judith S. Chester^c

Frederick M. Chester^c

James P. Evans^d

^aDepartment of Earth and Atmospheric Sciences, Saint Louis University, 205 O'Neil Hall, 3642 Lindell Blvd, Saint Louis, MO, 63108, luetkepb@slu.edu, david.kirschner@shell.com

^bDepartment of Earth and Space Sciences, Box 351310, University of Washington, Seattle, WA, 98195, kate1@uw.edu

^cDepartment of Geology and Geophysics, Texas A & M University, College Station, TX 77843, chesterj@tamu.edu, chesterf@tamu.edu

^dDepartment of Geology, Utah State University, Logan, UT, 84322-4505, james.evans@usu.edu

Keywords: SAFOD, clumped-isotope thermometry; calcite veins; fluids; faults

Abstract

The San Andreas Fault Observatory at Depth (SAFOD), near Parkfield, California, is a borehole drilled through two active deforming zones of the San Andreas fault, the Southwest Deforming Zone (SDZ) and the Central Deforming Zone (CDZ). These zones accommodate displacement by seismic slip and aseismic creep. Elevated fluid pressures and fluid-rock interactions have been proposed to explain the low apparent strength and aseismic creep observed, but the origin of the fluids and existence of high fluid pressures remains uncertain. We

use clumped-isotope thermometry and $\delta^{18}\text{O}$ - $\delta^{13}\text{C}$ compositions of calcite in veins to constrain the origin of paleofluids and compare these results to the isotopic composition of modern-day pore fluids from the SAFOD borehole and nearby areas. We observe that: (1) calcite vein temperatures vary from 81 to 134 °C, which overlaps the current ambient borehole temperatures of 110-115 °C at sampled depths; (2) vein calcite is not in carbon isotope equilibrium with modern-day pore fluids; (3) the $\delta^{18}\text{O}$ values of paleofluids close to the SDZ and CDZ, calculated from vein $\delta^{18}\text{O}$ and temperature data, are not in equilibrium with local modern-day pore waters but approach equilibrium with modern pore waters far from these zones; and (4) syntectonic vein calcite is only in C- and O-isotopic equilibrium with their host rocks within the SDZ and CDZ. Spatial patterns of $\delta^{18}\text{O}$ and $\delta^{13}\text{C}$ show little evidence for across-fault fluid-flow. Clumped isotope temperatures are consistent with locally-derived fluid sources, but not with continuous or episodic replenishment of fluids from shallow sedimentary brines or deep fluid sources. Our findings are compatible with flow of meteoric fluids from the southwestern damage zone into the SDZ and CDZ, which would have favored the formation of weak phyllosilicates and contributed to the present day weakness of the two actively deforming zones.

Keywords: SAFOD; clumped isotope thermometry; calcite veins; fluids; faults

1. Introduction

The San Andreas Fault zone (SAFZ) accommodates displacement between the Pacific and North American Plates without producing an observable heat anomaly (e.g., Lachenbruch and Sass, 1980; Fulton et al., 2004) and under stress conditions considered unfavorable for shear failure (Zoback et al., 1987; Hickman and Zoback, 2004). These observations and others are consistent with the San Andreas Fault being mechanically weak. Numerous models have been proposed to explain this apparent weakness (Byerlee, 1990; Sibson, 1992; Sleep and Blanpied,

1992; Rice, 1992; Johnson and McEvilly, 1995; Kennedy et al., 1997; Hardebeck and Hauksson, 1999; Moore and Rymer, 2007; Fulton and Saffer, 2008; Noda et al., 2009; Mittempergher et al., 2011; Richard et al., 2014).

Many explanations of weakening require that fluids are present within the SAFZ, and it is well known that fluids play a critical role in controlling the chemical and physical conditions in and around fault zones (e.g., Wintsch et al., 1995; Evans and Chester, 1995). For example, high fluid pressures can reduce the effective normal stress within a fault zone causing a decrease in fault strength (e.g., Rice, 1992, Byerlee, 1993). Fluids can act to enhance mass-transfer processes within fault zones that can lead to fault weakening or strengthening (e.g., Rutter, 1976; Gratier et al., 2011). A number of studies provide evidence that fluid-rock reactions lead to the crystallization of phyllosilicates that cannot support high shear stresses due to their low coefficients of friction (e.g., Wintsch et al., 1995; Vrolijk and van der Pluijm, 1999; Imber et al., 2008; Lockner et al., 2011; French et al., 2015). It is likely that a combination of these processes operate within the SAFZ (e.g., Holdsworth et al., 2011; Bradbury et al., 2011; Hadizadeh et al., 2012; Richard et al., 2014; Bradbury et al., 2015).

The spatial distribution and geochemical variation of carbonate veins in the SAFZ provide constraints needed to test models of fault weakening. Stable-isotope geochemistry and fluid-inclusion analyses of syn- and post-kinematic veins are routinely used in paleofluid studies to constrain the thermal conditions during vein formation, fluid origin, and changing fluid chemistry in a number of tectonic settings (e.g. Kirschner et al., 1999; Kirschner and Kennedy, 2001; Pili et al., 2002; Boles et al., 2004; Beaudoin et al., 2011; Pili et al., 2011; Evans et al., 2012; Swanson et al., 2012; Bergman et al., 2013; Huntington and Lechler, 2015). Veins often form in fracture networks that can greatly influence permeability and fluid migration,

particularly if incomplete cementation occurs (Marrett and Laubach, 1997; Laubach and Diaz-Tushman, 2009). Further, the spatial distribution of veins can be used to construct a model of the temporal variations in fluid-flow processes that could significantly influence seismic processes at depth.

The goal of this study is to determine the sources and temperatures of paleofluids that contributed to vein formation in two actively deforming zones within the San Andreas Fault (SAF) at the San Andreas Fault Observatory at Depth (SAFOD). We use conventional oxygen and carbon isotopic analyses and recently developed techniques of clumped-isotope analysis. The results provide constraints on fluid-flow models in the San Andreas Fault at seismogenic depths.

2. Background

2.1 Geologic setting of SAFOD

The SAFOD Observatory, a part of the Earthscope initiative, has provided access to rocks from the top of the seismogenic zone of the SAFZ. The SAFZ consists of a broad northwest-trending zone of deformation that accommodates right-lateral motion between the North American and Pacific tectonic plates (e.g., Titus et al., 2011). The SAFOD borehole, spudded approximately 1.8 km southwest of the surface trace of the SAFZ near the city of Parkfield, CA (Fig. 1), is located along a segment of the fault zone that exhibits both creep and microseismic-slip behavior. A vertical pilot hole was drilled to 2.2 km true vertical depth (TVD) in 2002. From the same drill pad, the main hole was drilled in three phases between 2004 and 2007. Phase 1 drilling in 2004 reached a TVD of 1.5 km along a vertical path, and then was deviated 55° to an inclined orientation of 35° towards N35°E for approximately 2.5 km TVD. Phase 2 drilling in 2005 extended the main borehole to a TVD of ~3.2 km across the geologic boundary

between the Pacific and North American Plates. Phase 3 drilling in 2007 resulted in several multilaterals being drilled through the steel casing of the main borehole at ~2.5 km depth.

During Phase 2 drilling, a 200-meter wide damage zone was defined on the basis of P-wave (V_p) and S-wave (V_s) velocities and relatively low resistivity values. This damage zone is between 3157 and 3400 meters measured depth (m MD; Fig. 1), within the Great Valley Group. Casing deformation revealed two active fault strands at 3192 and 3302 m MD, referred to as the Southwest Deforming Zone (SDZ) and Central Deforming Zone (CDZ), respectively (Zoback et al., 2010; 2011). As part of Phase 3 drilling, several multilateral cores were acquired within the arkosic sedimentary rocks and in the low velocity interval in order to sample rocks within and near the SDZ and CDZ.

2.2 Description of core and veins

The cores acquired in 2007 were cut, cleaned, photographed, logged, mapped, and sampled by several co-authors of this report. The cores are curated at the IODP's Gulf Coast Repository in College Station, Texas. Detailed geologic descriptions of the rocks and interpretations of the deformation features of the Phase 2 and Phase 3 cores have been subsequently provided in other studies (Bradbury et al., 2007; Bradbury et al., 2011; Holdsworth et al., 2011; Mittempergher et al., 2011; Rybacki et al., 2011; Gratier et al., 2011; Hadizadeh et al., 2012, and references therein). Here we provide a brief description of the units that we documented in the core samples at the well site, and later sampled for this study.

Foliated sandstone-siltstone-shale from 3186 - 3194 m MD contains thin cross-cutting vein-fill cements found primarily in irregular-shaped lenses of siltstone to very fine sandstones surrounded by foliated siltstone and shale cataclasite (Fig. A.1 and A.2, see supplementary figures in Appendix A). Carbonate within the sheared shales occurs as highly disaggregated vein

material. A sample collected at 3189 m MD by Rybacki et al. (2011) revealed the presence of several generations of cross-cutting veins interpreted to have formed as open-mode fractures with the youngest generation overprinting the fabric related to faulting. Indurated black ultracataclasite (3194.0-3196.4 m MD; Fig. A.3) is cross-cut by thin calcite veins and calcite cemented faults (e.g. at 3194.08 m MD).

An abrupt transition to brown fault gouge at the base of the black ultracataclasite unit occurs at 3196.4 m MD. The brown fault gouge is foliated, contains clasts of serpentinite, and is spatially associated with the actively creeping SDZ (3196.4-3198.1 m MD). Abundant intact calcite veins are present in a 30 cm serpentinite block within the brown gouge (Fig. A.3). The veins are oriented at both high and low angles relative to the core axis. Near the base of the serpentinite-bearing section of core, the veins are sheared and reoriented at the contact with the brown foliated fault gouge below.

The rocks from 3295.1 to 3297.1 m MD (Fig. A.4) are characterized by alternating bands of greenish-gray and more deformed reddish-brown foliated sandstones and siltstones that are crosscut by numerous small faults. Calcite veins several millimeters thick are abundant in the greenish-gray units and oriented at high angles to the overall shear foliation. Foliated brown fault gouge associated with the CDZ (3297.1-3299.1 m MD) contains porphyroclasts of serpentinite, siltstone, and sandstone. Numerous thin, short calcite veins oriented subparallel to the core axis are preserved in the serpentinite clasts. The sheared silty shale (3299.1-3301.5; Figs. A.5 and A.6), located below the CDZ, contains numerous moderately deformed calcite veins that are oriented subperpendicular to the core axis, and small cross-cutting veins within lenticular clasts of fine siltstone that do not extend into the surrounding sheared shale. Petrographic analysis of a calcite vein sampled at 3300 m MD by Rybacki et al. (2011) found irregularly shaped carbonate

veinlets coating fractured grain boundaries. Greenish-black sheared siltstone grades into relatively undeformed massive siltstone (Fig. A.6) from 3301.5 to 3303.3 m MD. Calcite cements fill small dilational jogs of shear fractures that are oriented subparallel to the core axis. A sharp, inclined contact is observed at 3303.3 m MD (Fig. A.7) that juxtaposes the relatively undeformed massive siltstone against a dark gray foliated siltstone-sandstone-shale unit extending to 3307.4 m MD. Calcite veins are preserved in clasts and thin layers of interbedded sandstone and shale. Calcite occurs as intact fracture fill oriented at intermediate angles to the core axis in more massive fine sandstone and siltstone units. Some of the most strongly deformed veins were documented within this interval at 3307 m MD by Rybacki et al. (2011). Sheared and fractured calcareous siltstone and claystone (3307.4-3311 m MD) contain intact calcite vein-fill cements preserved within clasts of siltstone. Comminuted calcite fragments are preserved within the sheared claystone layers.

2.3 Previous work: Petrography of SAFOD veins

Rybacki et al. (2011) documented multiple generations of calcite veins ranging from relatively undeformed to highly deformed. The youngest veins cross-cut the dominant fault-related fabric based on the relationships observed in four samples taken at 3141, 3189, 3300, and 3307 m MD. Homogenous yellow to orange calcite luminescence for these veins were interpreted to represent relatively fast cement precipitation from a single fluid pulse (Rybacki et al., 2011).

Mittempergher et al. (2011) documented carbonates in fractures and dilational jogs sampled within meters of the SDZ to have orientations consistent with overall right-lateral displacement of the SAF. The same study reported alternating light and dark calcite luminescence rims in stretched and elongate calcite grains that were interpreted to represent post-

fracturing changes in fluid compositions.

Holdsworth et al. (2011) in a comprehensive study of 38 thin sections of the Phase 3 core concluded that the calcite-filled veins formed just before and synchronous with the development of fault gouge. Additionally, Holdsworth et al (2011) documented an increase in veining towards the SDZ and CDZ.

2.4 Previous work: San Andreas fault gases and fluids

2.4.1 SAFOD borehole

The dominant carbon-bearing gases in the SAFOD borehole were carbon dioxide (CO₂) and methane (CH₄) (Wiersberg and Erzinger, 2008) and were present in the drilling mud throughout the drill hole (Erzinger et al., 2004; Wiersberg and Erzinger, 2008; 2011). At depths less than 770 m in the SAFOD pilot hole, the C₁/(C₂+C₃) ratios of the gases locally exceeded 2000, consistent with a biogenic origin for most, if not all, of the methane. At depths greater than 3 km, the C₁/(C₂+C₃) ratios of the hydrocarbons were lower than 10, consistent with a thermogenic origin of the methane (Wiersberg and Erzinger, 2011). The gases between approximately 770 m and 3000 m depths (MD) were of intermediate ratios and potentially mixtures of thermogenic and biogenic origin.

The δ¹³C values of the CO₂ mud gas ranged from -23 to -16 ‰ (Vienna PeeDee Belemnite, VPDB), consistent with an organic origin for the CO₂ (Wiersberg and Erzinger (2008). At present-day downhole temperatures, the isotopic values of the methane and CO₂ gases are in disequilibrium leading Wiersberg and Erzinger (2011) to propose that the gases had undergone post-formation alteration/fractionation.

Stable isotope and noble gas studies on calcite veins (Pili et al., 2002; 2011) and spring waters (Kennedy et al., 2007) sampled along the SAFZ found evidence consistent with the

involvement of fluids containing some mantle CO₂. However, the $\delta^{13}\text{C}$ values of the mud gases sampled at SAFOD ($-26 < \delta^{13}\text{C} < -13$ ‰, VPDB; Wiersberg and Erzinger, 2008) are significantly lower than $\delta^{13}\text{C}$ values typical of mantle-derived CO₂ (-7 to -4 ‰, VPDB; Wycherley et al., 1999).

2.4.2 SAF regional

Many studies have used various geochemical methods to constrain the source(s) of fluids within the SAFZ and nearby sedimentary basins (Kharaka et al., 1973; Margaritz and Taylor, 1976; Suchecki and Land, 1983; Hayes and Boles, 1993; Wood and Boles, 1991; Davisson et al., 1994; Thompson and White, 1991; Kharaka et al., 1999; Campbell et al., 2002; Pili et al., 2002, 2011; Sadofsky and Bebout, 2004; Kirby et al., 2014). The body of evidence is consistent with fluids in the fault zone having exchanged isotopes with fluids from many local and external sources.

Suchecki and Land (1983) suggested, based on the oxygen isotope compositions of calcite cements and authigenic clays in Great Valley sediments of northern California, the calcite cements precipitated from formation fluids that had been buffered by the conversion of smectite to illite during diagenesis. Kharaka and Berry (1973) concluded that the $\delta^{18}\text{O}$ -depleted waters from the Middle Miocene Temblor Formation were meteoric in origin with the isotopic compositions having been controlled by exchange with carbonate cements, whereas $\delta^{18}\text{O}$ -enriched waters were representative of the original connate water released from the underlying Mesozoic sedimentary rocks. Further, Kharaka et al. (1999) found that δD and $\delta^{18}\text{O}$ values of various spring waters emanating from seismically active strands of the SAF were consistent with meteoric fluids having circulated down to 10 km depth. Thompson and White (1991) also reported $\delta^{18}\text{O}$ values collected from wells and springs emanating from the SAFZ within the

greater Parkfield area. The wide range of fluid oxygen isotope compositions led these authors to conclude that the fluid $\delta^{18}\text{O}$ values could be attributed to a number of processes including fluid-rock interaction in deep sedimentary basins, decomposition of organic matter, and the alteration of serpentinite.

3. Methods

3.1 Sampling

Carbonate veins and host rocks were selected for the isotopic analyses of carbon and oxygen in order to: (1) compare the isotopic compositions of veins and their hosts, (2) define variations in isotopic compositions as a function of lithology and structural position with distance away from the SDZ and CDZ, (3) constrain the temperature of vein precipitation and origin of fluids, and (4) determine the extent of fluid-rock interactions across the fault zone.

Vein material for stable isotopic analysis was sampled from Phase 2 drill cuttings and the Phase 3 core. The hand-picked cuttings contained variable amounts of grey non-calcareous host rock (siltstone, shale) and white calcite vein or breccia cement. We assume that the true depth of origin of the cuttings is approximated by the measured depths. Veins from the Phase 3 cores were microdrilled with a millimeter-diameter bit.

Eighty-one cutting samples from 3185 to 3946 m (MD) were analyzed. We used the systematic variations in stable isotopic compositions in this data set to establish the context for the data acquired from the Phase 3 cores. Sixty-three vein samples from the Phase 3 cores were analyzed for $\delta^{13}\text{C}$ and $\delta^{18}\text{O}$. Sample locations, photographs, and core descriptions are in Supplementary Figures A.1- A.8, and the Petrographic Atlas of the Phase 3 cores at URL http://www.earthscope.org/samples/safod_core_samples/. Ten veins near the SDZ and serpentinite-bearing CDZ were also analyzed for clumped-isotope thermometry.

3.2 Stable isotope analysis of carbon and oxygen

Carbonate was analyzed for $\delta^{13}\text{C}$ and $\delta^{18}\text{O}$ in the stable isotope laboratory at Saint Louis University. Approximately two milligrams of material were placed in glass vials, capped, and reacted with 100 % orthophosphoric acid at 90 °C for several hours in an automated sample-prep system. The evolved CO_2 was entrained in a helium stream to a continuous-flow, Micromass Isoprime isotope-ratio mass spectrometer for analysis. The mass-45 signal of data reported in this study ranged between 3 and 10nA. The $\delta^{13}\text{C}$ and $\delta^{18}\text{O}$ data are reported in permil (‰) relative to the Vienna Pee Dee belemnite (VPDB), and calculated values of $\delta^{18}\text{O}_{\text{porewater}}$ are reported in permil (‰) against Vienna Standard Mean Ocean Water (VSMOW). An in-house standard with an accepted $\delta^{13}\text{C}_{\text{VPDB}}$ value of -2.33 ‰ and $\delta^{18}\text{O}_{\text{VSMOW}}$ value of 24.72 ‰ relative to NBS19 ($\delta^{13}\text{C}_{\text{VPDB}} = 1.95$ ‰ and $\delta^{18}\text{O}_{\text{VSMOW}} = 28.64$ ‰) was analyzed on average with every five to six samples. The results of fifty-three in-house standard analyses had a standard deviation of 0.10 ‰ and 0.09 ‰ for $\delta^{13}\text{C}$ and $\delta^{18}\text{O}$, respectively.

3.3 Clumped isotope analysis

Carbonate clumped-isotope thermometry, a technique that constrains the temperature of mineral formation independent of the isotopic composition of the fluid from which it grew, is well suited to investigate paleofluids associated with cementation and deformation in fault zones (Bergman et al., 2013; Budd et al., 2013; Huntington and Lechler, 2015; Hodson et al., this volume). Carbonate clumped-isotope thermometry is based on the degree to which heavy isotopes ^{13}C and ^{18}O bond preferentially with, or near, each other relative to the more abundant light isotopes, ^{12}C and ^{16}O (Schauble et al., 2006; Ghosh et al., 2006; Eiler, 2007; 2011; 2013; Eiler et al., 2015). This "clumping" of heavy isotopes is thermodynamically favored at lower temperatures and thus records the temperature of mineral formation (Schauble et al., 2006). To

measure the state of ordering in a mineral, the carbonate is digested in acid to produce CO₂, and the abundance of mass-47 CO₂ molecules, most of which contain both ¹³C and ¹⁸O, is measured relative to the abundance expected for a random (stochastic) distribution of isotopes among isotopologues (Ghosh et al., 2006; Eiler, 2007). This over abundance, reported as the Δ₄₇ value, is independent of the initial bulk isotopic composition of the fluid (Ghosh, 2006). Thus, the δ¹⁸O of the fluid in equilibrium with the sampled carbonates can be calculated from the measured δ¹⁸O value of the carbonate sample and the temperature obtained from clumped-isotope thermometry. Such information from clumped isotope analysis has enabled previous workers to study interactions of geologic structures, fluid flow and cementation (Swanson et al., 2012; Bergman et al., 2013; Loyd et al., 2013; Budd et al., 2013).

Clumped-isotope analyses (δ¹³C, δ¹⁸O, Δ₄₇) were carried out at the University of Washington (UW) on a subset of the samples analyzed for δ¹³C and δ¹⁸O at Saint Louis University. Calcium carbonate samples (6 to 8 mg) were digested in phosphoric acid at 90 °C for 10 minutes. The evolved CO₂ was cryogenically separated from water on an automated stainless steel vacuum line, passed through a Poropak Q trap held between -10 °C and -20 °C using helium as the carrier gas, and transferred to a Pyrex break seal tube. Carbonate standards (NBS-19 and C64 reagent-grade calcite intralaboratory standard) and CO₂ reference gases (equilibrated at 4, 60, and 1000 °C) were purified in the same manner as the samples. Break seals were loaded into an automated 10-port tube cracker inlet system and analyzed on a Thermo MAT 253 configured to measure masses 44 to 49 inclusive. Sample and reference bellows were expanded to 100 % and filled with equal pressures of sample CO₂ and UW ‘fermented corn’ reference CO₂ (δ¹³C_{PDB} = -10.2 ‰, δ¹⁸O_{VSMOW} = -6.0 ‰; values calibrated using NBS-19), respectively. The mass-47 signal was used for peak centering, and bellows were adjusted to

produce a mass-47 signal of 2550 mV (~16 V for mass-44). Pressure baseline (PBL) was automatically measured using the technique of He et al. (2012), followed by 6 acquisitions of 10 sample-reference comparison cycles with 26-second integration times. Following each sample, water was monitored by measuring m/z 18 on the same cup as m/z 45. Δ_{47} values were calculated using methods established by Affek and Eiler (2006) and Huntington et al. (2009), and reported in the absolute reference frame (Dennis et al., 2011) using heated gas (1000 °C) and CO₂-water equilibration (4 and 60 °C) lines constructed during the corresponding analysis period.

Analyses with Δ_{48} values >2 ‰ indicate potential sample contamination and therefore were excluded. Because the analytical methods used in this study are similar to the methods and 90 °C phosphoric acid temperature used by Kluge et al. (2015) and references therein, we used the 90 °C acid Kluge et al. (2015), calibration (Equation 5) to calculate temperature ($T(\Delta_{47})$) from Δ_{47} . Calculated values of $\delta^{18}\text{O}$ and $\delta^{13}\text{C}$ were made using the following fractionation factors: $\delta^{18}\text{O}_{\text{calcite-water}}$ (O'Neil et al., 1969), $\delta^{18}\text{O}_{\text{quartz-water}}$ (Kawabe, 1978), $\delta^{18}\text{O}_{\text{calcite-serpentinite}}$ (Zheng, 1993), $\delta^{13}\text{C}_{\text{calcite-CO}_2}$ (Bottinga, 1968), and $\delta^{13}\text{C}_{\text{calcite-CH}_4}$ (Bottinga, 1969).

4. Results

A total of 145 samples were analyzed from the SAFOD borehole (Table 1). The $\delta^{13}\text{C}$ and $\delta^{18}\text{O}$ values of cements collected from both Phase 2 cuttings and Phase 3 drill cores are plotted together along with host rock $\delta^{13}\text{C}$ and $\delta^{18}\text{O}$ values (Fig. 2). Veins exhibit a wide range of carbon ($\delta^{13}\text{C} = -20$ ‰ to +7 ‰) and oxygen ($\delta^{18}\text{O} = -18$ ‰ to -4 ‰) isotopic values, whereas host rock values occur in a narrower range of carbon ($\delta^{13}\text{C} = -12$ ‰ to +9 ‰) and oxygen ($\delta^{18}\text{O} = -14$ ‰ to -6 ‰) values. The isotopic composition of veins shows little variation in carbon and oxygen for any individual lithology (Fig. 2). However, vein $\delta^{13}\text{C}$ and $\delta^{18}\text{O}$ values vary with depth and proximity to lithologic, SDZ, and CDZ contacts (Fig. 3).

Table 1. Stable isotope data of cuttings from the SAFOD borehole

| ^a Depth (feet MD) | ^a Depth (meters MD) | ^b $\delta^{13}\text{C}$ (‰, VPDB) | ^c $\delta^{18}\text{O}$ (‰, VSMOW) | ^c $\delta^{18}\text{O}$ (‰, VPDB) | ^d Sample Type |
|---------------------------------|-----------------------------------|---|--|---|-----------------------------|
| 10450 | 3185 | 8.3 | 22.5 | -8.2 | wr |
| 10490 | 3197 | -0.5 | 19.2 | -11.4 | wr |
| 10510 | 3203 | -6.8 | 21.5 | -9.1 | wr |
| 10510 | 3203 | -0.9 | 16.7 | -13.8 | v |
| 10530 | 3210 | -7.7 | 21.8 | -8.8 | wr |
| 10540 | 3213 | 2.0 | 14.0 | -16.4 | v |
| 10585 | 3226 | -9.3 | 20.2 | -10.4 | v |
| 10617 | 3236 | -11.0 | 21.5 | -9.2 | v |
| 10675 | 3254 | -11.1 | 20.7 | -9.9 | v |
| 10705 | 3263 | 2.5 | 13.8 | -16.6 | v |
| 10735 | 3272 | -5.1 | 19.7 | -10.9 | v |
| 10735 | 3272 | 2.9 | 14.6 | -15.9 | v |
| 10765 | 3281 | 2.2 | 14.7 | -15.7 | v |
| 10765 | 3281 | 2.8 | 15.1 | -15.4 | v |
| 10765 | 3281 | -5.4 | 20.2 | -10.4 | v |
| 10800 | 3292 | 2.3 | 15.0 | -15.5 | v |
| 10810 | 3295 | 1.0 | 15.2 | -15.2 | v |
| 10810 | 3295 | -9.6 | 19.7 | -10.9 | v |
| 10820 | 3298 | -8.5 | 20.7 | -9.9 | v |
| 10820 | 3298 | -3.5 | 19.6 | -11.0 | v |
| 10820 | 3298 | 2.5 | 13.5 | -16.9 | v |
| 10825 | 3299 | -6.0 | 18.5 | -12.0 | v |
| 10825 | 3299 | 0.2 | 16.1 | -14.4 | v |
| 10825 | 3299 | -9.4 | 20.1 | -10.5 | v |
| 10830 | 3301 | 1.7 | 14.5 | -15.9 | v |
| 10830 | 3301 | 2.4 | 14.3 | -16.1 | v |
| 10840 | 3304 | 2.4 | 15.3 | -15.2 | v |
| 10850 | 3307 | -9.0 | 19.8 | -10.8 | v |
| 10855 | 3309 | -15.9 | 12.7 | -17.7 | v |
| 10860 | 3310 | 2.8 | 12.9 | -17.5 | v |
| 10860 | 3310 | -3.6 | 20.5 | -10.1 | wr |
| 10860 | 3310 | -10.4 | 19.7 | -10.9 | v |
| 10860 | 3310 | 2.8 | 14.2 | -16.2 | v |
| 10870 | 3313 | -4.8 | 18.6 | -11.9 | v |
| 10870 | 3313 | -8.9 | 18.6 | -12.0 | v |
| 10870 | 3313 | -4.7 | 19.0 | -11.6 | v |
| 10880 | 3316 | -4.2 | 20.2 | -10.4 | wr |
| 10880 | 3316 | -11.7 | 19.5 | -11.1 | v |
| 10894 | 3320 | -4.6 | 19.2 | -11.3 | v |

Table 1. continued

| ^a Depth (feet MD) | ^a Depth (meters MD) | ^b $\delta^{13}\text{C}$ (‰, VPDB) | ^c $\delta^{18}\text{O}$ (‰, VSMOW) | ^c $\delta^{18}\text{O}$ (‰, VPDB) | ^d Sample Type |
|---------------------------------|-----------------------------------|---|--|---|-----------------------------|
| 10900 | 3322 | -4.6 | 20.2 | -10.4 | wr |
| 10900 | 3322 | -4.2 | 19.8 | -10.8 | v |
| 10900 | 3322 | 2.7 | 14.8 | -15.6 | v |
| 10920 | 3328 | -5.7 | 17.1 | -13.4 | wr |
| 10924 | 3330 | -4.5 | 19.0 | -11.6 | v |
| 10924 | 3330 | -7.4 | 19.7 | -10.9 | v |
| 10924 | 3330 | 3.5 | 13.8 | -16.6 | v |
| 10940 | 3335 | -3.7 | 21.4 | -9.3 | wr |
| 10954 | 3339 | 2.0 | 12.9 | -17.5 | v |
| 10954 | 3339 | 0.8 | 15.2 | -15.3 | v |
| 10960 | 3341 | -2.1 | 24.3 | -6.4 | wr |
| 10960 | 3341 | -8.9 | 19.8 | -10.8 | v |
| 10980 | 3347 | -4.2 | 23.0 | -7.7 | wr |
| 11011 | 3356 | -6.8 | 18.4 | -12.2 | v |
| 11011 | 3356 | -4.6 | 18.9 | -11.7 | v |
| 11011 | 3356 | 0.4 | 15.8 | -14.7 | v |
| 11041 | 3365 | -12.6 | 26.7 | -4.0 | v |
| 11074 | 3375 | -10.3 | 21.3 | -9.3 | v |
| 11163 | 3402 | -11.5 | 23.2 | -7.5 | v |
| 11190 | 3411 | 2.6 | 14.2 | -16.2 | v |
| 11252 | 3430 | -9.2 | 20.7 | -9.9 | v |
| 11252 | 3430 | 3.0 | 13.7 | -16.7 | v |
| 11290 | 3441 | 1.0 | 14.1 | -16.3 | v |
| 11290 | 3441 | -9.8 | 20.1 | -10.5 | v |
| 11340 | 3456 | -7.5 | 18.5 | -12.0 | v |
| 11370 | 3466 | -12.6 | 19.9 | -10.7 | v |
| 11420 | 3481 | -11.8 | 23.9 | -6.8 | wr |
| 11420 | 3481 | -2.1 | 14.2 | -16.2 | v |
| 11440 | 3487 | -8.7 | 20.6 | -10.0 | wr |
| 11460 | 3493 | -9.4 | 23.0 | -7.7 | wr |
| 11480 | 3499 | -10.3 | 24.0 | -6.7 | wr |
| 11480 | 3499 | -15.3 | 20.6 | -10.0 | v |
| 11500 | 3505 | -10.5 | 17.0 | -13.5 | wr |
| 11520 | 3511 | -10.1 | 18.6 | -12.0 | wr |
| 11540 | 3517 | -11.5 | 17.8 | -12.8 | wr |
| 11540 | 3517 | -10.4 | 20.9 | -9.7 | v |
| 11640 | 3548 | -10.2 | 19.1 | -11.5 | v |
| 11850 | 3612 | 1.2 | 14.5 | -15.9 | v |
| 11947 | 3641 | 1.8 | 14.6 | -15.9 | v |

Table 1. continued

| ^a Depth (feet MD) | ^a Depth (meters MD) | ^b $\delta^{13}\text{C}$ (‰, VPDB) | ^c $\delta^{18}\text{O}$ (‰, VSMOW) | ^c $\delta^{18}\text{O}$ (‰, VPDB) | ^d Sample Type |
|---------------------------------|-----------------------------------|---|--|---|-----------------------------|
| 11947 | 3641 | 2.0 | 14.4 | -16.0 | v |
| 12050 | 3673 | -12.0 | 18.7 | -11.9 | v |
| 12050 | 3673 | -9.0 | 20.2 | -10.4 | v |
| 12145 | 3702 | 3.8 | 14.1 | -16.3 | v |
| 12245 | 3732 | -14.5 | 19.6 | -11.0 | v |
| 12245 | 3732 | -13.3 | 19.2 | -11.3 | v |
| 12346 | 3763 | -7.6 | 21.9 | -8.7 | v |
| 12346 | 3763 | -18.9 | 19.6 | -11.0 | v |
| 12464 | 3799 | -6.5 | 19.2 | -11.4 | v |
| 12464 | 3799 | -12.9 | 19.1 | -11.4 | v |
| 12464 | 3799 | -5.6 | 18.9 | -11.6 | v |
| 12546 | 3824 | -17.5 | 19.1 | -11.4 | v |
| 12546 | 3824 | -6.5 | 20.2 | -10.4 | v |
| 12645 | 3854 | -19.6 | 19.5 | -11.1 | v |
| 12846 | 3915 | 0.5 | 23.8 | -6.9 | v |
| 12846 | 3915 | -6.4 | 19.0 | -11.6 | v |
| 12945 | 3946 | 3.2 | 14.8 | -15.6 | v |
| 12945 | 3946 | -5.7 | 18.8 | -11.8 | v |

^aDepths are reported in meters measured depth (MD) for phase 2 drilling.

^b $\delta^{13}\text{C}$ values of calcite are reported in per mil relative to Vienna Peedee Belemnite (VPDB).

^c $\delta^{18}\text{O}$ values are reported in per mil relative to both VPDB and Vienna Standard Mean Ocean Water (VSMOW).

^dwr-whole rock; v-calcite vein

Veins sampled within the foliated siltstone-shale cataclasite (3186.7 to 3193.9 m MD) exhibit a narrow range of isotopic signature (blue circles: $+1.0\text{‰} < \delta^{13}\text{C} < +5\text{‰}$; $-18\text{‰} < \delta^{18}\text{O} < -13\text{‰}$; Fig.3). The two veins sampled at the base of the foliated siltstone-shale cataclasite (3193.4 m MD) and at the lithologic contact with the black ultracataclasite (at 3194.1 m MD) have $\delta^{13}\text{C}$ (+0.4 to +1 ‰) and $\delta^{18}\text{O}$ (-13 to -11 ‰) values that are intermediate between those found in the overlying foliated siltstone-shale cataclasite and the underlying black ultracataclasite (black circles: $-7\text{‰} < \delta^{13}\text{C} < +1\text{‰}$; $-12\text{‰} < \delta^{18}\text{O} < -11\text{‰}$; Fig. 3). This zone marks a shift in the isotopic signatures of veins to the lower $\delta^{13}\text{C}$ and higher $\delta^{18}\text{O}$ values typical

of the veins within the serpentinite-bearing, foliated fault gouge (3196.4 to 3198.1 m MD) that correlates with the SDZ (green circles: $-16\text{‰} < \delta^{13}\text{C} < -10\text{‰}$; $-13\text{‰} < \delta^{18}\text{O} < -10\text{‰}$; Fig. 3). The samples from the serpentinite-bearing foliated fault gouge were all taken from veins cutting the large serpentinite block and show similar isotopic signatures; however, the two veins at the upper and lower boundaries of the block (at 3196.5 and 3197.0 m MD) have $\delta^{13}\text{C}$ values $\sim 10\text{‰}$ lower than the veins sampled in the nearby black ultracataclasite and $\sim 5\text{‰}$ lower than the other veins taken from the SDZ. Veins sampled within the SDZ have similar $\delta^{13}\text{C}$ and $\delta^{18}\text{O}$ values compared to the isotopic composition of the whole rock sample ($\delta^{13}\text{C}$ of -6.8‰ and $\delta^{18}\text{O}$ of -9.1‰) collected from Phase 2 cuttings at 3203 m MD (Fig. 3).

Vein samples in the CDZ exhibit a narrow range of $\delta^{18}\text{O}$ values (-11 to -13‰), whereas the $\delta^{18}\text{O}$ values of veins sampled below the CDZ (3295 to 3310 m MD) range from -14 to -5‰ (Fig. 3). Host-rock samples from cuttings within this same interval also exhibit little variation in carbon and oxygen compositions (orange squares: $-8\text{‰} < \delta^{13}\text{C} < -6\text{‰}$; $-10\text{‰} < \delta^{18}\text{O} < -8\text{‰}$; Fig. 3). The $\delta^{13}\text{C}$ values of veins from the sheared siltstone and sandstone (295.1 to 3297.1 m MD) vary from -10 to -4‰ (Fig. 3). An abrupt shift toward heavier carbon isotopic compositions occurs within the serpentinite-bearing fault gouge of the CDZ (brown circles: $1\text{‰} < \delta^{13}\text{C} < 4\text{‰}$) at 3297 m MD continuing into the underlying sheared silty shale units (yellow circles: $1\text{‰} < \delta^{13}\text{C} < 7\text{‰}$) to 3301.4 m MD (Fig. 3). The vein carbon isotope compositions are increasingly depleted in ^{13}C away from the CDZ in the following order: massive siltstone (yellow circles: $-6\text{‰} < \delta^{13}\text{C} < -2\text{‰}$), foliated sandstone-siltstone-shale (red circles: $-9\text{‰} < \delta^{13}\text{C} < -7\text{‰}$), and sheared calcareous siltstone-claystone (Fig. 3).

Clumped-isotope data (Table 2) from samples between 3196.7 and 3309.9 m MD yield Δ_{47} values of 0.486 to 0.620 ‰ (average analytical uncertainties of 0.021 ‰, 1 standard error

Table 2. Stable and clumped isotope data of calcite veins from SAFOD borehole phase 3 multilateral cores.

| Sample ID ^a | Depth ^b (meters, MD) | $\delta^{13}\text{C}^c$ (‰, VPDB) | $\delta^{18}\text{O}^d$ (‰, VSMOW) | $\delta^{18}\text{O}^d$ (‰, VPDB) | Δ_{47} (‰) ARF ^e | ± 1 SE ^f (‰, analytical) | Sample Average Δ_{47} (‰), ARF | ± 1 SE (‰, external) | Temperature ^g (°C) | ± 1 SE (°C) |
|------------------------|------------------------------------|--------------------------------------|---------------------------------------|--------------------------------------|---------------------------------------|--|--|-----------------------------|----------------------------------|--------------------|
| G-R1-S1 7.3 cm | 3186.81 | 4.7 | 13.1 | -17.3 | | | | | | |
| G-R1-S1 10.7 cm | 3186.92 | 3.7 | 12.4 | -17.9 | | | | | | |
| G-R1-S1 65.5 cm | 3187.47 | 3.9 | 13.1 | -17.3 | | | | | | |
| G-R1-S2 0-3 cm | 3187.55 | 4.2 | 13.9 | -16.5 | | | | | | |
| G-R1-S4 0-4 cm | 3189.32 | 3.6 | 15.2 | -15.3 | | | | | | |
| G-R2-S2 33.7 cm | 3192.15 | 2.4 | 13.6 | -16.8 | | | | | | |
| G-R2-S2 36.2 cm | 3192.18 | 3.6 | 12.7 | -17.6 | | | | | | |
| G-R2-S2 37.0 cm | 3192.27 | 3.8 | 12.9 | -17.5 | | | | | | |
| G-R2-S2 64.3 cm | 3192.54 | 2.8 | 13.4 | -17.0 | | | | | | |
| G-R2-S2 66.0 cm | 3192.56 | 2.0 | 13.7 | -16.7 | | | | | | |
| G-R2-S2 69.1 cm | 3192.59 | 1.9 | 15.1 | -15.4 | | | | | | |
| G-R2-S2 70.3 cm | 3192.60 | 2.4 | 13.0 | -17.4 | | | | | | |
| G-R2-S2 73.4 cm | 3192.64 | 1.1 | 15.9 | -14.5 | | | | | | |
| G-R2-S2 81.6 cm | 3192.72 | 2.6 | 13.0 | -17.3 | | | | | | |
| G-R2-S3 10.1 cm | 3192.89 | 0.9 | 12.4 | -18.0 | | | | | | |
| G-R2-S3 16.6 cm | 3192.96 | 2.9 | 13.2 | -17.2 | | | | | | |
| G-R2-S3 16.7 cm | 3192.97 | 2.5 | 13.4 | -17.0 | | | | | | |
| G-R2-S3 25.9 cm | 3193.06 | 3.6 | 12.9 | -17.5 | | | | | | |
| G-R2-S3 30.6 cm | 3193.11 | 2.6 | 13.4 | -17.0 | | | | | | |
| G-R2-S3 62.4 cm | 3193.41 | 1.0 | 17.3 | -13.2 | | | | | | |
| G-R2-S4 39.9 cm | 3194.08 | 0.4 | 18.9 | -11.6 | | | | | | |
| G-R2-S6 34.5 cm | 3195.81 | -6.7 | 18.9 | -11.6 | | | | | | |
| G-R2-S6 45.6 cm | 3195.92 | -6.9 | 19.4 | -11.2 | | | | | | |
| G-R2-S7 31.6 cm | 3300.26 | -15.8 | 18.1 | -12.5 | | | | | | |
| G-R2-S7 39.8 cm | 3300.34 | -10.2 | 19.2 | -11.4 | 0.515 | 0.010 | 0.515 | 0.023 | 112 | 6 |
| G-R2-S7 46.5 cm | 3300.40 | -11.4 | 19.1 | -11.5 | 0.533 | 0.010 | 0.533 | 0.023 | 100 | 6 |

Table 2. continued

| Sample ID ^a | Depth ^b (meters, MD) | $\delta^{13}\text{C}^c$ (‰, VPDB) | $\delta^{18}\text{O}^d$ (‰, VSMOW) | $\delta^{18}\text{O}^d$ (‰, VPDB) | Δ_{47} (‰) ARF ^c | ± 1 SE ^f (‰, analytical) | Sample Average Δ_{47} (‰), ARF | ± 1 SE (‰, external) | Temperature ^g (°C) | ± 1 SE (°C) |
|------------------------|------------------------------------|--------------------------------------|---------------------------------------|--------------------------------------|---------------------------------------|--|--|-----------------------------|----------------------------------|--------------------|
| G-R2-S7 53.3 cm | 3196.74 | -10.6 | 20.1 | -10.5 | 0.580 | 0.008 | 0.549 | 0.031 | 81 | 8 |
| | | -10.6 | 20.1 | -10.5 | 0.518 | 0.008 | | | | |
| G-R2-S7 59.3 cm | 3196.80 | -11.3 | 18.4 | -12.1 | 0.486 | 0.009 | 0.486 | 0.023 | 134 | 6 |
| G-R2-S7 68.2 cm | 3196.89 | -11.2 | 19.1 | -11.5 | 0.524 | 0.008 | 0.510 | 0.010 | 115 | 3 |
| | | -11.2 | 19.2 | -11.4 | 0.492 | 0.011 | | | | |
| | | -11.2 | 19.1 | -11.4 | 0.515 | 0.009 | | | | |
| G-R2-S7 70.2 cm | 3196.91 | -10.5 | 18.8 | -11.8 | | | | | | |
| G-R2-S7 72.0 cm | 3196.93 | -10.9 | 19.3 | -11.3 | | | | | | |
| G-R2-S7 72.2 cm | 3196.93 | -11.0 | 19.2 | -11.4 | | | | | | |
| G-R2-S7 80.0 cm | 3197.01 | -16.0 | 18.5 | -12.0 | | | | | | |
| G-R4-S1 24.2 cm | 3295.14 | -6.7 | 17.7 | -12.8 | | | | | | |
| G-R4-S2 9.6 cm | 3295.87 | -9.2 | 17.6 | -12.9 | | | | | | |
| G-R4-S2 54.7 cm | 3296.33 | -9.3 | 17.6 | -12.9 | | | | | | |
| G-R4-S3 3.4 cm | 3296.60 | -4.4 | 18.0 | -12.5 | | | | | | |
| G-R4-S5 53 cm | 3299.10 | -4.9 | 19.0 | -11.6 | | | | | | |
| G-R4-S5 56.7 cm | 3299.14 | -5.0 | 19.1 | -11.5 | | | | | | |
| G-R4-S5 57-62 cm | 3299.18 | 3.1 | 19.0 | -11.6 | | | | | | |
| G-R4-S5 58.0 cm | 3299.15 | 1.6 | 18.1 | -12.4 | | | | | | |
| G-R4-S6 8.3 cm | 3299.43 | 3.5 | 19.5 | -11.1 | | | | | | |
| G-R4-S6 26.3 cm | 3299.61 | 4.2 | 19.0 | -11.6 | | | | | | |
| G-R4-S6 41.6 cm | 3299.76 | 6.6 | 20.5 | -10.1 | | | | | | |
| G-R4-S7 40.1 cm | 3300.31 | 3.3 | 18.5 | -12.1 | | | | | | |
| G-R5-S1 8.1 cm | 3300.47 | 3.5 | 17.3 | -13.3 | 0.514 | 0.009 | 0.514 | 0.023 | 113 | 6 |
| G-R5-S1 11.0 cm | 3300.50 | 4.1 | 19.2 | -11.3 | 0.529 | 0.008 | 0.529 | 0.023 | 103 | 6 |
| G-R5-S1 78.2 cm | 3301.17 | 3.1 | 19.6 | -11.0 | | | | | | |
| G-R5-S2 6.9 cm | 3301.34 | 5.5 | 20.8 | -9.8 | | | | | | |

Table 2. continued

| Sample ID ^a | Depth ^b (meters, MD) | $\delta^{13}\text{C}^c$ (‰, VPDB) | $\delta^{18}\text{O}^d$ (‰, VSMOW) | $\delta^{18}\text{O}^d$ (‰, VPDB) | Δ_{47} (‰) ARF ^e | ± 1 SE ^f (‰, analytical) | Sample Average Δ_{47} (‰), ARF | ± 1 SE (‰, external) | Temperature ^g (°C) | ± 1 SE (°C) |
|------------------------|------------------------------------|--------------------------------------|---------------------------------------|--------------------------------------|---------------------------------------|--|--|-----------------------------|----------------------------------|--------------------|
| G-R5-S2 9.8 cm | 3301.37 | 1.2 | 20.2 | -10.4 | 0.522 | 0.008 | 0.519 | 0.003 | 109 | 1 |
| | | 1.2 | 20.3 | -10.3 | 0.517 | 0.009 | | | | |
| G-R5-S2 18.3 cm | 3301.45 | 1.3 | 17.1 | -13.4 | 0.564 | 0.009 | 0.564 | 0.023 | 82 | 6 |
| G-R5-S3 3.4 cm | 3302.24 | -4.3 | 17.7 | -12.8 | 0.496 | 0.009 | 0.496 | 0.023 | 126 | 6 |
| G-R5-S3 12.4 cm | 3302.32 | -2.9 | 17.9 | -12.6 | | | | | | |
| G-R5-S3 78.2 cm | 3302.93 | -4.0 | 17.5 | -13.0 | | | | | | |
| G-R5-S4 19.8 cm | 3303.00 | -5.3 | 17.9 | -12.7 | 0.493 | 0.008 | 0.529 | 0.036 | 103 | 9 |
| | | -5.3 | 17.8 | -12.7 | 0.565 | 0.008 | | | | |
| G-R5-S4 61.1 cm | 3303.50 | -8.3 | 20.2 | -10.4 | | | | | | |
| G-R5-S5 28.4 cm | 3304.00 | -7.3 | 17.9 | -12.6 | | | | | | |
| G-R5-S5 67.1 cm | 3304.39 | -9.0 | 19.0 | -11.5 | | | | | | |
| G-R6-S1 33.1 cm | 3307.73 | -10.1 | 21.6 | -9.1 | | | | | | |
| G-R6-S1 35.8 cm | 3307.76 | -12.5 | 18.4 | -12.1 | | | | | | |
| G-R6-S1 49.8 cm | 3307.90 | -18.8 | 25.3 | -5.4 | 0.620 | 0.009 | 0.593 | 0.014 | 67 | 4 |
| | | -18.8 | 25.2 | -5.6 | 0.571 | 0.009 | | | | |
| | | -18.9 | 25.2 | -5.6 | 0.587 | 0.008 | | | | |
| G-R6-S3 63.7 cm | 3309.80 | -13.7 | 20.3 | -10.3 | 0.579 | 0.010 | 0.549 | 0.030 | 91 | 8 |
| | | -13.8 | 20.3 | -10.3 | 0.519 | 0.009 | | | | |
| G-R6-S3 65.4 cm | 3309.97 | -14.0 | 21.9 | -8.7 | | | | | | |

^aSample identifier represents Hole-Run-Section-Distance (cm)

^bDepths are reported in meters measured depth (MD) for phase 3 drilling.

^c $\delta^{13}\text{C}$ values of calcite are reported in per mil relative to Vienna Pee Dee Belemnite (VPDB).

^d $\delta^{18}\text{O}$ values are reported in per mil relative to both VPDB and Vienna Standard Mean Ocean Water (VSMOW).

^e Δ_{47} values are reported in the absolute reference frame (ARF) of Dennis et al. (2011).

^fStandard error (SE) for samples not externally replicated reflect actual analytical error for the sample, or long-term error in standard analyses (0.023 ‰), whichever is larger.

^gTemperatures calculated using the calibration of Kluge et al. (2015).

(1SE)), corresponding to calcite formation temperatures of 67 to 134 °C, with average uncertainties of ± 5 °C considering the analytical error. Clumped-isotope temperatures for veins sampled in the serpentinite-bearing fault gouges of the SDZ at 3197.9 m MD (134 ± 2 °C, 1SE) and in the sheared massive siltstone unit approximately 2 m below the CDZ at 3302.2 m MD (126 ± 2 °C, 1 SE) are higher than present-day downhole temperatures of ~ 115 °C (Fig. 3). Clumped isotope temperatures are 30 °C below modern ambient borehole temperatures within the sheared calcareous siltstone-claystone units at 3309.8 m MD.

Clumped isotope temperatures were used to calculate $\delta^{18}\text{O}_{\text{water}}$, $\delta^{13}\text{C}_{\text{CO}_2}$, and $\delta^{13}\text{C}_{\text{CH}_4}$ values for fluids and gases that would have been in equilibrium with the calcite at the time of mineral growth; for samples that do not have clumped isotope measurements, these values were calculated using a modern borehole temperature of 115 °C.

The mean calculated $\delta^{18}\text{O}_{\text{paleowater}}$ compositions of the calcite veins are +3 ‰, which is in the range of $\delta^{18}\text{O}$ values reported for waters sampled from the SAFOD borehole (-4 ‰ to +7 ‰; Thordsen et al., 2010). The values for $\delta^{18}\text{O}_{\text{water}}$ increase as a function of increasing vein formation temperature with the exception of one calcareous clast sampled at 3307.9 m MD that had a calculated $\delta^{18}\text{O}_{\text{water}}$ of +4 ‰ and a relatively low clumped isotope temperature of 67 ± 4 °C (1 SE).

The calculated $\delta^{13}\text{C}_{\text{CO}_2}$ composition of CO_2 that would have been in equilibrium with the vein calcite has a mean value of -10 ± 8 ‰ (1σ), and is isotopically heavier at the sampled depths (3186 to 3309 m MD) than the mean $\delta^{13}\text{C}_{\text{CO}_2}$ value of -19 ± 4 ‰ (1σ) reported for SAFOD mudgas CO_2 (255 to 3903 m MD; Wiersberg and Erzinger, 2008). The calculated $\delta^{13}\text{C}_{\text{CO}_2}$ composition of CO_2 also is heavier than soil CO_2 along the SAFZ, which has a mean $\delta^{13}\text{C}_{\text{CO}_2}$ value of -2 ± 1 ‰ (1σ) (Lewicki et al., 2003). Calculated $\delta^{13}\text{C}_{\text{CO}_2}$ values are tightly clustered at

-14 ± 1 ‰ (1σ) from 3196.7 to 3198.0 m MD; however, an abrupt shift to a $\delta^{13}\text{C}_{\text{CO}_2}$ value of $+0.8$ ‰ occurs within the sheared silty shale units just below the CDZ at 3300.0 m MD. $\delta^{13}\text{C}_{\text{CO}_2}$ values become isotopically lighter with depth from 3198 m MD to 3309.8 m MD. The $\delta^{13}\text{C}_{\text{CO}_2}$ value is -17 ‰ within the calcareous siltstone and claystone units at 3309.8 m MD.

The carbon isotopic composition of methane that would have been in equilibrium with the calcite veins ($\delta^{13}\text{C}_{\text{CH}_4} -58 \pm 10$ ‰, 1σ) is about 17 ‰ lower than the mean value of the modern-day mudgas $\delta^{13}\text{C}_{\text{CH}_4}$ (-41 ± 9 ‰, 1σ) (Wiersberg and Erzinger, 2008).

5. Discussion

The following generalizations can be made regarding the results of the stable isotope data. First, there are systematic variations in the isotopic values as a function of lithology and with distance from the SDZ and CDZ. Whereas $\delta^{13}\text{C}$ values vary throughout the sampled interval, the greatest variation in $\delta^{18}\text{O}$ is generally restricted to the structural transition across the SDZ. Secondly, the clumped-isotope temperatures for some samples are similar to present-day downhole temperatures. A few veins in deformed gouge and rocks near the SDZ and CDZ have Δ_{47} temperatures that exceed modern borehole temperatures by 10 to 20 °C, while a few veins below the CDZ have Δ_{47} temperatures that are ~20 to 30 °C below modern ambient borehole temperatures. We use these data to constrain (1) the origin and temperature of fluids from which the veins precipitated, (2) the possible migration pathways of fluids within the SAFZ at seismogenic depths, and (3) implications for fault strength.

5.1 Constraints on the origin of fluids from carbon isotopes

The $\delta^{13}\text{C}$ values of carbonate veins sampled within the SAFOD borehole likely represent a mixture of several organic- and inorganic-derived carbon sources including biogenic and thermogenic CO_2 and/or CH_4 derived from (1) bicarbonate-bearing formation fluids in

sediments, (2) dissolution of calcareous shells or diagenetic calcite cements, (3) metamorphism of carbonates, (4) mantle degassing, and (5) organic matter. Here we evaluate these potential fluid sources by comparing the measured $\delta^{13}\text{C}$ values of carbonate veins and back-calculated equilibrium $\delta^{13}\text{C}$ values of CO_2 and CH_4 with modern borehole gas values, and compare the $\delta^{13}\text{C}$ values of carbonate veins to their sedimentary host rocks.

The calculated $\delta^{13}\text{C}_{\text{CO}_2}$ values for a subset of calcite veins are in equilibrium with modern-day mudgas CO_2 (Fig. 4a). The $\delta^{13}\text{C}_{\text{CO}_2}$ that would be in equilibrium with calcite veins sampled from the serpentinite-bearing fault gouge of the SDZ (3196.4 to 3198.1 m MD), sheared calcareous siltstone-claystone units (3307.4-3311.0 m MD), and the majority of vein material obtained from cuttings are in approximate carbon isotopic equilibrium with the modern-day mud gas ($-26 < \delta^{13}\text{C}_{\text{CO}_2} < -13$ ‰) that fall within the range of $\delta^{13}\text{C}$ values typical of CO_2 generated from the thermal breakdown of organic matter (-25 to -10 ‰) (Fig. 4a).

The carbon isotope trends observed just outside the SDZ and CDZ are consistent with a second fluid source that interacted with marine carbonates. Calcite veins sampled within the foliated sandstone-siltstone-shale cataclasites (3186.8-3194.0 m MD), serpentinite-bearing fault gouge (CDZ, 3297.1-3299.1 m MD), and sheared silty shale (3299.1-3301.5 m MD) have $\delta^{13}\text{C}$ values (Fig. 4a) that fall within the range of $\delta^{13}\text{C}$ values typical of marine carbonates ($-2 < \delta^{13}\text{C} < +2$ ‰; Wycherley et al., 1999). Calculated $\delta^{13}\text{C}_{\text{CO}_2}$ using our $T(\Delta_{47})$ data fall within the range of $\delta^{13}\text{C}_{\text{CO}_2}$ values predicted to be in carbon isotope equilibrium with limestone and marble host rocks sampled by Pili et al. (2011) from several localities along the SAFZ in the Parkfield area.

The carbon isotopic compositions of the veins from the black ultracataclasite (3194.0-3196.4 m MD), sheared siltstone and shale (3295.1 to 3296.3 m MD), and foliated sandstone-siltstone-shale (3303.3 to 3307.4 m MD) have values ($-12 < \delta^{13}\text{C}_{\text{CO}_2} < -2$ ‰) that (1) fall within

a range of values for CO₂ derived from mixing of two sources (e.g., thermal break of organic matter and limestone) or from regional metamorphism or mantle degassing source (Wycherley et al., 1999), and (2) are intermediate between the veins found within their adjacent units (Fig. 4a). Our T(Δ_{47}) are not consistent with the calcite veins having precipitated from fluids within the range of temperatures required for significant CO₂ generation from regional or contact metamorphism. This includes two samples from the sheared massive siltstone (3301.5-3303.3 m MD) that have clumped-isotope temperatures of 103 and 126 °C, close to the modern ambient borehole temperature of ~114 °C at those depths (Fig. 3). Thus, it is possible that the calculated $\delta^{13}\text{C}_{\text{CO}_2}$ values for this subset of veins are influenced by carbon-bearing fluids from the adjacent rock units.

The $\delta^{13}\text{C}$ values of a subset of veins sampled from the sheared siltstone and shale (3295.1 to 3296.3 m MD) and foliated sandstone-siltstone-shale (3303.3 to 3307.4 m MD) (Figs. 3 and 4a) could be controlled, in part, by the localized flux of mantle volatiles between the SDZ and CDZ reported by Wiersberg and Erzinger (2011). The equilibrium $\delta^{13}\text{C}_{\text{CO}_2}$ values of this subset of veins (Fig. 4a) fall within mantle $\delta^{13}\text{C}_{\text{CO}_2}$ values of -4 to -7 ‰ (Wycherley et al., 1999), but do not permit unequivocal interpretations of fluid provenance because bulk crustal and average mantle-derived $\delta^{13}\text{C}_{\text{CO}_2}$ values overlap (-3 to -8 ‰, VPDB). The $^3\text{He}/^4\text{He}$ values of fluids and veins may be more diagnostic. The $^3\text{He}/^4\text{He}$ values obtained from fluids (Kennedy et al., 1997) and veins (Pili et al., 2011) sampled from various locations along the SAFZ are consistent with a flux of mantle-derived fluids entering the SAF zone. The spatial distribution of measured $^3\text{He}/^4\text{He}$ ratios from SAFOD mud gas were interpreted by Wiersberg and Erzinger (2011) to represent (1) little to no flux of mantle volatiles within the Pacific Plate side of the SAF, (2) the presence of mantle-derived volatiles at small spatial scales between the SDZ and CDZ that were

limited by rock permeability, and (3) an elevated flux of mantle volatiles within the North American Plate side of the SAF. Our results are consistent with limited migration of mantle-derived fluids into the fault zone at the SAFOD locality, possibly along fracture networks on either side of the CDZ. However, the systematic shift from low to high $\delta^{13}\text{C}$ values can also be explained by increasing contributions of carbon derived from marine carbonate in the damage zones adjacent to the low permeability SDZ and CDZ.

The calculated $\delta^{13}\text{C}_{\text{CH}_4}$ values show that none of the calcite veins formed in carbon-isotope equilibrium with the methane encountered in the drill hole at the sample depths (Fig. 4b). If methane was involved in the formation of the veins, then either (1) the veins formed at shallower depths where biogenic methane was once more prevalent, or (2) the $\delta^{13}\text{C}$ of the methane has been altered since the veins formed.

The measured $T(\Delta_{47})$ and calculated $\delta^{13}\text{C}_{\text{CH}_4}$ values may support the hypothesis that at least some of the calcite veins precipitated from fluids at depths where biogenic or mixed biogenic/thermogenic gases are prevalent from 2 to 2.5 km MD (Fig. 4b). This hypothesis has been suggested by the results from previous basin modeling (d'Alessio and Williams, 2007) and stable isotope studies (Wiersberg and Erzinger, 2008; 2011). Integrated (U/-Th)/He and fission track age and length modeling indicate that the SAFOD site has experienced <1 km of burial and subsequent unroofing since SAF initiation (d'Alessio and Williams, 2007). Based on this estimate of d'Alessio and Williams (2007) and a constant modern-day geothermal gradient (Blythe et al., 2004), it is unlikely that the rocks encountered within the SAFOD borehole have experienced temperatures outside the range of approximately 80 to 150 °C since the onset of faulting. Wiersberg and Erzinger (2008) showed that the SAFOD mud gas hydrocarbons above 2500 m MD have carbon and hydrogen compositions consistent with a significant microbial

component. Calcite veins precipitating from fluids at these depths should preserve a $T(\Delta_{47})$ of less than 70 °C. Only one sample of a carbonaceous clast at 3307.9 m MD records a crystallization temperature low enough to have formed at depths where biogenically derived gases are present (Fig. 3).

The calculated $\delta^{13}\text{C}_{\text{CH}_4}$ values are not consistent with the hypothesis that the veins formed in carbon isotopic equilibrium with modern thermogenic gases (Fig. 4c); however, the measured $T(\Delta_{47})$ for the veins are consistent with formation at depths where thermogenic gases are prevalent. Wiersberg and Erzinger (2011) attribute the observed mud gas $\text{CO}_2\text{-CH}_4$ carbon isotope disequilibrium to preferential removal of light carbon molecules due to diffusive gas loss from the reservoir units. Thus, the veins could have formed in equilibrium with gases prior to post-formation migration when the $\delta^{13}\text{C}$ values of the methane would have been significantly lower. These findings are consistent with the $\delta^{13}\text{C}$ variations in the SAFOD calcite veins not having been influenced significantly by the presence of methane.

The carbon isotope data are consistent with a relatively open-flow system through interconnected fracture networks rather than pervasive or porous flow within portions of the damage zone proximal to the actively-deforming fault strands (Fig. 3). Only the vein samples hosted within the SDZ and CDZ have carbon isotopic values similar to their host rocks (Fig. 3) consistent with closed-system fluid flow regime.

5.2 Constraints on fluid pathways and fluid-rock interaction from oxygen isotopes

The oxygen isotope compositions of the carbonate veins encountered within the SAFOD borehole are likely controlled by several factors including the parent fluid isotopic composition (meteoric water versus basin brines), fluid temperatures, fluid-rock interactions, and water-to-rock ratios. Here we compare our calculated $\delta^{18}\text{O}_{\text{paleowater}}$ values to values of the modern SAFOD

borehole fluids and nearby well and spring waters in order to determine possible fluid sources, migration pathways, and the extent of fluid-rock interaction within the SAFOD borehole.

The $\delta^{18}\text{O}_{\text{paleofluid}}$ values are consistent with vein precipitation from meteoric fluids advected to sampled depths on the southwest side of the SDZ, and with evolved meteoric/basin brine fluids on the northeast side of the SDZ. The $\delta^{18}\text{O}$ values of well waters (Fig. 4d) measured at ~3 km depth (Thordsen et al., 2005) are enriched in ^{18}O by approximately 1.2 ‰ compared to the most ^{18}O -rich local shallow groundwater (Thompson and White, 1991). These observations are consistent with the advection of shallow groundwater to at least 3 km depth possibly along permeable fracture networks through the damage zone of the SAF. The $\delta^{18}\text{O}_{\text{paleofluid}}$ values in equilibrium with calcite veins at modern-day borehole temperatures from the foliated sandstone-siltstone-shale cataclasites located on the southwest side of the SDZ range from -4 to +1 ‰ (Fig. 4d). These $\delta^{18}\text{O}_{\text{paleofluid}}$ values are similar to the $\delta^{18}\text{O}$ of modern SAFOD borehole fluids (Thordsen et al., 2005) and waters sampled from the Jack-Ranch Highway 46 well (Kennedy et al., 1997) located in close proximity to the SAF approximately 30 km south of the SAFOD study area (Fig. 4d). The observed oxygen isotope disequilibrium between the calcite veins and host rocks ($\Delta^{18}\text{O}_{\text{vein-host rock}} \sim 10$ ‰) above the SDZ is consistent with the infiltration of meteoric fluids to these depths (Fig. 3). The $\delta^{18}\text{O}$ values of well water encountered deeper within the borehole at 3608 m MD on the northeast side of the actively-deforming zones were interpreted by Thordsen et al. (2010) to be consistent with rock-buffered formational fluids at intermediate depths and temperatures (Fig. 4e). The Middle Mountain Oil seep and Varian-Phillips wells are within 1.5 km east of the SAF near Parkfield and have high $\delta^{18}\text{O}$ values of +5.6 and +5.9 ‰ (Fig. 4e), respectively (Thompson and White, 1991). The $\delta^{18}\text{O}_{\text{paleofluid}}$ values (Fig. 4e) for veins sampled below the foliated sandstone-siltstone-shale cataclasites (3194.0 m MD) follow a trend

toward $\delta^{18}\text{O}$ values similar to the evolved meteoric waters or oil field brines sampled on the northeast side of the SAF.

The difference in the observed $\delta^{18}\text{O}$ values of waters on either side of the actively-deforming zones is consistent with the SAFZ acting as a baffle to cross-fault fluid flow (Fig. 4d,e). The $\delta^{18}\text{O}_{\text{water}}$ values calculated using $T(\Delta_{47})$ and modern borehole temperatures for the veins sampled from 3194.0 to 3309.9 m MD are intermediate between modern day $\delta^{18}\text{O}_{\text{water}}$ values sampled on either side of the fault zone. We interpret these intermediate values to represent episodic mixing between meteoric fluids and basin brines within open fracture networks possibly during episodes of fracture opening associated with motion on the fault. Our interpretation is consistent with the results of Mittempergher et al. (2011), who interpreted alternating luminescent bands and crack-seal growth textures to represent changing fluid conditions after fracture development. Additionally, Holdsworth et al. (2011) observed that veins within the active fault gouges occur primarily within clasts of various lithologies in contrast to the presence of relatively continuous veins found within the inactive sections of the fault zone. This observation is consistent with vein formation within the active sections of the SAF predating aseismic creep, and possibly providing a record of deformation episodes characterized by fracture-network facilitated fluid flow within the impermeable fault core.

The calculated calcite vein $\delta^{18}\text{O}_{\text{paleowater}}$ values, variable $T(\Delta_{47})$ values, and the observed oxygen isotope equilibrium between calcite veins and host rock are consistent with calcite vein precipitation from pore fluids that have undergone varying degrees of oxygen isotope exchange with the host rocks over a range of temperatures (Fig. 4f). An original pore fluid having a meteoric oxygen isotope composition would have likely undergone some degree of isotopic exchange with the host rocks enriching the pore fluids in heavy oxygen. The $\delta^{18}\text{O}_{\text{paleowater}}$ values

calculated for the calcite veins and cuttings sampled from 3194.0 to 3309.9 m MD fall within the range of values predicted for water-mineral equilibrium fractionation curves representing the predominant mineralogy of the Great Valley sequence host rocks (Fig. 4f) including quartz, serpentinite, and illite-smectite (Barnes et al., 2013; Suchecky and Land, 1983). These observations are consistent with closed-system fluid flow conditions below 3194.0 m MD.

The changes in $\delta^{18}\text{O}$ of the carbonate cements and the back-calculated fluids can be used to model the isotopic evolution of the fluid-rock system (Fig. 5) using the method outlined in Banner and Hansen (1990). We modeled heating from 0 to 140 °C using the average $\delta^{18}\text{O}$ value of the six host rock samples (+21 ‰, VSMOW) and $\delta^{18}\text{O}$ of water equal to the average of the shallow spring and well waters near Parkfield (-7 ‰, Thompson and White, 1999).

The open system model (Fig. 5) tracks the evolution of the fluid-rock system as repeated additions of unreacted fluid (i.e., with constant oxygen isotopic composition) displace the existing pore fluids. The $\delta^{18}\text{O}$ values of the precipitating carbonates evolve toward the fluid $\delta^{18}\text{O}$ composition as temperatures increase (Δ_{47} decreases). The open-system heating model predicts a 10 ‰ shift in carbonate $\delta^{18}\text{O}$ values over the temperature range indicated by the $T(\Delta_{47})$ results spanning from 67 to 134 °C. Our dataset does not follow the pattern predicted by the open-system model.

Instead, our data set is well described by a closed-system (rock-buffered) heating model for water-rock ratios less than ~0.25 wt %. The $\delta^{18}\text{O}$ values of the majority of the carbonate cements are consistent with very low water-rock ratios (< 0.1 weight %), supporting the interpretation that the veins formed in a rock-buffered system. This result is also consistent with our interpretation of the modern waters sampled by previous workers within the SAFOD well. Fluids sampled at approximately 3065 m MD by Thordsen et al. (2005) fall between the 0.5 and

1.0 weight % water-to-rock ratio contour consistent with rapid downward migration of meteoric fluids with limited fluid-rock interaction on the west side of the fault. The $\delta^{18}\text{O}$ values of deeper formation fluids sampled at about 3608 m MD fall below the 0.01 weight % water-to-rock contour consistent with rock-buffered formation fluids.

6. Model of vein formation

The veins analyzed in this study were sampled throughout the damage zone and along the contacts of the actively-deforming serpentinite-bearing units. The spatial distribution of vein isotopic compositions appears to be controlled primarily by lithology, which exerts primary control on fluid chemistry in a closed fluid system. The isotopic compositions of the veins near the lithologic contacts and actively-deforming zones have values of $\delta^{13}\text{C}$ and $\delta^{18}\text{O}$ intermediate between the two adjacent units, consistent with these contact surfaces acting as local fluid conduits possibly accommodating some displacement. We propose that the veins formed in compartments where fluids become isolated and follow different isotopic evolution paths controlled by the local mineralogy and carbon sources. Our observations are consistent with microstructural studies of the calcite veins within meters of the actively-deforming portions of the SAF by Mittempergher et al. (2011) and Hadizadeh et al. (2012), which clearly show evidence of locally high fluid pressures interpreted to have formed in compartments isolated from each other by zones of insoluble material formed from stress driven pressure solution (Gratier et al., 2009; Schleicher et al., 2009; Mittempergher et al., 2011). In light of these observations, we interpret the isotopic data to be consistent with limited, episodic, and heterogeneously distributed fluid flow within the SDZ and CDZ, and relatively open-flow conditions within the damage zones proximal to the low-permeability deforming zones that may

serve as a permeable pathway through the upper crust for meteoric fluids to reach seismogenic depths.

7. Implications for fault strength

7.1 Fluid pressure

Several models have been proposed for the development of high pore fluid pressures (and low effective normal stress) that could explain the slip on the SAF under very low shear stresses (Zoback et al., 1987), and the associated lack of an observable heat anomaly near the fault (Lachenbruch, 1980). A model of episodic flow and sealing involves a cyclical process in which fluids from the host rocks saturate the fault zone, high fluid pressure compartments form as fractures become mineralized, earthquakes are triggered by ruptures between high- and low-pressure seals, and fluids are expelled during shearing (Byerlee, 1993). A channelized, continuous flow model envisions fluid flow up a low, but pressure-dependent permeable fault zone in which fluids are sourced from depth, possibly from the mantle (Rice, 1992). An alternative model that involves flow of fluids from deep sources is the fault-valve model of Sibson (1990) in which elevated fluid pressure develops below a locked, impermeable fault until seismic slip ruptures the fault seal and pressurized fluids are released.

Our results are not consistent with the channelized, continuous flow model or the fault-valve model. Morrow et al. (2014) found that the gouge in the actively deforming zones has ultra-low permeability and concluded that fluid-flow occurs in the highly fractured bounding rocks. Carbon and oxygen isotope disequilibrium between veins in the foliated and sheared siltstones and shales above the SDZ are consistent with a meteoric water-dominated open-flow system on the southwest side of the actively-deforming zones. Oxygen equilibrium between calcite veins and host rocks associated with the actively-deforming strands are consistent with

closed-system behavior, and the results of Morrow et al. (2014). Additionally, the carbon isotopic composition of the veins is not consistent with continuous or episodic replenishment of fluids into the fault zone from the upper mantle. This interpretation is supported by results from magnetotelluric data obtained by Becken et al. (2008), who show that the SAF does not currently act as a major fluid pathway through the entire crust. Flow through a low-permeability fault zone would allow for the fluids to thermally equilibrate with the surrounding host rocks; thus, clumped-isotope temperatures would not likely provide a record of a heat-flow anomaly unless fluids were migrating rapidly upward from greater depths.

The model of episodic flow and sealing (Byerlee, 1993) is compatible with our stable isotope data wherein fluids flow into the fault, fault-sealing processes compartmentalize the fluid zones through mineralization, pressure solution, and compaction of fault gouges, and locally high-pressures could develop under fault-normal compression. Recent experiments, however, show that the clay-rich gouge of the SDZ and CDZ have extremely low coefficients of sliding friction and that elevated pore fluids are not necessary to explain the low strength and creep behavior (Lockner et al., 2011; Carpenter et al., 2011, 2012; Coble et al., 2014; French et al., 2015).

7.2 Fluid-rock interactions

Wintsch et al. (1995) modeled the interaction of meteoric waters with rocks having granitic compositions in both water- and rock-dominated environments at zeolite to lower-greenschist-facies conditions, which are appropriate for the SAF at SAFOD. The infiltration of meteoric water into the fault zone is expected to shift the composition of the pore water away from equilibrium established between the existing fault fluids and mineral assemblages. Given these conditions, the solid-fluid equilibria models of Wintsch et al. (1995) predict the formation

of illite and smectite (I-S) in meteoric water-dominated systems by way of replacement reactions with feldspar, and the replacement of phyllosilicates by feldspars in a rock-dominated system. Wintsch et al. (1995) predicts the production of phyllosilicates, especially chlorite and smectite (C-S), in both water- and rock-dominated environments provided the chemical activity of magnesium is high enough. In light of the fluid-mineral equilibria models of Wintsch et al. (1995), we suggest that there is (1) a short-lived water-dominated chemical environment that favors the generation of I-S phyllosilicates along newly formed fracture and mineral surfaces (Fig 6 a and b), followed by (2) a period of rock-dominated fluid-rock interaction as fluids become more compartmentalized in the fault zone because of precipitation of feldspar or C-S phyllosilicates in fractures and pores (Fig 6c).

Our interpretation is supported by Schleicher et al. (2010) who utilized electron microscopy and x-ray diffraction to identify phyllosilicate phases within the SAFOD borehole. Schleicher et al. (2010) observed the preferential formation of thin (<100 nm thick) coatings of both I-S and C-S on fracture surfaces and grain boundaries. They proposed a three-step model of fault zone evolution wherein (1) fluids are introduced into the fault zone along fracture networks after displacement, (2) phyllosilicates precipitate along fracture surfaces and grain boundaries via mineral replacement reactions, and (3) clay-coated fracture networks coalesce, eventually leading to the onset of creep. Macroscopically, Moore and Rymer (2012) and Bradbury et al. (2015) document the presence of smectitic clays saponite and palygorskite in the foliated clay gouge from the CDZ and SDZ. The illite-smectite mineral assemblages observed near the SDZ and CDZ are more smectite-rich than kinetic models predict for typical prograde burial sequences (Schleicher et al. 2009). The increased smectite content could be a result of the influx of cool fluids or fluids with K^+ concentrations lower than typical sedimentary brines (Schleicher

et al., 2009), consistent with our model of vein formation that predicts the advection of meteoric fluids along permeable fracture networks within the damage zone of the SAF.

8. Summary

Clumped-isotope thermometry of calcite veins within the SAFOD borehole provides a record of paleo-fluid flow within the fault zone. The C and O-isotope compositions vary systematically as a function of distance from the SDZ and CDZ. Fracture networks located adjacent to the SDZ and CDZ served as conduits for advecting meteoric fluids to seismogenic depths. The advecting meteoric fluids likely contained inorganic carbon derived from interaction with marine carbonates. A meteoric water-dominated environment would favor the formation of the low-strength phyllosilicate fault rocks. The difference in the calculated $\delta^{18}\text{O}_{\text{paleofluids}}$ ($\Delta\delta^{18}\text{O} \sim 14 \text{ ‰}$) from which the vein cements grew on either side of the fault zone is consistent with the SDZ and CDZ acting as low-permeability cross-fault fluid-flow barriers. The oxygen isotopic composition of fluids within these two actively deforming zones was controlled by fluid interactions with the surrounding host rocks. Locally, the fluid within the SDZ and CDZ contained organically derived carbon released from the thermal breakdown of organic matter during burial. Clumped-isotope temperatures provide evidence that calcite vein growth occurred over a wide range of temperatures that bound modern-day ambient borehole temperatures. The hydrogeologic system can be envisioned as a network of short-lived conduits that open episodically during deformation and transport fluids from the surrounding host rocks into the fault zone. These conduits are then sealed by mineralization and compartmentalize the fault zone, possibly allowing for the development of locally high fluid pressures, and subsequent fracture formation and slip in otherwise unfavorable stress conditions.

Acknowledgements

We thank Stephen Hickman, Mark Zoback, and Bill Ellsworth for bringing the SAFOD project to fruition. We also thank Jim Thordsen, Yousef Kharaka, and Thomas Wiersberg for their input and willingness to share their as yet unpublished water and gas chemistry data during the early phases of this study. We also thank the SAFOD student crew for their help and support in collecting some of the cuttings that were used in this study. A special thanks to Andrew Schauer and Kyle Samek for their time and patience while training PBL at the IsoLab, UW-Seattle. Finally, we thank Olivier Fabbri and an anonymous reviewer for their constructive comments that significantly improved this manuscript.

The authors acknowledge financial support for this study to P. B. Luetkemeyer from a Geological Society of America graduate student research grant and Grant-in-Aid of Research from the American Association of Petroleum Geologists, to D. Kirschner from the National Science Foundation (EAR-0643223), to J. Chester and F. Chester from the National Science Foundation (EAR-0643339), to J. Evans from the National Science Foundation (EAR-0643027, EAR-0454527), and to K. W. Huntington from the National Science Foundation (EAR-1156134).

Appendix A. Supplementary Figures

Supplementary data associated with this article can be found in the online version. These data include images of the Phase 3 core with sample locations and results from conventional stable isotope analyses and clumped-isotope thermometry.

References

Affek, H.P., Eiler, J.M., 2006. Abundance of mass 47 CO₂ in urban air, car exhaust, and human breath. *Geochem. Cosmochim. Acta* 70, 1-12.

- Banner, J.L., Hanson, G.N., 1990. Calculation of simultaneous isotopic and trace element variations during water-rock interaction with applications to carbonate diagenesis: *Geochim. Cosmochim. Acta* 54, 3123-3137.
- Barnes, J.D., Eldman, R., Lee, C-T. A., Errico, J.C., Loewy, S., Cisneros, M., 2013. Petrogenesis of serpentinites from the Franciscan Complex, western California, USA. *Lithos* 178, 143-157.
- Beaudoin, N., Bellahsen, N., Lacombe, O., Emmanuel, L., 2011. Fracture-controlled paleohydrology in a basement-cored, fault-related fold: Sheep Mountain Anticline, Wyoming, United States. *Geochem. Geophys. Geosys.* 12, Q06011.
- Becken, M., Ritter, O., Park, S.K., Bedrosian, P.A., Weckmann, U., Weber, M., 2008. A deep crustal fluid channel into the San Andreas Fault system near Parkfield, California. *Geophys. J. Int.* 173, 718-732.
- Bergman, S.C., Huntington, K.W., Crider, J., 2013. Tracing paleofluid sources using clumped isotope thermometry of diagenetic cements along the Moab Fault, Utah. *Am. J. Sci.* 315, 490-515.
- Boles, J.R., Eichhubl, P., Graven, G., Chen, J., 2004. Evolution of a hydrocarbon pathway along basin-bounding faults: Evidence from fault cement. *AAPG Bull.* 88, 947-970.
- Bottinga, Y., 1968. Calculation of fractionation factors for carbon and oxygen isotopic exchange in the system calcite-carbon dioxide-water. *J. Phys. Chem.* 72, 800-808.
- Bottinga, Y., 1969. Calculated fractionation factors for carbon and hydrogen isotope exchange in the system calcite-carbon dioxide-graphite-methane-hydrogen-water vapor. *Geochim. Cosmochim. Acta* 33, 49-64.

- Bradbury, K.K., Barton, D.C., Solum, J.G., Draper, S.D., Evans, J.P., 2007. Mineralogic and textural analysis of drill cuttings from the San Andreas Fault Observatory at Depth (SAFOD) boreholes: Initial interpretations of fault zone composition and constraints on geologic models. *Geosphere* 7, 299-318.
- Bradbury, K.K., Evans, J.P., Chester, J.S., Chester, F.M., Kirschner, D.L., 2011. Lithology and internal structure of the San Andreas fault at depth based on characterization of Phase 3 whole-rock core in the San Andreas Fault Observatory at Depth (SAFOD) borehole. *Earth Planet. Sci. Lett.* 310, 131-144.
- Bradbury, K. K., Davis, C., Shervais, J. W., Janecke, S. U., and Evans, J. P., 2015, Composition, alteration, and texture of fault-related rocks from SAFOD core and surface analogs: Evidence for deformation processes and fluid-rock interactions, *Pure Appl. Geophys.* 172,1053-1078, doi:10.1007/s00024-014-0896-6.
- Budd, D.A., Frost, E.L., Huntington, K.W., Allwardt, P.F., 2013. Syndepositional deformation features in high-relief carbonate platforms: long-lived conduits for diagenetic fluids. *J. Sediment. Res.* 83, 12–36. doi: 10.2110/jsr.2013.3.
- Byerlee, J., 1990. Friction, overpressure, and fault normal compression. *Geophys. Res. Lett.*, 17, 2109-2122.
- Byerlee, J., 1993. Model for episodic flow of high-pressure water in fault zones before earthquakes. *Geology*, 21, 303-306.
- Blythe, A.E., d'Alessio, M.A., Bürgmann, R., 2004. Constraining the exhumation and burial history of the SAFOD pilot hole with apatite fission track and (U-Th)/He thermochronology. *Geophys. Res. Lett.* 31, L15S16.

- Campbell, K.A., Farmer, J.D., Marais, D.D., 2002. Ancient hydrocarbon seeps from the Mesozoic convergent margin of California: carbonate geochemistry, fluids and paleoenvironments. *Geofluids* 2, 63-94.
- Carpenter, B., Marone, C., and Saffer, D., 2011. Weakness of the San Andreas Fault revealed by samples from the active fault zone, *Nat. Geosci.*, 4, 251–254, doi:10.1038/ngeo1089.
- Carpenter, B. M., Saffer, D. M., Marone, C., 2012. Frictional properties and sliding stability of the San Andreas Fault from deep drill core, *Geology*, 40, 759–762, doi:10.1130/G33007.1.
- Coble, C. G., French, M. E., Chester, F. M., Chester, J. S., Kitajima, H., 2014. Frictional Strength of the Creeping Section of the San Andreas Fault at SAFOD, *Geophys. J. Int.* 199, 956-967, doi:10.1093/gji/ggu306.
- d'Alession, M.A., Williams, C.F., 2007. Putting it all together: Exhumation histories from a formal combination of heat flow and a suite of thermochronometers. *J. Geophys. Res.* 112, B08412.
- Davisson, M.L., Presser, T.S., Criss, R.E., 1994. Geochemistry of tectonically expelled fluids from the northern Coast ranges, Rumsey Hills, California, USA. *Geochim. Cosmochim. Acta* 58, 1687-1699.
- Dennis, K.J., Affek, H.P., Passey, B.H., Schrag, D.P., Eiler, J.M., 2011. Defining an absolute reference frame for 'clumped' isotope studies of CO₂. *Geochim. Cosmochim. Acta* 75, 7117-7131.
- Eiler, J.M., 2007. "Clumped-isotope" geochemistry - The study of naturally-occurring, multiply-substituted isotopologues. *Earth Plane. Sci. Lett.* 262, 309-327.
- Eiler, J.M., 2011. Paleoclimate reconstruction using carbonate clumped isotope thermometry. *Quat. Sci. Rev.* 30, 3575–3588.

- Eiler, J.M., 2013. The isotopic Anatomies of Molecules and Minerals. *Annu Rev Earth Pl Sc.* 41, 411-441.
- Eiler, J.M., Bergquist, B., Bourg, I., Cartigny, P., Farquhar, J., Gagnon, A., Guo, W., Halevy, I., Hofmann, A., Larson, T.E., Levin, N., Schauble, E.A., Stolper, D., 2014. Frontiers of stable isotope geoscience. *Chem. Geol.* 372, 119-143.
- Erzinger, J., Wiersberg, T., Dahms, E., 2004. Real-time mud gas logging during drilling of the SAFOD Pilot Hole in Parkfield, CA. *Geophys. Res. Lett.* 31, L13S18.
- Evans, J.P., Chester, F.M., 1995. Fluid interactions in faults of the San Andreas system: Inferences from San Gabriel fault rock geochemistry and microstructures. *J. Geophys. Res.* 100, 13007-13020.
- Evans, M.A., Bebout, G.E., Brown, C.H., 2012. Changing fluid conditions during folding: An example from the central Appalachians. *Tectonophysics* 576-577, 99-115.
- French, M. E., Chester, F. M., Chester, J. S., 2015. Micro-mechanisms of creep in clay-rich gouge from the Central Deforming Zone of the San Andreas Fault, *J. Geophys. Res. Solid Earth* 120, 827–849, doi: 10.1002/2014JB011496.
- Fulton, P.M., Saffer, D.M., Harris, R.N., Bekins, B.A., 2004. Re-evaluation of heat flow data near Parkfield, CA: Evidence for a weak San Andreas Fault. *Geophys. Res. Lett.* 31, L15S15.
- Fulton, P.M., Saffer, D.M., 2008. Potential role of mantle-derived fluids in weakening the San Andreas Fault. *J. Geophys. Res.* 114, B07408.
- Ghosh, P., Adkins, J., Affek, H., Balta, B., Guo, W., Schauble, E.A., Schrag, D., Eiler, J.M., 2006. ^{13}C - ^{18}O bonds in carbonate minerals: A new kind of paleothermometer. *Geochim. Cosmochim. Acta* 70, 1439-1456.

- Gratier, J.-P., Richard, J., Mittempergher, S., Renard, F., Doan, M., Di Toro, G., Hadizadeh, J., Bertrand, A.M.B., 2009. Pressure solution as a mechanism for creep and sealing in active faults, evidence from the SAFOD samples. *Eos Trans. AGU*, 90(52), Fall Meet. Suppl. Abstract T21B-1800.
- Gratier, J.-P., Richard, J., Renard, F., Mittempergher, S., Doan, M.-L., Di Toro, G., Hadizadeh, J., Boullier, A.-M., 2011. Aseismic sliding of active faults by pressure solution creep: Evidence from the San Andreas Fault Observatory at Depth. *Geology* 39, 1131-1134.
- Hadizadeh, J., Mittempergher, S., Gratier, J.-P., Renard, F., Di Toro, G., Richard, J., Babaie, H.A., 2012. A microstructural study of fault rocks from the SAFOD: Implications for the deformation mechanisms and strength of the creeping segment of the San Andreas Fault. *J. Struct. Geol.* 42, 246-260.
- Hayes, M.J., Boles, J., 1993. Evidence for meteoric recharge in the San Joaquin basin, California provided by isotope and trace element chemistry of calcite. *Mar. and Petrol. Geol.* 10, 135-144.
- Hardebeck, J.L., Hauksson, E., 1999. Role of fluids in faulting inferred from stress field signatures. *Science* 286, 236-239.
- He, B., Olack, G.A., Colman, A.S., 2012. Pressure baseline correction and high-precision CO₂ clumped-isotope (Δ_{47}) measurements in bellows and micro-volume modes. *Rapid Comm. Mass Spec.* 26, 2837-2853.
- Hickman, S.H., Zoback, M.D., 2004. Stress orientations and magnitudes in the SAFOD pilot hole. *Geophys. Res. Lett.* 31, L15S12.

- Holdsworth, R.E., van Diggelen, E.W.E., Spiers, C.J., de Bresser, J.H.P., Walker, R.J., Bowe, L., 2011. Fault rocks from the SAFOD core samples: Implications for weakening at shallow depths along the San Andreas Fault, California. *J. Struct. Geol.* 33, 132-144.
- Hodson, K.R., Crider, J.G., Huntington, K.W., in revision. Multi-stage cementation and paleo fluid temperature in a faulted sandstone reservoir, Moab Fault, Utah, USA. *Tectonophysics* (this volume).
- Huntington, K.W., Eiler, J.M., Affek, H.P., Guo, W., Boniface, M., Yeung, L.Y., Thiagarajan, N., Passey, B., Tripathi, A., Daeron, M., Came, R., 2009. Methods and limitations of 'clumped' isotope (Δ_{47}) analysis by gas-source isotope ratio mass spectrometry. *J. Mass Spec.* 44, 1318-1329.
- Huntington, K.W., Lechler, A.R., 2015. Carbonate clumped isotope thermometry in continental tectonics. *Tectonophysics* 647-648, 1-20.
- Imber, J., Holdsworth, R.E., Smith, S.A., Jefferies, S.P., Collettini, C., 2008. Frictional-viscous flow, seismicity and the geology of weak faults: a review and future directions. In: Wibberly, C.A., Kurz, W., Imber, J., Holdsworth, R.E., Collettini, C., (Eds.), *The internal structure of fault zones: Implications for mechanical and fluid-flow properties*. *The Geo. Soc. Lond.* 299, 151-173.
- Johnson, P.A., Mc Evilly, T.V., 1995. Parkfield seismicity: fluid driven? *J. Geophys. Res.*, 100, B7, 12937-12950.
- Kawabe, I., 1978. Calculation of oxygen-isotope fractionation in quartz-water system with special reference to the low temperature fractionation. *Geochim. Cosmochim. Acta* 42, 613-621.

- Kennedy, B.M., Kharaka, Y.K., Evans, W.C., Ellwood, A., DePaolo, D.J., Thordsen, J., Ambats, G., Mariner, R.H., 1997. Mantle fluids in the San Andreas Fault System, California. *Science* 278, 1278-1280.
- Kharaka, Y.K., Berry, A.F., 1973. Isotopic composition of oil-field brines from Kettleman North Dome, California, and their geologic implications. *Geochim. Cosmochim. Acta* 37, 1899-1908.
- Kharaka, Y.K., Thordsen, J.J., Evans, W., 1999. Geochemistry and hydromechanical interactions of fluids associated with the San Andreas Fault system, California. *Am. Geophys. Union, Geophysical Monograph* 113, 129-148.
- Kirby, S.H., Wang, K., Brocher, T.M., 2014. A large mantle water source for the northern San Andreas fault system: a ghost of subduction past. *Earth, Planets, and Space* 66, 1-18.
- Kirschner, D.L., Masson, H., Sharp, Z.D., 1999. Fluid migration through thrust faults in the Helvetic nappes (Western Swiss Alps). *Contrib. Mineral. Petrol.*, 136, 169-183.
- Kirschner, D.L., Kennedy, L.A., 2001. Limited syntectonic fluid flow in carbonate-hosted thrust faults of the Front Ranges, Canadian Rockies, inferred from stable isotope data and structures. *J. Geophys. Res.* 106, B6, 8827-8840.
- Kluge, T., John, C.M., Jourdan, A-L., Davis, S., Crawshaw, J., 2015. Laboratory calibration of the calcium carbonate thermometer in the 25-250 °C temperature range. *Geochim. Cosmochim. Acta* 157, 213-227.
- Lachenbruch A.H., Sass, J.H., 1980. Heat flow energetics of the San Andreas Fault Zone. *J. Geophys. Res.* 85, 6185-6222.

- Laubach, S.E., Diaz-Tushman, K., 2009. Laurentian paleostress trajectories and ephemeral fracture permeability, Cambrian Eriboll Formation sandstones west of the Moine Thrust Zone, NW Scotland. *J. Geol. Soc.* 166, 349-362.
- Lewicki, J.L., Evans, W.C., Hilley, G.E., Sorey, M.L., Rogie, J.D., Brantley, S.L., 2003. Shallow soil CO₂ flow along the San Andreas and Calaveras Faults, California.
- Lockner, D. A., Morrow, C., Moore, D., Hickman, S., 2011. Low strength of deep San Andreas fault gouge from SAFOD core. *Nature*. doi:10.1038/nature09927.
- Loyd, S.J., Dickson, J.A.D., Scholle, P.A., Tripathi, A.K., 2013. Extensive, uplift-related and non-fault-controlled spar precipitation in the Permian Capitan Formation. *Sedimentary Geol.* 298, 17-27, doi: 10.1016/j.sedgeo.2013.10.001.
- Margaritz, M., Taylor, H.P., 1976. Oxygen, hydrogen, and carbon isotope studies of the Franciscan formation, Coast Ranges, California. *Geochim. Cosmochim. Acta* 40, 215-234.
- Marrett, R., Laubach, S.E., 1997. Diagenetic controls on fracture permeability and sealing. *Int. J. Rock Mech. & Min. Sci.* 34, 3-4, Paper No. 204.
- Mittempergher, S., Di Toro, G., Gratier, J.P., Hadizadeh, J., Smith, S.A.F., Spiess, R., 2011. Evidence of transient increases of fluid pressure in SAFOD phase III cores. *Geophys. Res. Lett.* 38, L03301.
- Moore, D.E. and Rymer, M.J., 2007. Talc-bearing serpentinite and the creeping section of the San Andreas fault. *Nature*, 448, 795-797.
- Moore, D.E., and Rymer, M.J. (2012), Correlation of clayey gouge in a surface exposure of serpentinite in the San Andreas Fault with gouge from the San Andreas Fault Observatory at Depth (SAFOD). *J. Struct. Geol.*, 38, 51-60, doi:10.1016/j.jsg.2011.11.014.

- Morrow, C.A., Lockner, D.A., Moore, D.E., Hickman, S., 2014. Deep permeability of the San Andreas Fault from San Andreas Fault Observatory at Depth (SAFOD) core samples. *J. Struct. Geol.* 64, 99-114.
- Noda, H., Dunham, E.M., Rice, J.R., 2009. Earthquake ruptures with thermal weakening and the operation of major faults at low overall stress levels. *J. Geophys. Res.* 114, B07302.
- O'Neil, J.R., Clayton, R.N., Mayeda, T.K., 1969. Oxygen isotope fractionation in divalent metal carbonates. *J. Chem. Phys.* 51, 5547-5558.
- Pili, É, Poitrasson, F., Gratier, J-P., 2002. Carbon-oxygen isotope and trace element constraints on how fluids percolate faulted limestones from the San Andreas Faults system: partitioning of fluid sources and pathways. *Chem. Geol.* 190, 231-250.
- Pili, É, Kennedy, B.M., Conrad, M.E., Gratier, J.-P., 2011. Isotopic evidence for the infiltration of mantle and metamorphic CO₂-H₂O fluids from below in faulted rocks from the San Andreas Fault system. *Chem. Geol.* 281, 242-252.
- Rice, J.R., 1992. Fault stress states, pore pressure distributions, and the weakness of the San Andreas fault, in Evans, B., and Wong, T.F., eds., *Earthquake mechanics and transport properties of rocks*: London, Academic Press, 475-503.
- Richard, J., Gratier, J-P., Doan, M-L., Boullier, A-M., Renard, F., 2014. Rock and mineral transformations in a fault zone leading to permanent creep: Interactions between brittle and viscous mechanisms in the San Andreas Fault. *J. Geophys. Res.* 119, 8132-8153.
- Rutter, E. H. 1976. The kinetics of rock deformation by pressure solution. *Phil. Trans. R. Soc. Lond.* 1976;A283:203-219.

- Rybacki, E., Janssen, C., Wirth, R., Chen, K., Wenk, H.-R., Stromeyer, D., Dresen, G., 2011. Low-temperature deformation in calcite veins of SAFOD core samples (San Andreas Fault) - Microstructural analysis and implications for fault rheology. *Tectonophysics* 509, 107-119.
- Sadofsky, S.J., Bebout, G.E., 2004. Field and isotopic evidence for fluid mobility in the Franciscan Complex: forearc paleohydrology to depths of 30 kilometers. *Int. Geol. Rev.* 46, 1053-1088.
- Schauble, E.A., Ghosh, P., Eiler, J.M., 2006. Preferential formation of ^{13}C - ^{18}O bonds in carbonate minerals, estimated using first-principles lattice dynamics. *Geochim. Cosmochim. Acta* 70, 2510-2529.
- Schleicher, A.M., Tourscher, S.N., van der Pluijm, B.A., Warr, L.N., 2009. Constraints on mineralization, fluid-rock interaction, and mass transfer during faulting at 2-3 km depth from the SAFOD drill hole. *J. Geophys. Res.* 114, B04202.
- Schleicher, A.M., van der Pluijm, B.A., War, L.N., 2010. Nanocoatings of clay and creep of the San Andreas fault at Parkfield, California. *Geology* 38, 667-670.
- Sleep, N.H., and Blanpied, M.L., 1992. Creep, compaction and the weak rheology of major faults. *Nature* 359, 687-692.
- Sibson, R.H., 1990. Conditions for fault-valve behavior. *Geol. Soc. Lond. Spec. Pub.* 54, 12-28.
- Sibson, R.H., 1992. Implications of fault-valve behavior for rupture nucleation and recurrence. *Tectonophysics*, 211, 283-293.
- Suchecki, R.K., Land, L.S., 1983. Isotopic geochemistry of burial-metamorphosed volcanogenic sediments, Great Valley sequence, northern California. *Geochim. Cosmochim. Acta* 47, 1487-1499.

- Swanson, E.A., Wernicke, B.P., Eiler, J.M., Losh, S., 2012. Temperatures and fluids on faults based on carbonate clumped-isotope thermometry. *Am. J. Sci.* 312, 1-21.
- Thordsen, J.J., Evans, W.C., & Kharaka, Y.K., 2010. Geochemistry of formation fluids from the SAFOD wells, Parkfield, California. *Eos Trans. AGU, Fall Meet. Suppl.* Abstract T41A-2098.
- Thordsen, J.J., Evans W.C., Kharaka, Y.K., Kennedy, B.M., & van Soest, M., 2005. Chemical and isotopic composition of water and gases from the SAFOD wells: implications to the dynamics of the San Andreas Fault at Parkfield, California. *Eos Trans. AGU, Fall Meet. Suppl.* Abstract T23E-08.
- Thompson, J.M., & White, L.D., 1991. Chemical analysis of water from the GTA-1 well, Parkfield, California, and other nearby spring and well waters. *USGS OFR 91-0003.*
- Titus, S.J., Dyson, M., DeMets, C., Tikoff, B., Rolandone, F., Bürgmann, R., 2011. Geologic versus geodetic deformation adjacent to the San Andreas fault, central California. *Bull. Geo. Soc. Am.* 123, 794-820.
- Vrolijk, P., and van der Pluijm, B.A., 1999. Clay gouge. *J. Struct. Geol.* 21, 1039-1048.
- Wiersberg, T., and Erzinger, J., 2008. Origin and spatial distribution of gas at seismogenic depths of the San Andreas Fault from drill-mud gas analysis. *Appl. Geochem.* 23, 1675-1690.
- Wiersberg, T., and Erzinger, J., 2011. Chemical and isotope compositions of drilling mud gas from the San Andreas Fault Observatory at Depth (SAFOD) boreholes: Implications on gas migration and the permeability structure of the San Andreas Fault. *Chem. Geol.* 284, 148-159.
- Wintsch, R.P., Cristoffersen, R., Kronenberg, A.K., 1995. Fluid-rock reaction weakening of fault zones. *J. Geophys. Res.* 100, 13021-13032.

- Wood, J.R., Boles., J.R., 1991. Evidence for episodic cementation and diagenetic recording of seismic pumping events, North Coles Levee, California, U.S.A. *Appl. Geochem.* 6, 509-521.
- Wycherly, H., Fleet, A., Shaw, H., 1999. Some observations on the origins of large volumes of carbon dioxide accumulations in sedimentary basins. *Mar. and Petrol. Geol.* 16, 489-494.
- Zheng, Y.-F., 1993. Calculation of oxygen isotope fractionation in hydroxyl-bearing silicates. *Earth Planet. Sci. Lett.* 120, 247-263.
- Zoback, M.D., Zoback, M.L., Mount, V.S., Suppe, J., Eaton J.P., Healy, J.H., Oppenheimer, D., Reasenber, P., Jones, L., Raleigh, C.B., Wong, I.G., Scotti, O., Wentworth, C., 1987. New evidence on the state of stress of the San Andreas fault. *Science* 238, 1105-1111.
- Zoback, M.D., Hickman, S.H., Ellsworth, B., 2010. Scientific drilling into the San Andreas fault zone. *Eos: Transactions of the American Geophysical Union* 91 (22), 197-199.
- Zoback, M.D., Hickman, S., Ellsworth, W., SAFOD Science Team, 2011. Scientific drilling into the San Andreas Fault Zone - An overview of SAFOD's first five years: *Scientific Drilling*, no. 11, 14-28.

Constraints on paleofluid sources using the clumped-isotope thermometry of carbonate veins from the SAFOD (San Andreas Fault Observatory at Depth) borehole

P. Benjamin Luetkemeyer^a *corresponding author*

David L. Kirschner^a

Katharine W. Huntington^b

Judith S. Chester^c

Frederick M. Chester^c

James P. Evans^d

^aDepartment of Earth and Atmospheric Sciences, Saint Louis University, 205 O'Neil Hall, 3642 Lindell Blvd, Saint Louis, MO, 63108, luetkepb@slu.edu, david.kirschner@shell.com

^bDepartment of Earth and Space Sciences, Box 351310, University of Washington, Seattle, WA, 98195, kate1@uw.edu

^cDepartment of Geology and Geophysics, Texas A & M University, College Station, TX 77843, chesterj@tamu.edu, chesterf@tamu.edu

^dDepartment of Geology, Utah State University, Logan, UT, 84322-4505, james.evans@usu.edu

Keywords: SAFOD, clumped-isotope thermometry; calcite veins; fluids; faults

Abstract

The San Andreas Fault Observatory at Depth (SAFOD), near Parkfield, California, is a borehole drilled through two active deforming zones of the San Andreas fault, the Southwest Deforming Zone (SDZ) and the Central Deforming Zone (CDZ). These zones accommodate displacement by seismic slip and aseismic creep. Elevated fluid pressures and fluid-rock interactions have been proposed to explain the low apparent strength and aseismic creep observed, but the origin of the fluids and existence of high fluid pressures remains uncertain. We

use clumped-isotope thermometry and $\delta^{18}\text{O}$ - $\delta^{13}\text{C}$ compositions of calcite in veins to constrain the origin of paleofluids and compare these results to the isotopic composition of modern-day pore fluids from the SAFOD borehole and nearby areas. We observe that: (1) calcite vein temperatures vary from 81 to 134 °C, which overlaps the current ambient borehole temperatures of 110-115 °C at sampled depths; (2) vein calcite is not in carbon isotope equilibrium with modern-day pore fluids; (3) the $\delta^{18}\text{O}$ values of paleofluids close to the SDZ and CDZ, calculated from vein $\delta^{18}\text{O}$ and temperature data, are not in equilibrium with local modern-day pore waters but approach equilibrium with modern pore waters far from these zones; and (4) syntectonic vein calcite is only in C- and O-isotopic equilibrium with their host rocks within the SDZ and CDZ. Spatial patterns of $\delta^{18}\text{O}$ and $\delta^{13}\text{C}$ show little evidence for across-fault fluid-flow. Clumped isotope temperatures are consistent with locally-derived fluid sources, but not with continuous or episodic replenishment of fluids from shallow sedimentary brines or deep fluid sources. Our findings are compatible with flow of meteoric fluids from the southwestern damage zone into the SDZ and CDZ, which would have favored the formation of weak phyllosilicates and contributed to the present day weakness of the two actively deforming zones.

Keywords: SAFOD; clumped isotope thermometry; calcite veins; fluids; faults

1. Introduction

The San Andreas Fault zone (SAFZ) accommodates displacement between the Pacific and North American Plates without producing an observable heat anomaly (e.g., Lachenbruch and Sass, 1980; Fulton et al., 2004) and under stress conditions considered unfavorable for shear failure (Zoback et al., 1987; Hickman and Zoback, 2004). These observations and others are consistent with the San Andreas Fault being mechanically weak. Numerous models have been proposed to explain this apparent weakness (Byerlee, 1990; Sibson, 1992; Sleep and Blanpied,

1992; Rice, 1992; Johnson and McEvilly, 1995; Kennedy et al., 1997; Hardebeck and Hauksson, 1999; Moore and Rymer, 2007; Fulton and Saffer, 2008; Noda et al., 2009; Mittempergher et al., 2011; Richard et al., 2014).

Many explanations of weakening require that fluids are present within the SAFZ, and it is well known that fluids play a critical role in controlling the chemical and physical conditions in and around fault zones (e.g., Wintsch et al., 1995; Evans and Chester, 1995). For example, high fluid pressures can reduce the effective normal stress within a fault zone causing a decrease in fault strength (e.g., Rice, 1992, Byerlee, 1993). Fluids can act to enhance mass-transfer processes within fault zones that can lead to fault weakening or strengthening (e.g., Rutter, 1976; Gratier et al., 2011). A number of studies provide evidence that fluid-rock reactions lead to the crystallization of phyllosilicates that cannot support high shear stresses due to their low coefficients of friction (e.g., Wintsch et al., 1995; Vrolijk and van der Pluijm, 1999; Imber et al., 2008; Lockner et al., 2011; French et al., 2015). It is likely that a combination of these processes operate within the SAFZ (e.g., Holdsworth et al., 2011; Bradbury et al., 2011; Hadizadeh et al., 2012; Richard et al., 2014; Bradbury et al., 2015).

The spatial distribution and geochemical variation of carbonate veins in the SAFZ provide constraints needed to test models of fault weakening. Stable-isotope geochemistry and fluid-inclusion analyses of syn- and post-kinematic veins are routinely used in paleofluid studies to constrain the thermal conditions during vein formation, fluid origin, and changing fluid chemistry in a number of tectonic settings (e.g. Kirschner et al., 1999; Kirschner and Kennedy, 2001; Pili et al., 2002; Boles et al., 2004; Beaudoin et al., 2011; Pili et al., 2011; Evans et al., 2012; Swanson et al., 2012; Bergman et al., 2013; Huntington and Lechler, 2015). Veins often form in fracture networks that can greatly influence permeability and fluid migration,

particularly if incomplete cementation occurs (Marrett and Laubach, 1997; Laubach and Diaz-Tushman, 2009). Further, the spatial distribution of veins can be used to construct a model of the temporal variations in fluid-flow processes that could significantly influence seismic processes at depth.

The goal of this study is to determine the sources and temperatures of paleofluids that contributed to vein formation in two actively deforming zones within the San Andreas Fault (SAF) at the San Andreas Fault Observatory at Depth (SAFOD). We use conventional oxygen and carbon isotopic analyses and recently developed techniques of clumped-isotope analysis. The results provide constraints on fluid-flow models in the San Andreas Fault at seismogenic depths.

2. Background

2.1 Geologic setting of SAFOD

The SAFOD Observatory, a part of the Earthscope initiative, has provided access to rocks from the top of the seismogenic zone of the SAFZ. The SAFZ consists of a broad northwest-trending zone of deformation that accommodates right-lateral motion between the North American and Pacific tectonic plates (e.g., Titus et al., 2011). The SAFOD borehole, spudded approximately 1.8 km southwest of the surface trace of the SAFZ near the city of Parkfield, CA (Fig. 1), is located along a segment of the fault zone that exhibits both creep and microseismic-slip behavior. A vertical pilot hole was drilled to 2.2 km true vertical depth (TVD) in 2002. From the same drill pad, the main hole was drilled in three phases between 2004 and 2007. Phase 1 drilling in 2004 reached a TVD of 1.5 km along a vertical path, and then was deviated 55° to an inclined orientation of 35° towards N35°E for approximately 2.5 km TVD. Phase 2 drilling in 2005 extended the main borehole to a TVD of ~3.2 km across the geologic boundary

between the Pacific and North American Plates. Phase 3 drilling in 2007 resulted in several multilaterals being drilled through the steel casing of the main borehole at ~2.5 km depth.

During Phase 2 drilling, a 200-meter wide damage zone was defined on the basis of P-wave (V_p) and S-wave (V_s) velocities and relatively low resistivity values. This damage zone is between 3157 and 3400 meters measured depth (m MD; Fig. 1), within the Great Valley Group. Casing deformation revealed two active fault strands at 3192 and 3302 m MD, referred to as the Southwest Deforming Zone (SDZ) and Central Deforming Zone (CDZ), respectively (Zoback et al., 2010; 2011). As part of Phase 3 drilling, several multilateral cores were acquired within the arkosic sedimentary rocks and in the low velocity interval in order to sample rocks within and near the SDZ and CDZ.

2.2 Description of core and veins

The cores acquired in 2007 were cut, cleaned, photographed, logged, mapped, and sampled by several co-authors of this report. The cores are curated at the IODP's Gulf Coast Repository in College Station, Texas. Detailed geologic descriptions of the rocks and interpretations of the deformation features of the Phase 2 and Phase 3 cores have been subsequently provided in other studies (Bradbury et al., 2007; Bradbury et al., 2011; Holdsworth et al., 2011; Mittempergher et al., 2011; Rybacki et al., 2011; Gratier et al., 2011; Hadizadeh et al., 2012, and references therein). Here we provide a brief description of the units that we documented in the core samples at the well site, and later sampled for this study.

Foliated sandstone-siltstone-shale from 3186 - 3194 m MD contains thin cross-cutting vein-fill cements found primarily in irregular-shaped lenses of siltstone to very fine sandstones surrounded by foliated siltstone and shale cataclasite (Fig. A.1 and A.2, see supplementary figures in Appendix A). Carbonate within the sheared shales occurs as highly disaggregated vein

material. A sample collected at 3189 m MD by Rybacki et al. (2011) revealed the presence of several generations of cross-cutting veins interpreted to have formed as open-mode fractures with the youngest generation overprinting the fabric related to faulting. Indurated black ultracataclasite (3194.0-3196.4 m MD; Fig. A.3) is cross-cut by thin calcite veins and calcite cemented faults (e.g. at 3194.08 m MD).

An abrupt transition to brown fault gouge at the base of the black ultracataclasite unit occurs at 3196.4 m MD. The brown fault gouge is foliated, contains clasts of serpentinite, and is spatially associated with the actively creeping SDZ (3196.4-3198.1 m MD). Abundant intact calcite veins are present in a 30 cm serpentinite block within the brown gouge (Fig. A.3). The veins are oriented at both high and low angles relative to the core axis. Near the base of the serpentinite-bearing section of core, the veins are sheared and reoriented at the contact with the brown foliated fault gouge below.

The rocks from 3295.1 to 3297.1 m MD (Fig. A.4) are characterized by alternating bands of greenish-gray and more deformed reddish-brown foliated sandstones and siltstones that are crosscut by numerous small faults. Calcite veins several millimeters thick are abundant in the greenish-gray units and oriented at high angles to the overall shear foliation. Foliated brown fault gouge associated with the CDZ (3297.1-3299.1 m MD) contains porphyroclasts of serpentinite, siltstone, and sandstone. Numerous thin, short calcite veins oriented subparallel to the core axis are preserved in the serpentinite clasts. The sheared silty shale (3299.1-3301.5; Figs. A.5 and A.6), located below the CDZ, contains numerous moderately deformed calcite veins that are oriented subperpendicular to the core axis, and small cross-cutting veins within lenticular clasts of fine siltstone that do not extend into the surrounding sheared shale. Petrographic analysis of a calcite vein sampled at 3300 m MD by Rybacki et al. (2011) found irregularly shaped carbonate

veinlets coating fractured grain boundaries. Greenish-black sheared siltstone grades into relatively undeformed massive siltstone (Fig. A.6) from 3301.5 to 3303.3 m MD. Calcite cements fill small dilational jogs of shear fractures that are oriented subparallel to the core axis. A sharp, inclined contact is observed at 3303.3 m MD (Fig. A.7) that juxtaposes the relatively undeformed massive siltstone against a dark gray foliated siltstone-sandstone-shale unit extending to 3307.4 m MD. Calcite veins are preserved in clasts and thin layers of interbedded sandstone and shale. Calcite occurs as intact fracture fill oriented at intermediate angles to the core axis in more massive fine sandstone and siltstone units. Some of the most strongly deformed veins were documented within this interval at 3307 m MD by Rybacki et al. (2011). Sheared and fractured calcareous siltstone and claystone (3307.4-3311 m MD) contain intact calcite vein-fill cements preserved within clasts of siltstone. Comminuted calcite fragments are preserved within the sheared claystone layers.

2.3 Previous work: Petrography of SAFOD veins

Rybacki et al. (2011) documented multiple generations of calcite veins ranging from relatively undeformed to highly deformed. The youngest veins cross-cut the dominant fault-related fabric based on the relationships observed in four samples taken at 3141, 3189, 3300, and 3307 m MD. Homogenous yellow to orange calcite luminescence for these veins were interpreted to represent relatively fast cement precipitation from a single fluid pulse (Rybacki et al., 2011).

Mittempergher et al. (2011) documented carbonates in fractures and dilational jogs sampled within meters of the SDZ to have orientations consistent with overall right-lateral displacement of the SAF. The same study reported alternating light and dark calcite luminescence rims in stretched and elongate calcite grains that were interpreted to represent post-

fracturing changes in fluid compositions.

Holdsworth et al. (2011) in a comprehensive study of 38 thin sections of the Phase 3 core concluded that the calcite-filled veins formed just before and synchronous with the development of fault gouge. Additionally, Holdsworth et al (2011) documented an increase in veining towards the SDZ and CDZ.

2.4 Previous work: San Andreas fault gases and fluids

2.4.1 SAFOD borehole

The dominant carbon-bearing gases in the SAFOD borehole were carbon dioxide (CO₂) and methane (CH₄) (Wiersberg and Erzinger, 2008) and were present in the drilling mud throughout the drill hole (Erzinger et al., 2004; Wiersberg and Erzinger, 2008; 2011). At depths less than 770 m in the SAFOD pilot hole, the C₁/(C₂+C₃) ratios of the gases locally exceeded 2000, consistent with a biogenic origin for most, if not all, of the methane. At depths greater than 3 km, the C₁/(C₂+C₃) ratios of the hydrocarbons were lower than 10, consistent with a thermogenic origin of the methane (Wiersberg and Erzinger, 2011). The gases between approximately 770 m and 3000 m depths (MD) were of intermediate ratios and potentially mixtures of thermogenic and biogenic origin.

The δ¹³C values of the CO₂ mud gas ranged from -23 to -16 ‰ (Vienna PeeDee Belemnite, VPDB), consistent with an organic origin for the CO₂ (Wiersberg and Erzinger (2008). At present-day downhole temperatures, the isotopic values of the methane and CO₂ gases are in disequilibrium leading Wiersberg and Erzinger (2011) to propose that the gases had undergone post-formation alteration/fractionation.

Stable isotope and noble gas studies on calcite veins (Pili et al., 2002; 2011) and spring waters (Kennedy et al., 2007) sampled along the SAFZ found evidence consistent with the

involvement of fluids containing some mantle CO₂. However, the $\delta^{13}\text{C}$ values of the mud gases sampled at SAFOD ($-26 < \delta^{13}\text{C} < -13$ ‰, VPDB; Wiersberg and Erzinger, 2008) are significantly lower than $\delta^{13}\text{C}$ values typical of mantle-derived CO₂ (-7 to -4 ‰, VPDB; Wycherley et al., 1999).

2.4.2 SAF regional

Many studies have used various geochemical methods to constrain the source(s) of fluids within the SAFZ and nearby sedimentary basins (Kharaka et al., 1973; Margaritz and Taylor, 1976; Suchecki and Land, 1983; Hayes and Boles, 1993; Wood and Boles, 1991; Davisson et al., 1994; Thompson and White, 1991; Kharaka et al., 1999; Campbell et al., 2002; Pili et al., 2002, 2011; Sadofsky and Bebout, 2004; Kirby et al., 2014). The body of evidence is consistent with fluids in the fault zone having exchanged isotopes with fluids from many local and external sources.

Suchecki and Land (1983) suggested, based on the oxygen isotope compositions of calcite cements and authigenic clays in Great Valley sediments of northern California, the calcite cements precipitated from formation fluids that had been buffered by the conversion of smectite to illite during diagenesis. Kharaka and Berry (1973) concluded that the $\delta^{18}\text{O}$ -depleted waters from the Middle Miocene Temblor Formation were meteoric in origin with the isotopic compositions having been controlled by exchange with carbonate cements, whereas $\delta^{18}\text{O}$ -enriched waters were representative of the original connate water released from the underlying Mesozoic sedimentary rocks. Further, Kharaka et al. (1999) found that δD and $\delta^{18}\text{O}$ values of various spring waters emanating from seismically active strands of the SAF were consistent with meteoric fluids having circulated down to 10 km depth. Thompson and White (1991) also reported $\delta^{18}\text{O}$ values collected from wells and springs emanating from the SAFZ within the

greater Parkfield area. The wide range of fluid oxygen isotope compositions led these authors to conclude that the fluid $\delta^{18}\text{O}$ values could be attributed to a number of processes including fluid-rock interaction in deep sedimentary basins, decomposition of organic matter, and the alteration of serpentinite.

3. Methods

3.1 Sampling

Carbonate veins and host rocks were selected for the isotopic analyses of carbon and oxygen in order to: (1) compare the isotopic compositions of veins and their hosts, (2) define variations in isotopic compositions as a function of lithology and structural position with distance away from the SDZ and CDZ, (3) constrain the temperature of vein precipitation and origin of fluids, and (4) determine the extent of fluid-rock interactions across the fault zone.

Vein material for stable isotopic analysis was sampled from Phase 2 drill cuttings and the Phase 3 core. The hand-picked cuttings contained variable amounts of grey non-calcareous host rock (siltstone, shale) and white calcite vein or breccia cement. We assume that the true depth of origin of the cuttings is approximated by the measured depths. Veins from the Phase 3 cores were microdrilled with a millimeter-diameter bit.

Eighty-one cutting samples from 3185 to 3946 m (MD) were analyzed. We used the systematic variations in stable isotopic compositions in this data set to establish the context for the data acquired from the Phase 3 cores. Sixty-three vein samples from the Phase 3 cores were analyzed for $\delta^{13}\text{C}$ and $\delta^{18}\text{O}$. Sample locations, photographs, and core descriptions are in Supplementary Figures A.1- A.8, and the Petrographic Atlas of the Phase 3 cores at URL http://www.earthscope.org/samples/safod_core_samples/. Ten veins near the SDZ and serpentinite-bearing CDZ were also analyzed for clumped-isotope thermometry.

3.2 Stable isotope analysis of carbon and oxygen

Carbonate was analyzed for $\delta^{13}\text{C}$ and $\delta^{18}\text{O}$ in the stable isotope laboratory at Saint Louis University. Approximately two milligrams of material were placed in glass vials, capped, and reacted with 100 % orthophosphoric acid at 90 °C for several hours in an automated sample-prep system. The evolved CO_2 was entrained in a helium stream to a continuous-flow, Micromass Isoprime isotope-ratio mass spectrometer for analysis. The mass-45 signal of data reported in this study ranged between 3 and 10nA. The $\delta^{13}\text{C}$ and $\delta^{18}\text{O}$ data are reported in permil (‰) relative to the Vienna Pee Dee belemnite (VPDB), and calculated values of $\delta^{18}\text{O}_{\text{porewater}}$ are reported in permil (‰) against Vienna Standard Mean Ocean Water (VSMOW). An in-house standard with an accepted $\delta^{13}\text{C}_{\text{VPDB}}$ value of -2.33 ‰ and $\delta^{18}\text{O}_{\text{VSMOW}}$ value of 24.72 ‰ relative to NBS19 ($\delta^{13}\text{C}_{\text{VPDB}} = 1.95$ ‰ and $\delta^{18}\text{O}_{\text{VSMOW}} = 28.64$ ‰) was analyzed on average with every five to six samples. The results of fifty-three in-house standard analyses had a standard deviation of 0.10 ‰ and 0.09 ‰ for $\delta^{13}\text{C}$ and $\delta^{18}\text{O}$, respectively.

3.3 Clumped isotope analysis

Carbonate clumped-isotope thermometry, a technique that constrains the temperature of mineral formation independent of the isotopic composition of the fluid from which it grew, is well suited to investigate paleofluids associated with cementation and deformation in fault zones (Bergman et al., 2013; Budd et al., 2013; Huntington and Lechler, 2015; Hodson et al., this volume). Carbonate clumped-isotope thermometry is based on the degree to which heavy isotopes ^{13}C and ^{18}O bond preferentially with, or near, each other relative to the more abundant light isotopes, ^{12}C and ^{16}O (Schauble et al., 2006; Ghosh et al., 2006; Eiler, 2007; 2011; 2013; Eiler et al., 2015). This "clumping" of heavy isotopes is thermodynamically favored at lower temperatures and thus records the temperature of mineral formation (Schauble et al., 2006). To

measure the state of ordering in a mineral, the carbonate is digested in acid to produce CO₂, and the abundance of mass-47 CO₂ molecules, most of which contain both ¹³C and ¹⁸O, is measured relative to the abundance expected for a random (stochastic) distribution of isotopes among isotopologues (Ghosh et al., 2006; Eiler, 2007). This over abundance, reported as the Δ₄₇ value, is independent of the initial bulk isotopic composition of the fluid (Ghosh, 2006). Thus, the δ¹⁸O of the fluid in equilibrium with the sampled carbonates can be calculated from the measured δ¹⁸O value of the carbonate sample and the temperature obtained from clumped-isotope thermometry. Such information from clumped isotope analysis has enabled previous workers to study interactions of geologic structures, fluid flow and cementation (Swanson et al., 2012; Bergman et al., 2013; Loyd et al., 2013; Budd et al., 2013).

Clumped-isotope analyses (δ¹³C, δ¹⁸O, Δ₄₇) were carried out at the University of Washington (UW) on a subset of the samples analyzed for δ¹³C and δ¹⁸O at Saint Louis University. Calcium carbonate samples (6 to 8 mg) were digested in phosphoric acid at 90 °C for 10 minutes. The evolved CO₂ was cryogenically separated from water on an automated stainless steel vacuum line, passed through a Porapak Q trap held between -10 °C and -20 °C using helium as the carrier gas, and transferred to a Pyrex break seal tube. Carbonate standards (NBS-19 and C64 reagent-grade calcite intralaboratory standard) and CO₂ reference gases (equilibrated at 4, 60, and 1000 °C) were purified in the same manner as the samples. Break seals were loaded into an automated 10-port tube cracker inlet system and analyzed on a Thermo MAT 253 configured to measure masses 44 to 49 inclusive. Sample and reference bellows were expanded to 100 % and filled with equal pressures of sample CO₂ and UW ‘fermented corn’ reference CO₂ (δ¹³C_{PDB} = -10.2 ‰, δ¹⁸O_{VSMOW} = -6.0 ‰; values calibrated using NBS-19), respectively. The mass-47 signal was used for peak centering, and bellows were adjusted to

produce a mass-47 signal of 2550 mV (~16 V for mass-44). Pressure baseline (PBL) was automatically measured using the technique of He et al. (2012), followed by 6 acquisitions of 10 sample-reference comparison cycles with 26-second integration times. Following each sample, water was monitored by measuring m/z 18 on the same cup as m/z 45. Δ_{47} values were calculated using methods established by Affek and Eiler (2006) and Huntington et al. (2009), and reported in the absolute reference frame (Dennis et al., 2011) using heated gas (1000 °C) and CO₂-water equilibration (4 and 60 °C) lines constructed during the corresponding analysis period.

Analyses with Δ_{48} values >2 ‰ indicate potential sample contamination and therefore were excluded. Because the analytical methods used in this study are similar to the methods and 90 °C phosphoric acid temperature used by Kluge et al. (2015) and references therein, we used the 90 °C acid Kluge et al. (2015), calibration (Equation 5) to calculate temperature ($T(\Delta_{47})$) from Δ_{47} . Calculated values of $\delta^{18}\text{O}$ and $\delta^{13}\text{C}$ were made using the following fractionation factors: $\delta^{18}\text{O}_{\text{calcite-water}}$ (O'Neil et al., 1969), $\delta^{18}\text{O}_{\text{quartz-water}}$ (Kawabe, 1978), $\delta^{18}\text{O}_{\text{calcite-serpentinite}}$ (Zheng, 1993), $\delta^{13}\text{C}_{\text{calcite-CO}_2}$ (Bottinga, 1968), and $\delta^{13}\text{C}_{\text{calcite-CH}_4}$ (Bottinga, 1969).

4. Results

A total of 145 samples were analyzed from the SAFOD borehole (Table 1). The $\delta^{13}\text{C}$ and $\delta^{18}\text{O}$ values of cements collected from both Phase 2 cuttings and Phase 3 drill cores are plotted together along with host rock $\delta^{13}\text{C}$ and $\delta^{18}\text{O}$ values (Fig. 2). Veins exhibit a wide range of carbon ($\delta^{13}\text{C} = -20$ ‰ to +7 ‰) and oxygen ($\delta^{18}\text{O} = -18$ ‰ to -4 ‰) isotopic values, whereas host rock values occur in a narrower range of carbon ($\delta^{13}\text{C} = -12$ ‰ to +9 ‰) and oxygen ($\delta^{18}\text{O} = -14$ ‰ to -6 ‰) values. The isotopic composition of veins shows little variation in carbon and oxygen for any individual lithology (Fig. 2). However, vein $\delta^{13}\text{C}$ and $\delta^{18}\text{O}$ values vary with depth and proximity to lithologic, SDZ, and CDZ contacts (Fig. 3).

Table 1. Stable isotope data of cuttings from the SAFOD borehole

| ^a Depth (feet MD) | ^a Depth (meters MD) | ^b $\delta^{13}\text{C}$ (‰, VPDB) | ^c $\delta^{18}\text{O}$ (‰, VSMOW) | ^c $\delta^{18}\text{O}$ (‰, VPDB) | ^d Sample Type |
|---------------------------------|-----------------------------------|---|--|---|-----------------------------|
| 10450 | 3185 | 8.3 | 22.5 | -8.2 | wr |
| 10490 | 3197 | -0.5 | 19.2 | -11.4 | wr |
| 10510 | 3203 | -6.8 | 21.5 | -9.1 | wr |
| 10510 | 3203 | -0.9 | 16.7 | -13.8 | v |
| 10530 | 3210 | -7.7 | 21.8 | -8.8 | wr |
| 10540 | 3213 | 2.0 | 14.0 | -16.4 | v |
| 10585 | 3226 | -9.3 | 20.2 | -10.4 | v |
| 10617 | 3236 | -11.0 | 21.5 | -9.2 | v |
| 10675 | 3254 | -11.1 | 20.7 | -9.9 | v |
| 10705 | 3263 | 2.5 | 13.8 | -16.6 | v |
| 10735 | 3272 | -5.1 | 19.7 | -10.9 | v |
| 10735 | 3272 | 2.9 | 14.6 | -15.9 | v |
| 10765 | 3281 | 2.2 | 14.7 | -15.7 | v |
| 10765 | 3281 | 2.8 | 15.1 | -15.4 | v |
| 10765 | 3281 | -5.4 | 20.2 | -10.4 | v |
| 10800 | 3292 | 2.3 | 15.0 | -15.5 | v |
| 10810 | 3295 | 1.0 | 15.2 | -15.2 | v |
| 10810 | 3295 | -9.6 | 19.7 | -10.9 | v |
| 10820 | 3298 | -8.5 | 20.7 | -9.9 | v |
| 10820 | 3298 | -3.5 | 19.6 | -11.0 | v |
| 10820 | 3298 | 2.5 | 13.5 | -16.9 | v |
| 10825 | 3299 | -6.0 | 18.5 | -12.0 | v |
| 10825 | 3299 | 0.2 | 16.1 | -14.4 | v |
| 10825 | 3299 | -9.4 | 20.1 | -10.5 | v |
| 10830 | 3301 | 1.7 | 14.5 | -15.9 | v |
| 10830 | 3301 | 2.4 | 14.3 | -16.1 | v |
| 10840 | 3304 | 2.4 | 15.3 | -15.2 | v |
| 10850 | 3307 | -9.0 | 19.8 | -10.8 | v |
| 10855 | 3309 | -15.9 | 12.7 | -17.7 | v |
| 10860 | 3310 | 2.8 | 12.9 | -17.5 | v |
| 10860 | 3310 | -3.6 | 20.5 | -10.1 | wr |
| 10860 | 3310 | -10.4 | 19.7 | -10.9 | v |
| 10860 | 3310 | 2.8 | 14.2 | -16.2 | v |
| 10870 | 3313 | -4.8 | 18.6 | -11.9 | v |
| 10870 | 3313 | -8.9 | 18.6 | -12.0 | v |
| 10870 | 3313 | -4.7 | 19.0 | -11.6 | v |
| 10880 | 3316 | -4.2 | 20.2 | -10.4 | wr |
| 10880 | 3316 | -11.7 | 19.5 | -11.1 | v |
| 10894 | 3320 | -4.6 | 19.2 | -11.3 | v |

Table 1. continued

| ^a Depth (feet MD) | ^a Depth (meters MD) | ^b $\delta^{13}\text{C}$ (‰, VPDB) | ^c $\delta^{18}\text{O}$ (‰, VSMOW) | ^c $\delta^{18}\text{O}$ (‰, VPDB) | ^d Sample Type |
|---------------------------------|-----------------------------------|---|--|---|-----------------------------|
| 10900 | 3322 | -4.6 | 20.2 | -10.4 | wr |
| 10900 | 3322 | -4.2 | 19.8 | -10.8 | v |
| 10900 | 3322 | 2.7 | 14.8 | -15.6 | v |
| 10920 | 3328 | -5.7 | 17.1 | -13.4 | wr |
| 10924 | 3330 | -4.5 | 19.0 | -11.6 | v |
| 10924 | 3330 | -7.4 | 19.7 | -10.9 | v |
| 10924 | 3330 | 3.5 | 13.8 | -16.6 | v |
| 10940 | 3335 | -3.7 | 21.4 | -9.3 | wr |
| 10954 | 3339 | 2.0 | 12.9 | -17.5 | v |
| 10954 | 3339 | 0.8 | 15.2 | -15.3 | v |
| 10960 | 3341 | -2.1 | 24.3 | -6.4 | wr |
| 10960 | 3341 | -8.9 | 19.8 | -10.8 | v |
| 10980 | 3347 | -4.2 | 23.0 | -7.7 | wr |
| 11011 | 3356 | -6.8 | 18.4 | -12.2 | v |
| 11011 | 3356 | -4.6 | 18.9 | -11.7 | v |
| 11011 | 3356 | 0.4 | 15.8 | -14.7 | v |
| 11041 | 3365 | -12.6 | 26.7 | -4.0 | v |
| 11074 | 3375 | -10.3 | 21.3 | -9.3 | v |
| 11163 | 3402 | -11.5 | 23.2 | -7.5 | v |
| 11190 | 3411 | 2.6 | 14.2 | -16.2 | v |
| 11252 | 3430 | -9.2 | 20.7 | -9.9 | v |
| 11252 | 3430 | 3.0 | 13.7 | -16.7 | v |
| 11290 | 3441 | 1.0 | 14.1 | -16.3 | v |
| 11290 | 3441 | -9.8 | 20.1 | -10.5 | v |
| 11340 | 3456 | -7.5 | 18.5 | -12.0 | v |
| 11370 | 3466 | -12.6 | 19.9 | -10.7 | v |
| 11420 | 3481 | -11.8 | 23.9 | -6.8 | wr |
| 11420 | 3481 | -2.1 | 14.2 | -16.2 | v |
| 11440 | 3487 | -8.7 | 20.6 | -10.0 | wr |
| 11460 | 3493 | -9.4 | 23.0 | -7.7 | wr |
| 11480 | 3499 | -10.3 | 24.0 | -6.7 | wr |
| 11480 | 3499 | -15.3 | 20.6 | -10.0 | v |
| 11500 | 3505 | -10.5 | 17.0 | -13.5 | wr |
| 11520 | 3511 | -10.1 | 18.6 | -12.0 | wr |
| 11540 | 3517 | -11.5 | 17.8 | -12.8 | wr |
| 11540 | 3517 | -10.4 | 20.9 | -9.7 | v |
| 11640 | 3548 | -10.2 | 19.1 | -11.5 | v |
| 11850 | 3612 | 1.2 | 14.5 | -15.9 | v |
| 11947 | 3641 | 1.8 | 14.6 | -15.9 | v |

Table 1. continued

| ^a Depth (feet MD) | ^a Depth (meters MD) | ^b $\delta^{13}\text{C}$ (‰,VPDB) | ^c $\delta^{18}\text{O}$ (‰,VSMOW) | ^c $\delta^{18}\text{O}$ (‰,VPDB) | ^d Sample Type |
|---------------------------------|-----------------------------------|--|---|--|-----------------------------|
| 11947 | 3641 | 2.0 | 14.4 | -16.0 | v |
| 12050 | 3673 | -12.0 | 18.7 | -11.9 | v |
| 12050 | 3673 | -9.0 | 20.2 | -10.4 | v |
| 12145 | 3702 | 3.8 | 14.1 | -16.3 | v |
| 12245 | 3732 | -14.5 | 19.6 | -11.0 | v |
| 12245 | 3732 | -13.3 | 19.2 | -11.3 | v |
| 12346 | 3763 | -7.6 | 21.9 | -8.7 | v |
| 12346 | 3763 | -18.9 | 19.6 | -11.0 | v |
| 12464 | 3799 | -6.5 | 19.2 | -11.4 | v |
| 12464 | 3799 | -12.9 | 19.1 | -11.4 | v |
| 12464 | 3799 | -5.6 | 18.9 | -11.6 | v |
| 12546 | 3824 | -17.5 | 19.1 | -11.4 | v |
| 12546 | 3824 | -6.5 | 20.2 | -10.4 | v |
| 12645 | 3854 | -19.6 | 19.5 | -11.1 | v |
| 12846 | 3915 | 0.5 | 23.8 | -6.9 | v |
| 12846 | 3915 | -6.4 | 19.0 | -11.6 | v |
| 12945 | 3946 | 3.2 | 14.8 | -15.6 | v |
| 12945 | 3946 | -5.7 | 18.8 | -11.8 | v |

^aDepths are reported in meters measured depth (MD) for phase 2 drilling.

^b $\delta^{13}\text{C}$ values of calcite are reported in per mil relative to Vienna Peedee Belemnite (VPDB).

^c $\delta^{18}\text{O}$ values are reported in per mil relative to both VPDB and Vienna Standard Mean Ocean Water (VSMOW).

^dwr-whole rock; v-calcite vein

Veins sampled within the foliated siltstone-shale cataclasite (3186.7 to 3193.9 m MD) exhibit a narrow range of isotopic signature (blue circles: $+1.0\text{‰} < \delta^{13}\text{C} < +5\text{‰}$; $-18\text{‰} < \delta^{18}\text{O} < -13\text{‰}$; Fig.3). The two veins sampled at the base of the foliated siltstone-shale cataclasite (3193.4 m MD) and at the lithologic contact with the black ultracataclasite (at 3194.1 m MD) have $\delta^{13}\text{C}$ (+0.4 to +1 ‰) and $\delta^{18}\text{O}$ (-13 to -11 ‰) values that are intermediate between those found in the overlying foliated siltstone-shale cataclasite and the underlying black ultracataclasite (black circles: $-7\text{‰} < \delta^{13}\text{C} < +1\text{‰}$; $-12\text{‰} < \delta^{18}\text{O} < -11\text{‰}$; Fig. 3). This zone marks a shift in the isotopic signatures of veins to the lower $\delta^{13}\text{C}$ and higher $\delta^{18}\text{O}$ values typical

of the veins within the serpentinite-bearing, foliated fault gouge (3196.4 to 3198.1 m MD) that correlates with the SDZ (green circles: $-16\text{‰} < \delta^{13}\text{C} < -10\text{‰}$; $-13\text{‰} < \delta^{18}\text{O} < -10\text{‰}$; Fig. 3). The samples from the serpentinite-bearing foliated fault gouge were all taken from veins cutting the large serpentinite block and show similar isotopic signatures; however, the two veins at the upper and lower boundaries of the block (at 3196.5 and 3197.0 m MD) have $\delta^{13}\text{C}$ values $\sim 10\text{‰}$ lower than the veins sampled in the nearby black ultracataclasite and $\sim 5\text{‰}$ lower than the other veins taken from the SDZ. Veins sampled within the SDZ have similar $\delta^{13}\text{C}$ and $\delta^{18}\text{O}$ values compared to the isotopic composition of the whole rock sample ($\delta^{13}\text{C}$ of -6.8‰ and $\delta^{18}\text{O}$ of -9.1‰) collected from Phase 2 cuttings at 3203 m MD (Fig. 3).

Vein samples in the CDZ exhibit a narrow range of $\delta^{18}\text{O}$ values (-11 to -13‰), whereas the $\delta^{18}\text{O}$ values of veins sampled below the CDZ (3295 to 3310 m MD) range from -14 to -5‰ (Fig. 3). Host-rock samples from cuttings within this same interval also exhibit little variation in carbon and oxygen compositions (orange squares: $-8\text{‰} < \delta^{13}\text{C} < -6\text{‰}$; $-10\text{‰} < \delta^{18}\text{O} < -8\text{‰}$; Fig. 3). The $\delta^{13}\text{C}$ values of veins from the sheared siltstone and sandstone (295.1 to 3297.1 m MD) vary from -10 to -4‰ (Fig. 3). An abrupt shift toward heavier carbon isotopic compositions occurs within the serpentinite-bearing fault gouge of the CDZ (brown circles: $1\text{‰} < \delta^{13}\text{C} < 4\text{‰}$) at 3297 m MD continuing into the underlying sheared silty shale units (yellow circles: $1\text{‰} < \delta^{13}\text{C} < 7\text{‰}$) to 3301.4 m MD (Fig. 3). The vein carbon isotope compositions are increasingly depleted in ^{13}C away from the CDZ in the following order: massive siltstone (yellow circles: $-6\text{‰} < \delta^{13}\text{C} < -2\text{‰}$), foliated sandstone-siltstone-shale (red circles: $-9\text{‰} < \delta^{13}\text{C} < -7\text{‰}$), and sheared calcareous siltstone-claystone (Fig. 3).

Clumped-isotope data (Table 2) from samples between 3196.7 and 3309.9 m MD yield Δ_{47} values of 0.486 to 0.620 ‰ (average analytical uncertainties of 0.021 ‰ , 1 standard error

Table 2. Stable and clumped isotope data of calcite veins from SAFOD borehole phase 3 multilateral cores.

| Sample ID ^a | Depth ^b (meters, MD) | $\delta^{13}\text{C}^c$ (‰, VPDB) | $\delta^{18}\text{O}^d$ (‰, VSMOW) | $\delta^{18}\text{O}^d$ (‰, VPDB) | Δ_{47} (‰) ARF ^e | ± 1 SE ^f (‰, analytical) | Sample Average Δ_{47} (‰), ARF | ± 1 SE (‰, external) | Temperature ^g (°C) | ± 1 SE (°C) |
|------------------------|------------------------------------|--------------------------------------|---------------------------------------|--------------------------------------|---------------------------------------|--|--|-----------------------------|----------------------------------|--------------------|
| G-R1-S1 7.3 cm | 3186.81 | 4.7 | 13.1 | -17.3 | | | | | | |
| G-R1-S1 10.7 cm | 3186.92 | 3.7 | 12.4 | -17.9 | | | | | | |
| G-R1-S1 65.5 cm | 3187.47 | 3.9 | 13.1 | -17.3 | | | | | | |
| G-R1-S2 0-3 cm | 3187.55 | 4.2 | 13.9 | -16.5 | | | | | | |
| G-R1-S4 0-4 cm | 3189.32 | 3.6 | 15.2 | -15.3 | | | | | | |
| G-R2-S2 33.7 cm | 3192.15 | 2.4 | 13.6 | -16.8 | | | | | | |
| G-R2-S2 36.2 cm | 3192.18 | 3.6 | 12.7 | -17.6 | | | | | | |
| G-R2-S2 37.0 cm | 3192.27 | 3.8 | 12.9 | -17.5 | | | | | | |
| G-R2-S2 64.3 cm | 3192.54 | 2.8 | 13.4 | -17.0 | | | | | | |
| G-R2-S2 66.0 cm | 3192.56 | 2.0 | 13.7 | -16.7 | | | | | | |
| G-R2-S2 69.1 cm | 3192.59 | 1.9 | 15.1 | -15.4 | | | | | | |
| G-R2-S2 70.3 cm | 3192.60 | 2.4 | 13.0 | -17.4 | | | | | | |
| G-R2-S2 73.4 cm | 3192.64 | 1.1 | 15.9 | -14.5 | | | | | | |
| G-R2-S2 81.6 cm | 3192.72 | 2.6 | 13.0 | -17.3 | | | | | | |
| G-R2-S3 10.1 cm | 3192.89 | 0.9 | 12.4 | -18.0 | | | | | | |
| G-R2-S3 16.6 cm | 3192.96 | 2.9 | 13.2 | -17.2 | | | | | | |
| G-R2-S3 16.7 cm | 3192.97 | 2.5 | 13.4 | -17.0 | | | | | | |
| G-R2-S3 25.9 cm | 3193.06 | 3.6 | 12.9 | -17.5 | | | | | | |
| G-R2-S3 30.6 cm | 3193.11 | 2.6 | 13.4 | -17.0 | | | | | | |
| G-R2-S3 62.4 cm | 3193.41 | 1.0 | 17.3 | -13.2 | | | | | | |
| G-R2-S4 39.9 cm | 3194.08 | 0.4 | 18.9 | -11.6 | | | | | | |
| G-R2-S6 34.5 cm | 3195.81 | -6.7 | 18.9 | -11.6 | | | | | | |
| G-R2-S6 45.6 cm | 3195.92 | -6.9 | 19.4 | -11.2 | | | | | | |
| G-R2-S7 31.6 cm | 3300.26 | -15.8 | 18.1 | -12.5 | | | | | | |
| G-R2-S7 39.8 cm | 3300.34 | -10.2 | 19.2 | -11.4 | 0.515 | 0.010 | 0.515 | 0.023 | 112 | 6 |
| G-R2-S7 46.5 cm | 3300.40 | -11.4 | 19.1 | -11.5 | 0.533 | 0.010 | 0.533 | 0.023 | 100 | 6 |

Table 2. continued

| Sample ID ^a | Depth ^b (meters, MD) | $\delta^{13}\text{C}^c$ (‰, VPDB) | $\delta^{18}\text{O}^d$ (‰, VSMOW) | $\delta^{18}\text{O}^d$ (‰, VPDB) | Δ_{47} (‰) ARF ^c | ± 1 SE ^f (‰, analytical) | Sample Average Δ_{47} (‰), ARF | ± 1 SE (‰, external) | Temperature ^g (°C) | ± 1 SE (°C) |
|------------------------|------------------------------------|--------------------------------------|---------------------------------------|--------------------------------------|---------------------------------------|--|--|-----------------------------|----------------------------------|--------------------|
| G-R2-S7 53.3 cm | 3196.74 | -10.6 | 20.1 | -10.5 | 0.580 | 0.008 | 0.549 | 0.031 | 81 | 8 |
| | | -10.6 | 20.1 | -10.5 | 0.518 | 0.008 | | | | |
| G-R2-S7 59.3 cm | 3196.80 | -11.3 | 18.4 | -12.1 | 0.486 | 0.009 | 0.486 | 0.023 | 134 | 6 |
| G-R2-S7 68.2 cm | 3196.89 | -11.2 | 19.1 | -11.5 | 0.524 | 0.008 | 0.510 | 0.010 | 115 | 3 |
| | | -11.2 | 19.2 | -11.4 | 0.492 | 0.011 | | | | |
| | | -11.2 | 19.1 | -11.4 | 0.515 | 0.009 | | | | |
| G-R2-S7 70.2 cm | 3196.91 | -10.5 | 18.8 | -11.8 | | | | | | |
| G-R2-S7 72.0 cm | 3196.93 | -10.9 | 19.3 | -11.3 | | | | | | |
| G-R2-S7 72.2 cm | 3196.93 | -11.0 | 19.2 | -11.4 | | | | | | |
| G-R2-S7 80.0 cm | 3197.01 | -16.0 | 18.5 | -12.0 | | | | | | |
| G-R4-S1 24.2 cm | 3295.14 | -6.7 | 17.7 | -12.8 | | | | | | |
| G-R4-S2 9.6 cm | 3295.87 | -9.2 | 17.6 | -12.9 | | | | | | |
| G-R4-S2 54.7 cm | 3296.33 | -9.3 | 17.6 | -12.9 | | | | | | |
| G-R4-S3 3.4 cm | 3296.60 | -4.4 | 18.0 | -12.5 | | | | | | |
| G-R4-S5 53 cm | 3299.10 | -4.9 | 19.0 | -11.6 | | | | | | |
| G-R4-S5 56.7 cm | 3299.14 | -5.0 | 19.1 | -11.5 | | | | | | |
| G-R4-S5 57-62 cm | 3299.18 | 3.1 | 19.0 | -11.6 | | | | | | |
| G-R4-S5 58.0 cm | 3299.15 | 1.6 | 18.1 | -12.4 | | | | | | |
| G-R4-S6 8.3 cm | 3299.43 | 3.5 | 19.5 | -11.1 | | | | | | |
| G-R4-S6 26.3 cm | 3299.61 | 4.2 | 19.0 | -11.6 | | | | | | |
| G-R4-S6 41.6 cm | 3299.76 | 6.6 | 20.5 | -10.1 | | | | | | |
| G-R4-S7 40.1 cm | 3300.31 | 3.3 | 18.5 | -12.1 | | | | | | |
| G-R5-S1 8.1 cm | 3300.47 | 3.5 | 17.3 | -13.3 | 0.514 | 0.009 | 0.514 | 0.023 | 113 | 6 |
| G-R5-S1 11.0 cm | 3300.50 | 4.1 | 19.2 | -11.3 | 0.529 | 0.008 | 0.529 | 0.023 | 103 | 6 |
| G-R5-S1 78.2 cm | 3301.17 | 3.1 | 19.6 | -11.0 | | | | | | |
| G-R5-S2 6.9 cm | 3301.34 | 5.5 | 20.8 | -9.8 | | | | | | |

Table 2. continued

| Sample ID ^a | Depth ^b (meters, MD) | $\delta^{13}\text{C}^c$ (‰, VPDB) | $\delta^{18}\text{O}^d$ (‰, VSMOW) | $\delta^{18}\text{O}^d$ (‰, VPDB) | Δ_{47} (‰) ARF ^e | ± 1 SE ^f (‰, analytical) | Sample Average Δ_{47} (‰), ARF | ± 1 SE (‰, external) | Temperature ^g (°C) | ± 1 SE (°C) |
|------------------------|------------------------------------|--------------------------------------|---------------------------------------|--------------------------------------|---------------------------------------|--|--|-----------------------------|----------------------------------|--------------------|
| G-R5-S2 9.8 cm | 3301.37 | 1.2 | 20.2 | -10.4 | 0.522 | 0.008 | 0.519 | 0.003 | 109 | 1 |
| | | 1.2 | 20.3 | -10.3 | 0.517 | 0.009 | | | | |
| G-R5-S2 18.3 cm | 3301.45 | 1.3 | 17.1 | -13.4 | 0.564 | 0.009 | 0.564 | 0.023 | 82 | 6 |
| G-R5-S3 3.4 cm | 3302.24 | -4.3 | 17.7 | -12.8 | 0.496 | 0.009 | 0.496 | 0.023 | 126 | 6 |
| G-R5-S3 12.4 cm | 3302.32 | -2.9 | 17.9 | -12.6 | | | | | | |
| G-R5-S3 78.2 cm | 3302.93 | -4.0 | 17.5 | -13.0 | | | | | | |
| G-R5-S4 19.8 cm | 3303.00 | -5.3 | 17.9 | -12.7 | 0.493 | 0.008 | 0.529 | 0.036 | 103 | 9 |
| | | -5.3 | 17.8 | -12.7 | 0.565 | 0.008 | | | | |
| G-R5-S4 61.1 cm | 3303.50 | -8.3 | 20.2 | -10.4 | | | | | | |
| G-R5-S5 28.4 cm | 3304.00 | -7.3 | 17.9 | -12.6 | | | | | | |
| G-R5-S5 67.1 cm | 3304.39 | -9.0 | 19.0 | -11.5 | | | | | | |
| G-R6-S1 33.1 cm | 3307.73 | -10.1 | 21.6 | -9.1 | | | | | | |
| G-R6-S1 35.8 cm | 3307.76 | -12.5 | 18.4 | -12.1 | | | | | | |
| G-R6-S1 49.8 cm | 3307.90 | -18.8 | 25.3 | -5.4 | 0.620 | 0.009 | 0.593 | 0.014 | 67 | 4 |
| | | -18.8 | 25.2 | -5.6 | 0.571 | 0.009 | | | | |
| | | -18.9 | 25.2 | -5.6 | 0.587 | 0.008 | | | | |
| G-R6-S3 63.7 cm | 3309.80 | -13.7 | 20.3 | -10.3 | 0.579 | 0.010 | 0.549 | 0.030 | 91 | 8 |
| | | -13.8 | 20.3 | -10.3 | 0.519 | 0.009 | | | | |
| G-R6-S3 65.4 cm | 3309.97 | -14.0 | 21.9 | -8.7 | | | | | | |

^aSample identifier represents Hole-Run-Section-Distance (cm)

^bDepths are reported in meters measured depth (MD) for phase 3 drilling.

^c $\delta^{13}\text{C}$ values of calcite are reported in per mil relative to Vienna Pee Dee Belemnite (VPDB).

^d $\delta^{18}\text{O}$ values are reported in per mil relative to both VPDB and Vienna Standard Mean Ocean Water (VSMOW).

^e Δ_{47} values are reported in the absolute reference frame (ARF) of Dennis et al. (2011).

^fStandard error (SE) for samples not externally replicated reflect actual analytical error for the sample, or long-term error in standard analyses (0.023 ‰), whichever is larger.

^gTemperatures calculated using the calibration of Kluge et al. (2015).

(1SE)), corresponding to calcite formation temperatures of 67 to 134 °C, with average uncertainties of ± 5 °C considering the analytical error. Clumped-isotope temperatures for veins sampled in the serpentinite-bearing fault gouges of the SDZ at 3197.9 m MD (134 ± 2 °C, 1SE) and in the sheared massive siltstone unit approximately 2 m below the CDZ at 3302.2 m MD (126 ± 2 °C, 1 SE) are higher than present-day downhole temperatures of ~ 115 °C (Fig. 3). Clumped isotope temperatures are 30 °C below modern ambient borehole temperatures within the sheared calcareous siltstone-claystone units at 3309.8 m MD.

Clumped isotope temperatures were used to calculate $\delta^{18}\text{O}_{\text{water}}$, $\delta^{13}\text{C}_{\text{CO}_2}$, and $\delta^{13}\text{C}_{\text{CH}_4}$ values for fluids and gases that would have been in equilibrium with the calcite at the time of mineral growth; for samples that do not have clumped isotope measurements, these values were calculated using a modern borehole temperature of 115 °C.

The mean calculated $\delta^{18}\text{O}_{\text{paleowater}}$ compositions of the calcite veins are +3 ‰, which is in the range of $\delta^{18}\text{O}$ values reported for waters sampled from the SAFOD borehole (-4 ‰ to +7 ‰; Thordsen et al., 2010). The values for $\delta^{18}\text{O}_{\text{water}}$ increase as a function of increasing vein formation temperature with the exception of one calcareous clast sampled at 3307.9 m MD that had a calculated $\delta^{18}\text{O}_{\text{water}}$ of +4 ‰ and a relatively low clumped isotope temperature of 67 ± 4 °C (1 SE).

The calculated $\delta^{13}\text{C}_{\text{CO}_2}$ composition of CO_2 that would have been in equilibrium with the vein calcite has a mean value of -10 ± 8 ‰ (1σ), and is isotopically heavier at the sampled depths (3186 to 3309 m MD) than the mean $\delta^{13}\text{C}_{\text{CO}_2}$ value of -19 ± 4 ‰ (1σ) reported for SAFOD mudgas CO_2 (255 to 3903 m MD; Wiersberg and Erzinger, 2008). The calculated $\delta^{13}\text{C}_{\text{CO}_2}$ composition of CO_2 also is heavier than soil CO_2 along the SAFZ, which has a mean $\delta^{13}\text{C}_{\text{CO}_2}$ value of -2 ± 1 ‰ (1σ) (Lewicki et al., 2003). Calculated $\delta^{13}\text{C}_{\text{CO}_2}$ values are tightly clustered at

-14 ± 1 ‰ (1σ) from 3196.7 to 3198.0 m MD; however, an abrupt shift to a $\delta^{13}\text{C}_{\text{CO}_2}$ value of $+0.8$ ‰ occurs within the sheared silty shale units just below the CDZ at 3300.0 m MD. $\delta^{13}\text{C}_{\text{CO}_2}$ values become isotopically lighter with depth from 3198 m MD to 3309.8 m MD. The $\delta^{13}\text{C}_{\text{CO}_2}$ value is -17 ‰ within the calcareous siltstone and claystone units at 3309.8 m MD.

The carbon isotopic composition of methane that would have been in equilibrium with the calcite veins ($\delta^{13}\text{C}_{\text{CH}_4} -58 \pm 10$ ‰, 1σ) is about 17 ‰ lower than the mean value of the modern-day mudgas $\delta^{13}\text{C}_{\text{CH}_4} (-41 \pm 9$ ‰, 1σ) (Wiersberg and Erzinger, 2008).

5. Discussion

The following generalizations can be made regarding the results of the stable isotope data. First, there are systematic variations in the isotopic values as a function of lithology and with distance from the SDZ and CDZ. Whereas $\delta^{13}\text{C}$ values vary throughout the sampled interval, the greatest variation in $\delta^{18}\text{O}$ is generally restricted to the structural transition across the SDZ. Secondly, the clumped-isotope temperatures for some samples are similar to present-day downhole temperatures. A few veins in deformed gouge and rocks near the SDZ and CDZ have Δ_{47} temperatures that exceed modern borehole temperatures by 10 to 20 °C, while a few veins below the CDZ have Δ_{47} temperatures that are ~20 to 30 °C below modern ambient borehole temperatures. We use these data to constrain (1) the origin and temperature of fluids from which the veins precipitated, (2) the possible migration pathways of fluids within the SAFZ at seismogenic depths, and (3) implications for fault strength.

5.1 Constraints on the origin of fluids from carbon isotopes

The $\delta^{13}\text{C}$ values of carbonate veins sampled within the SAFOD borehole likely represent a mixture of several organic- and inorganic-derived carbon sources including biogenic and thermogenic CO_2 and/or CH_4 derived from (1) bicarbonate-bearing formation fluids in

sediments, (2) dissolution of calcareous shells or diagenetic calcite cements, (3) metamorphism of carbonates, (4) mantle degassing, and (5) organic matter. Here we evaluate these potential fluid sources by comparing the measured $\delta^{13}\text{C}$ values of carbonate veins and back-calculated equilibrium $\delta^{13}\text{C}$ values of CO_2 and CH_4 with modern borehole gas values, and compare the $\delta^{13}\text{C}$ values of carbonate veins to their sedimentary host rocks.

The calculated $\delta^{13}\text{C}_{\text{CO}_2}$ values for a subset of calcite veins are in equilibrium with modern-day mudgas CO_2 (Fig. 4a). The $\delta^{13}\text{C}_{\text{CO}_2}$ that would be in equilibrium with calcite veins sampled from the serpentinite-bearing fault gouge of the SDZ (3196.4 to 3198.1 m MD), sheared calcareous siltstone-claystone units (3307.4-3311.0 m MD), and the majority of vein material obtained from cuttings are in approximate carbon isotopic equilibrium with the modern-day mud gas ($-26 < \delta^{13}\text{C}_{\text{CO}_2} < -13$ ‰) that fall within the range of $\delta^{13}\text{C}$ values typical of CO_2 generated from the thermal breakdown of organic matter (-25 to -10 ‰) (Fig. 4a).

The carbon isotope trends observed just outside the SDZ and CDZ are consistent with a second fluid source that interacted with marine carbonates. Calcite veins sampled within the foliated sandstone-siltstone-shale cataclasites (3186.8-3194.0 m MD), serpentinite-bearing fault gouge (CDZ, 3297.1-3299.1 m MD), and sheared silty shale (3299.1-3301.5 m MD) have $\delta^{13}\text{C}$ values (Fig. 4a) that fall within the range of $\delta^{13}\text{C}$ values typical of marine carbonates ($-2 < \delta^{13}\text{C} < +2$ ‰; Wycherley et al., 1999). Calculated $\delta^{13}\text{C}_{\text{CO}_2}$ using our $T(\Delta_{47})$ data fall within the range of $\delta^{13}\text{C}_{\text{CO}_2}$ values predicted to be in carbon isotope equilibrium with limestone and marble host rocks sampled by Pili et al. (2011) from several localities along the SAFZ in the Parkfield area.

The carbon isotopic compositions of the veins from the black ultracataclasite (3194.0-3196.4 m MD), sheared siltstone and shale (3295.1 to 3296.3 m MD), and foliated sandstone-siltstone-shale (3303.3 to 3307.4 m MD) have values ($-12 < \delta^{13}\text{C}_{\text{CO}_2} < -2$ ‰) that (1) fall within

a range of values for CO₂ derived from mixing of two sources (e.g., thermal break of organic matter and limestone) or from regional metamorphism or mantle degassing source (Wycherley et al., 1999), and (2) are intermediate between the veins found within their adjacent units (Fig. 4a). Our T(Δ_{47}) are not consistent with the calcite veins having precipitated from fluids within the range of temperatures required for significant CO₂ generation from regional or contact metamorphism. This includes two samples from the sheared massive siltstone (3301.5-3303.3 m MD) that have clumped-isotope temperatures of 103 and 126 °C, close to the modern ambient borehole temperature of ~114 °C at those depths (Fig. 3). Thus, it is possible that the calculated $\delta^{13}\text{C}_{\text{CO}_2}$ values for this subset of veins are influenced by carbon-bearing fluids from the adjacent rock units.

The $\delta^{13}\text{C}$ values of a subset of veins sampled from the sheared siltstone and shale (3295.1 to 3296.3 m MD) and foliated sandstone-siltstone-shale (3303.3 to 3307.4 m MD) (Figs. 3 and 4a) could be controlled, in part, by the localized flux of mantle volatiles between the SDZ and CDZ reported by Wiersberg and Erzinger (2011). The equilibrium $\delta^{13}\text{C}_{\text{CO}_2}$ values of this subset of veins (Fig. 4a) fall within mantle $\delta^{13}\text{C}_{\text{CO}_2}$ values of -4 to -7 ‰ (Wycherley et al., 1999), but do not permit unequivocal interpretations of fluid provenance because bulk crustal and average mantle-derived $\delta^{13}\text{C}_{\text{CO}_2}$ values overlap (-3 to -8 ‰, VPDB). The $^3\text{He}/^4\text{He}$ values of fluids and veins may be more diagnostic. The $^3\text{He}/^4\text{He}$ values obtained from fluids (Kennedy et al., 1997) and veins (Pili et al., 2011) sampled from various locations along the SAFZ are consistent with a flux of mantle-derived fluids entering the SAF zone. The spatial distribution of measured $^3\text{He}/^4\text{He}$ ratios from SAFOD mud gas were interpreted by Wiersberg and Erzinger (2011) to represent (1) little to no flux of mantle volatiles within the Pacific Plate side of the SAF, (2) the presence of mantle-derived volatiles at small spatial scales between the SDZ and CDZ that were

limited by rock permeability, and (3) an elevated flux of mantle volatiles within the North American Plate side of the SAF. Our results are consistent with limited migration of mantle-derived fluids into the fault zone at the SAFOD locality, possibly along fracture networks on either side of the CDZ. However, the systematic shift from low to high $\delta^{13}\text{C}$ values can also be explained by increasing contributions of carbon derived from marine carbonate in the damage zones adjacent to the low permeability SDZ and CDZ.

The calculated $\delta^{13}\text{C}_{\text{CH}_4}$ values show that none of the calcite veins formed in carbon-isotope equilibrium with the methane encountered in the drill hole at the sample depths (Fig. 4b). If methane was involved in the formation of the veins, then either (1) the veins formed at shallower depths where biogenic methane was once more prevalent, or (2) the $\delta^{13}\text{C}$ of the methane has been altered since the veins formed.

The measured $T(\Delta_{47})$ and calculated $\delta^{13}\text{C}_{\text{CH}_4}$ values may support the hypothesis that at least some of the calcite veins precipitated from fluids at depths where biogenic or mixed biogenic/thermogenic gases are prevalent from 2 to 2.5 km MD (Fig. 4b). This hypothesis has been suggested by the results from previous basin modeling (d'Alessio and Williams, 2007) and stable isotope studies (Wiersberg and Erzinger, 2008; 2011). Integrated (U/-Th)/He and fission track age and length modeling indicate that the SAFOD site has experienced <1 km of burial and subsequent unroofing since SAF initiation (d'Alessio and Williams, 2007). Based on this estimate of d'Alessio and Williams (2007) and a constant modern-day geothermal gradient (Blythe et al., 2004), it is unlikely that the rocks encountered within the SAFOD borehole have experienced temperatures outside the range of approximately 80 to 150 °C since the onset of faulting. Wiersberg and Erzinger (2008) showed that the SAFOD mud gas hydrocarbons above 2500 m MD have carbon and hydrogen compositions consistent with a significant microbial

component. Calcite veins precipitating from fluids at these depths should preserve a $T(\Delta_{47})$ of less than 70 °C. Only one sample of a carbonaceous clast at 3307.9 m MD records a crystallization temperature low enough to have formed at depths where biogenically derived gases are present (Fig. 3).

The calculated $\delta^{13}\text{C}_{\text{CH}_4}$ values are not consistent with the hypothesis that the veins formed in carbon isotopic equilibrium with modern thermogenic gases (Fig. 4c); however, the measured $T(\Delta_{47})$ for the veins are consistent with formation at depths where thermogenic gases are prevalent. Wiersberg and Erzinger (2011) attribute the observed mud gas $\text{CO}_2\text{-CH}_4$ carbon isotope disequilibrium to preferential removal of light carbon molecules due to diffusive gas loss from the reservoir units. Thus, the veins could have formed in equilibrium with gases prior to post-formation migration when the $\delta^{13}\text{C}$ values of the methane would have been significantly lower. These findings are consistent with the $\delta^{13}\text{C}$ variations in the SAFOD calcite veins not having been influenced significantly by the presence of methane.

The carbon isotope data are consistent with a relatively open-flow system through interconnected fracture networks rather than pervasive or porous flow within portions of the damage zone proximal to the actively-deforming fault strands (Fig. 3). Only the vein samples hosted within the SDZ and CDZ have carbon isotopic values similar to their host rocks (Fig. 3) consistent with closed-system fluid flow regime.

5.2 Constraints on fluid pathways and fluid-rock interaction from oxygen isotopes

The oxygen isotope compositions of the carbonate veins encountered within the SAFOD borehole are likely controlled by several factors including the parent fluid isotopic composition (meteoric water versus basin brines), fluid temperatures, fluid-rock interactions, and water-to-rock ratios. Here we compare our calculated $\delta^{18}\text{O}_{\text{paleowater}}$ values to values of the modern SAFOD

borehole fluids and nearby well and spring waters in order to determine possible fluid sources, migration pathways, and the extent of fluid-rock interaction within the SAFOD borehole.

The $\delta^{18}\text{O}_{\text{paleofluid}}$ values are consistent with vein precipitation from meteoric fluids advected to sampled depths on the southwest side of the SDZ, and with evolved meteoric/basin brine fluids on the northeast side of the SDZ. The $\delta^{18}\text{O}$ values of well waters (Fig. 4d) measured at ~3 km depth (Thordsen et al., 2005) are enriched in ^{18}O by approximately 1.2 ‰ compared to the most ^{18}O -rich local shallow groundwater (Thompson and White, 1991). These observations are consistent with the advection of shallow groundwater to at least 3 km depth possibly along permeable fracture networks through the damage zone of the SAF. The $\delta^{18}\text{O}_{\text{paleofluid}}$ values in equilibrium with calcite veins at modern-day borehole temperatures from the foliated sandstone-siltstone-shale cataclasites located on the southwest side of the SDZ range from -4 to +1 ‰ (Fig. 4d). These $\delta^{18}\text{O}_{\text{paleofluid}}$ values are similar to the $\delta^{18}\text{O}$ of modern SAFOD borehole fluids (Thordsen et al., 2005) and waters sampled from the Jack-Ranch Highway 46 well (Kennedy et al., 1997) located in close proximity to the SAF approximately 30 km south of the SAFOD study area (Fig. 4d). The observed oxygen isotope disequilibrium between the calcite veins and host rocks ($\Delta^{18}\text{O}_{\text{vein-host rock}} \sim 10$ ‰) above the SDZ is consistent with the infiltration of meteoric fluids to these depths (Fig. 3). The $\delta^{18}\text{O}$ values of well water encountered deeper within the borehole at 3608 m MD on the northeast side of the actively-deforming zones were interpreted by Thordsen et al. (2010) to be consistent with rock-buffered formational fluids at intermediate depths and temperatures (Fig. 4e). The Middle Mountain Oil seep and Varian-Phillips wells are within 1.5 km east of the SAF near Parkfield and have high $\delta^{18}\text{O}$ values of +5.6 and +5.9 ‰ (Fig. 4e), respectively (Thompson and White, 1991). The $\delta^{18}\text{O}_{\text{paleofluid}}$ values (Fig. 4e) for veins sampled below the foliated sandstone-siltstone-shale cataclasites (3194.0 m MD) follow a trend

toward $\delta^{18}\text{O}$ values similar to the evolved meteoric waters or oil field brines sampled on the northeast side of the SAF.

The difference in the observed $\delta^{18}\text{O}$ values of waters on either side of the actively-deforming zones is consistent with the SAFZ acting as a baffle to cross-fault fluid flow (Fig. 4d,e). The $\delta^{18}\text{O}_{\text{water}}$ values calculated using $T(\Delta_{47})$ and modern borehole temperatures for the veins sampled from 3194.0 to 3309.9 m MD are intermediate between modern day $\delta^{18}\text{O}_{\text{water}}$ values sampled on either side of the fault zone. We interpret these intermediate values to represent episodic mixing between meteoric fluids and basin brines within open fracture networks possibly during episodes of fracture opening associated with motion on the fault. Our interpretation is consistent with the results of Mittempergher et al. (2011), who interpreted alternating luminescent bands and crack-seal growth textures to represent changing fluid conditions after fracture development. Additionally, Holdsworth et al. (2011) observed that veins within the active fault gouges occur primarily within clasts of various lithologies in contrast to the presence of relatively continuous veins found within the inactive sections of the fault zone. This observation is consistent with vein formation within the active sections of the SAF predating aseismic creep, and possibly providing a record of deformation episodes characterized by fracture-network facilitated fluid flow within the impermeable fault core.

The calculated calcite vein $\delta^{18}\text{O}_{\text{paleowater}}$ values, variable $T(\Delta_{47})$ values, and the observed oxygen isotope equilibrium between calcite veins and host rock are consistent with calcite vein precipitation from pore fluids that have undergone varying degrees of oxygen isotope exchange with the host rocks over a range of temperatures (Fig. 4f). An original pore fluid having a meteoric oxygen isotope composition would have likely undergone some degree of isotopic exchange with the host rocks enriching the pore fluids in heavy oxygen. The $\delta^{18}\text{O}_{\text{paleowater}}$ values

calculated for the calcite veins and cuttings sampled from 3194.0 to 3309.9 m MD fall within the range of values predicted for water-mineral equilibrium fractionation curves representing the predominant mineralogy of the Great Valley sequence host rocks (Fig. 4f) including quartz, serpentinite, and illite-smectite (Barnes et al., 2013; Suchecky and Land, 1983). These observations are consistent with closed-system fluid flow conditions below 3194.0 m MD.

The changes in $\delta^{18}\text{O}$ of the carbonate cements and the back-calculated fluids can be used to model the isotopic evolution of the fluid-rock system (Fig. 5) using the method outlined in Banner and Hansen (1990). We modeled heating from 0 to 140 °C using the average $\delta^{18}\text{O}$ value of the six host rock samples (+21 ‰, VSMOW) and $\delta^{18}\text{O}$ of water equal to the average of the shallow spring and well waters near Parkfield (-7 ‰, Thompson and White, 1999).

The open system model (Fig. 5) tracks the evolution of the fluid-rock system as repeated additions of unreacted fluid (i.e., with constant oxygen isotopic composition) displace the existing pore fluids. The $\delta^{18}\text{O}$ values of the precipitating carbonates evolve toward the fluid $\delta^{18}\text{O}$ composition as temperatures increase (Δ_{47} decreases). The open-system heating model predicts a 10 ‰ shift in carbonate $\delta^{18}\text{O}$ values over the temperature range indicated by the $T(\Delta_{47})$ results spanning from 67 to 134 °C. Our dataset does not follow the pattern predicted by the open-system model.

Instead, our data set is well described by a closed-system (rock-buffered) heating model for water-rock ratios less than ~0.25 wt %. The $\delta^{18}\text{O}$ values of the majority of the carbonate cements are consistent with very low water-rock ratios (< 0.1 weight %), supporting the interpretation that the veins formed in a rock-buffered system. This result is also consistent with our interpretation of the modern waters sampled by previous workers within the SAFOD well. Fluids sampled at approximately 3065 m MD by Thordsen et al. (2005) fall between the 0.5 and

1.0 weight % water-to-rock ratio contour consistent with rapid downward migration of meteoric fluids with limited fluid-rock interaction on the west side of the fault. The $\delta^{18}\text{O}$ values of deeper formation fluids sampled at about 3608 m MD fall below the 0.01 weight % water-to-rock contour consistent with rock-buffered formation fluids.

6. Model of vein formation

The veins analyzed in this study were sampled throughout the damage zone and along the contacts of the actively-deforming serpentinite-bearing units. The spatial distribution of vein isotopic compositions appears to be controlled primarily by lithology, which exerts primary control on fluid chemistry in a closed fluid system. The isotopic compositions of the veins near the lithologic contacts and actively-deforming zones have values of $\delta^{13}\text{C}$ and $\delta^{18}\text{O}$ intermediate between the two adjacent units, consistent with these contact surfaces acting as local fluid conduits possibly accommodating some displacement. We propose that the veins formed in compartments where fluids become isolated and follow different isotopic evolution paths controlled by the local mineralogy and carbon sources. Our observations are consistent with microstructural studies of the calcite veins within meters of the actively-deforming portions of the SAF by Mittempergher et al. (2011) and Hadizadeh et al. (2012), which clearly show evidence of locally high fluid pressures interpreted to have formed in compartments isolated from each other by zones of insoluble material formed from stress driven pressure solution (Gratier et al., 2009; Schleicher et al., 2009; Mittempergher et al., 2011). In light of these observations, we interpret the isotopic data to be consistent with limited, episodic, and heterogeneously distributed fluid flow within the SDZ and CDZ, and relatively open-flow conditions within the damage zones proximal to the low-permeability deforming zones that may

serve as a permeable pathway through the upper crust for meteoric fluids to reach seismogenic depths.

7. Implications for fault strength

7.1 Fluid pressure

Several models have been proposed for the development of high pore fluid pressures (and low effective normal stress) that could explain the slip on the SAF under very low shear stresses (Zoback et al., 1987), and the associated lack of an observable heat anomaly near the fault (Lachenbruch, 1980). A model of episodic flow and sealing involves a cyclical process in which fluids from the host rocks saturate the fault zone, high fluid pressure compartments form as fractures become mineralized, earthquakes are triggered by ruptures between high- and low-pressure seals, and fluids are expelled during shearing (Byerlee, 1993). A channelized, continuous flow model envisions fluid flow up a low, but pressure-dependent permeable fault zone in which fluids are sourced from depth, possibly from the mantle (Rice, 1992). An alternative model that involves flow of fluids from deep sources is the fault-valve model of Sibson (1990) in which elevated fluid pressure develops below a locked, impermeable fault until seismic slip ruptures the fault seal and pressurized fluids are released.

Our results are not consistent with the channelized, continuous flow model or the fault-valve model. Morrow et al. (2014) found that the gouge in the actively deforming zones has ultra-low permeability and concluded that fluid-flow occurs in the highly fractured bounding rocks. Carbon and oxygen isotope disequilibrium between veins in the foliated and sheared siltstones and shales above the SDZ are consistent with a meteoric water-dominated open-flow system on the southwest side of the actively-deforming zones. Oxygen equilibrium between calcite veins and host rocks associated with the actively-deforming strands are consistent with

closed-system behavior, and the results of Morrow et al. (2014). Additionally, the carbon isotopic composition of the veins is not consistent with continuous or episodic replenishment of fluids into the fault zone from the upper mantle. This interpretation is supported by results from magnetotelluric data obtained by Becken et al. (2008), who show that the SAF does not currently act as a major fluid pathway through the entire crust. Flow through a low-permeability fault zone would allow for the fluids to thermally equilibrate with the surrounding host rocks; thus, clumped-isotope temperatures would not likely provide a record of a heat-flow anomaly unless fluids were migrating rapidly upward from greater depths.

The model of episodic flow and sealing (Byerlee, 1993) is compatible with our stable isotope data wherein fluids flow into the fault, fault-sealing processes compartmentalize the fluid zones through mineralization, pressure solution, and compaction of fault gouges, and locally high-pressures could develop under fault-normal compression. Recent experiments, however, show that the clay-rich gouge of the SDZ and CDZ have extremely low coefficients of sliding friction and that elevated pore fluids are not necessary to explain the low strength and creep behavior (Lockner et al., 2011; Carpenter et al., 2011, 2012; Coble et al., 2014; French et al., 2015).

7.2 Fluid-rock interactions

Wintsch et al. (1995) modeled the interaction of meteoric waters with rocks having granitic compositions in both water- and rock-dominated environments at zeolite to lower-greenschist-facies conditions, which are appropriate for the SAF at SAFOD. The infiltration of meteoric water into the fault zone is expected to shift the composition of the pore water away from equilibrium established between the existing fault fluids and mineral assemblages. Given these conditions, the solid-fluid equilibria models of Wintsch et al. (1995) predict the formation

of illite and smectite (I-S) in meteoric water-dominated systems by way of replacement reactions with feldspar, and the replacement of phyllosilicates by feldspars in a rock-dominated system. Wintsch et al. (1995) predicts the production of phyllosilicates, especially chlorite and smectite (C-S), in both water- and rock-dominated environments provided the chemical activity of magnesium is high enough. In light of the fluid-mineral equilibria models of Wintsch et al. (1995), we suggest that there is (1) a short-lived water-dominated chemical environment that favors the generation of I-S phyllosilicates along newly formed fracture and mineral surfaces (Fig 6 a and b), followed by (2) a period of rock-dominated fluid-rock interaction as fluids become more compartmentalized in the fault zone because of precipitation of feldspar or C-S phyllosilicates in fractures and pores (Fig 6c).

Our interpretation is supported by Schleicher et al. (2010) who utilized electron microscopy and x-ray diffraction to identify phyllosilicate phases within the SAFOD borehole. Schleicher et al. (2010) observed the preferential formation of thin (<100 nm thick) coatings of both I-S and C-S on fracture surfaces and grain boundaries. They proposed a three-step model of fault zone evolution wherein (1) fluids are introduced into the fault zone along fracture networks after displacement, (2) phyllosilicates precipitate along fracture surfaces and grain boundaries via mineral replacement reactions, and (3) clay-coated fracture networks coalesce, eventually leading to the onset of creep. Macroscopically, Moore and Rymer (2012) and Bradbury et al. (2015) document the presence of smectitic clays saponite and palygorskite in the foliated clay gouge from the CDZ and SDZ. The illite-smectite mineral assemblages observed near the SDZ and CDZ are more smectite-rich than kinetic models predict for typical prograde burial sequences (Schleicher et al. 2009). The increased smectite content could be a result of the influx of cool fluids or fluids with K^+ concentrations lower than typical sedimentary brines (Schleicher

et al., 2009), consistent with our model of vein formation that predicts the advection of meteoric fluids along permeable fracture networks within the damage zone of the SAF.

8. Summary

Clumped-isotope thermometry of calcite veins within the SAFOD borehole provides a record of paleo-fluid flow within the fault zone. The C and O-isotope compositions vary systematically as a function of distance from the SDZ and CDZ. Fracture networks located adjacent to the SDZ and CDZ served as conduits for advecting meteoric fluids to seismogenic depths. The advecting meteoric fluids likely contained inorganic carbon derived from interaction with marine carbonates. A meteoric water-dominated environment would favor the formation of the low-strength phyllosilicate fault rocks. The difference in the calculated $\delta^{18}\text{O}_{\text{paleofluids}}$ ($\Delta\delta^{18}\text{O} \sim 14 \text{‰}$) from which the vein cements grew on either side of the fault zone is consistent with the SDZ and CDZ acting as low-permeability cross-fault fluid-flow barriers. The oxygen isotopic composition of fluids within these two actively deforming zones was controlled by fluid interactions with the surrounding host rocks. Locally, the fluid within the SDZ and CDZ contained organically derived carbon released from the thermal breakdown of organic matter during burial. Clumped-isotope temperatures provide evidence that calcite vein growth occurred over a wide range of temperatures that bound modern-day ambient borehole temperatures. The hydrogeologic system can be envisioned as a network of short-lived conduits that open episodically during deformation and transport fluids from the surrounding host rocks into the fault zone. These conduits are then sealed by mineralization and compartmentalize the fault zone, possibly allowing for the development of locally high fluid pressures, and subsequent fracture formation and slip in otherwise unfavorable stress conditions.

Acknowledgements

We thank Stephen Hickman, Mark Zoback, and Bill Ellsworth for bringing the SAFOD project to fruition. We also thank Jim Thordsen, Yousef Kharaka, and Thomas Wiersberg for their input and willingness to share their as yet unpublished water and gas chemistry data during the early phases of this study. We also thank the SAFOD student crew for their help and support in collecting some of the cuttings that were used in this study. A special thanks to Andrew Schauer and Kyle Samek for their time and patience while training PBL at the IsoLab, UW-Seattle. Finally, we thank Olivier Fabbri and an anonymous reviewer for their constructive comments that significantly improved this manuscript.

The authors acknowledge financial support for this study to P. B. Luetkemeyer from a Geological Society of America graduate student research grant and Grant-in-Aid of Research from the American Association of Petroleum Geologists, to D. Kirschner from the National Science Foundation (EAR-0643223), to J. Chester and F. Chester from the National Science Foundation (EAR-0643339), to J. Evans from the National Science Foundation (EAR-0643027, EAR-0454527), and to K. W. Huntington from the National Science Foundation (EAR-1156134).

Appendix A. Supplementary Figures

Supplementary data associated with this article can be found in the online version. These data include images of the Phase 3 core with sample locations and results from conventional stable isotope analyses and clumped-isotope thermometry.

References

Affek, H.P., Eiler, J.M., 2006. Abundance of mass 47 CO₂ in urban air, car exhaust, and human breath. *Geochem. Cosmochim. Acta* 70, 1-12.

- Banner, J.L., Hanson, G.N., 1990. Calculation of simultaneous isotopic and trace element variations during water-rock interaction with applications to carbonate diagenesis: *Geochim. Cosmochim. Acta* 54, 3123-3137.
- Barnes, J.D., Eldman, R., Lee, C-T. A., Errico, J.C., Loewy, S., Cisneros, M., 2013. Petrogenesis of serpentinites from the Franciscan Complex, western California, USA. *Lithos* 178, 143-157.
- Beaudoin, N., Bellahsen, N., Lacombe, O., Emmanuel, L., 2011. Fracture-controlled paleohydrology in a basement-cored, fault-related fold: Sheep Mountain Anticline, Wyoming, United States. *Geochem. Geophys. Geosys.* 12, Q06011.
- Becken, M., Ritter, O., Park, S.K., Bedrosian, P.A., Weckmann, U., Weber, M., 2008. A deep crustal fluid channel into the San Andreas Fault system near Parkfield, California. *Geophys. J. Int.* 173, 718-732.
- Bergman, S.C., Huntington, K.W., Crider, J., 2013. Tracing paleofluid sources using clumped isotope thermometry of diagenetic cements along the Moab Fault, Utah. *Am. J. Sci.* 315, 490-515.
- Boles, J.R., Eichhubl, P., Graven, G., Chen, J., 2004. Evolution of a hydrocarbon pathway along basin-bounding faults: Evidence from fault cement. *AAPG Bull.* 88, 947-970.
- Bottinga, Y., 1968. Calculation of fractionation factors for carbon and oxygen isotopic exchange in the system calcite-carbon dioxide-water. *J. Phys. Chem.* 72, 800-808.
- Bottinga, Y., 1969. Calculated fractionation factors for carbon and hydrogen isotope exchange in the system calcite-carbon dioxide-graphite-methane-hydrogen-water vapor. *Geochim. Cosmochim. Acta* 33, 49-64.

- Bradbury, K.K., Barton, D.C., Solum, J.G., Draper, S.D., Evans, J.P., 2007. Mineralogic and textural analysis of drill cuttings from the San Andreas Fault Observatory at Depth (SAFOD) boreholes: Initial interpretations of fault zone composition and constraints on geologic models. *Geosphere* 7, 299-318.
- Bradbury, K.K., Evans, J.P., Chester, J.S., Chester, F.M., Kirschner, D.L., 2011. Lithology and internal structure of the San Andreas fault at depth based on characterization of Phase 3 whole-rock core in the San Andreas Fault Observatory at Depth (SAFOD) borehole. *Earth Planet. Sci. Lett.* 310, 131-144.
- Bradbury, K. K., Davis, C., Shervais, J. W., Janecke, S. U., and Evans, J. P., 2015, Composition, alteration, and texture of fault-related rocks from SAFOD core and surface analogs: Evidence for deformation processes and fluid-rock interactions, *Pure Appl. Geophys.* 172,1053-1078, doi:10.1007/s00024-014-0896-6.
- Budd, D.A., Frost, E.L., Huntington, K.W., Allwardt, P.F., 2013. Syndepositional deformation features in high-relief carbonate platforms: long-lived conduits for diagenetic fluids. *J. Sediment. Res.* 83, 12–36. doi: 10.2110/jsr.2013.3.
- Byerlee, J., 1990. Friction, overpressure, and fault normal compression. *Geophys. Res. Lett.*, 17, 2109-2122.
- Byerlee, J., 1993. Model for episodic flow of high-pressure water in fault zones before earthquakes. *Geology*, 21, 303-306.
- Blythe, A.E., d'Alessio, M.A., Bürgmann, R., 2004. Constraining the exhumation and burial history of the SAFOD pilot hole with apatite fission track and (U-Th)/He thermochronology. *Geophys. Res. Lett.* 31, L15S16.

- Campbell, K.A., Farmer, J.D., Marais, D.D., 2002. Ancient hydrocarbon seeps from the Mesozoic convergent margin of California: carbonate geochemistry, fluids and paleoenvironments. *Geofluids* 2, 63-94.
- Carpenter, B., Marone, C., and Saffer, D., 2011. Weakness of the San Andreas Fault revealed by samples from the active fault zone, *Nat. Geosci.*, 4, 251–254, doi:10.1038/ngeo1089.
- Carpenter, B. M., Saffer, D. M., Marone, C., 2012. Frictional properties and sliding stability of the San Andreas Fault from deep drill core, *Geology*, 40, 759–762, doi:10.1130/G33007.1.
- Coble, C. G., French, M. E., Chester, F. M., Chester, J. S., Kitajima, H., 2014. Frictional Strength of the Creeping Section of the San Andreas Fault at SAFOD, *Geophys. J. Int.* 199, 956-967, doi:10.1093/gji/ggu306.
- d'Alession, M.A., Williams, C.F., 2007. Putting it all together: Exhumation histories from a formal combination of heat flow and a suite of thermochronometers. *J. Geophys. Res.* 112, B08412.
- Davissou, M.L., Presser, T.S., Criss, R.E., 1994. Geochemistry of tectonically expelled fluids from the northern Coast ranges, Rumsey Hills, California, USA. *Geochim. Cosmochim. Acta* 58, 1687-1699.
- Dennis, K.J., Affek, H.P., Passey, B.H., Schrag, D.P., Eiler, J.M., 2011. Defining an absolute reference frame for 'clumped' isotope studies of CO₂. *Geochim. Cosmochim. Acta* 75, 7117-7131.
- Eiler, J.M., 2007. "Clumped-isotope" geochemistry - The study of naturally-occurring, multiply-substituted isotopologues. *Earth Plane. Sci. Lett.* 262, 309-327.
- Eiler, J.M., 2011. Paleoclimate reconstruction using carbonate clumped isotope thermometry. *Quat. Sci. Rev.* 30, 3575–3588.

- Eiler, J.M., 2013. The isotopic Anatomies of Molecules and Minerals. *Annu Rev Earth Pl Sc.* 41, 411-441.
- Eiler, J.M., Bergquist, B., Bourg, I., Cartigny, P., Farquhar, J., Gagnon, A., Guo, W., Halevy, I., Hofmann, A., Larson, T.E., Levin, N., Schauble, E.A., Stolper, D., 2014. Frontiers of stable isotope geoscience. *Chem. Geol.* 372, 119-143.
- Erzinger, J., Wiersberg, T., Dahms, E., 2004. Real-time mud gas logging during drilling of the SAFOD Pilot Hole in Parkfield, CA. *Geophys. Res. Lett.* 31, L13S18.
- Evans, J.P., Chester, F.M., 1995. Fluid interactions in faults of the San Andreas system: Inferences from San Gabriel fault rock geochemistry and microstructures. *J. Geophys. Res.* 100, 13007-13020.
- Evans, M.A., Bebout, G.E., Brown, C.H., 2012. Changing fluid conditions during folding: An example from the central Appalachians. *Tectonophysics* 576-577, 99-115.
- French, M. E., Chester, F. M., Chester, J. S., 2015. Micro-mechanisms of creep in clay-rich gouge from the Central Deforming Zone of the San Andreas Fault, *J. Geophys. Res. Solid Earth* 120, 827–849, doi: 10.1002/2014JB011496.
- Fulton, P.M., Saffer, D.M., Harris, R.N., Bekins, B.A., 2004. Re-evaluation of heat flow data near Parkfield, CA: Evidence for a weak San Andreas Fault. *Geophys. Res. Lett.* 31, L15S15.
- Fulton, P.M., Saffer, D.M., 2008. Potential role of mantle-derived fluids in weakening the San Andreas Fault. *J. Geophys. Res.* 114, B07408.
- Ghosh, P., Adkins, J., Affek, H., Balta, B., Guo, W., Schauble, E.A., Schrag, D., Eiler, J.M., 2006. ^{13}C - ^{18}O bonds in carbonate minerals: A new kind of paleothermometer. *Geochim. Cosmochim. Acta* 70, 1439-1456.

- Gratier, J.-P., Richard, J., Mittempergher, S., Renard, F., Doan, M., Di Toro, G., Hadizadeh, J., Bertrand, A.M.B., 2009. Pressure solution as a mechanism for creep and sealing in active faults, evidence from the SAFOD samples. *Eos Trans. AGU*, 90(52), Fall Meet. Suppl. Abstract T21B-1800.
- Gratier, J.-P., Richard, J., Renard, F., Mittempergher, S., Doan, M.-L., Di Toro, G., Hadizadeh, J., Boullier, A.-M., 2011. Aseismic sliding of active faults by pressure solution creep: Evidence from the San Andreas Fault Observatory at Depth. *Geology* 39, 1131-1134.
- Hadizadeh, J., Mittempergher, S., Gratier, J.-P., Renard, F., Di Toro, G., Richard, J., Babaie, H.A., 2012. A microstructural study of fault rocks from the SAFOD: Implications for the deformation mechanisms and strength of the creeping segment of the San Andreas Fault. *J. Struct. Geol.* 42, 246-260.
- Hayes, M.J., Boles, J., 1993. Evidence for meteoric recharge in the San Joaquin basin, California provided by isotope and trace element chemistry of calcite. *Mar. and Petrol. Geol.* 10, 135-144.
- Hardebeck, J.L., Hauksson, E., 1999. Role of fluids in faulting inferred from stress field signatures. *Science* 286, 236-239.
- He, B., Olack, G.A., Colman, A.S., 2012. Pressure baseline correction and high-precision CO₂ clumped-isotope (Δ_{47}) measurements in bellows and micro-volume modes. *Rapid Comm. Mass Spec.* 26, 2837-2853.
- Hickman, S.H., Zoback, M.D., 2004. Stress orientations and magnitudes in the SAFOD pilot hole. *Geophys. Res. Lett.* 31, L15S12.

- Holdsworth, R.E., van Diggelen, E.W.E., Spiers, C.J., de Bresser, J.H.P., Walker, R.J., Bowe, L., 2011. Fault rocks from the SAFOD core samples: Implications for weakening at shallow depths along the San Andreas Fault, California. *J. Struct. Geol.* 33, 132-144.
- Hodson, K.R., Crider, J.G., Huntington, K.W., in revision. Multi-stage cementation and paleo fluid temperature in a faulted sandstone reservoir, Moab Fault, Utah, USA. *Tectonophysics* (this volume).
- Huntington, K.W., Eiler, J.M., Affek, H.P., Guo, W., Boniface, M., Yeung, L.Y., Thiagarajan, N., Passey, B., Tripathi, A., Daeron, M., Came, R., 2009. Methods and limitations of 'clumped' isotope (Δ_{47}) analysis by gas-source isotope ratio mass spectrometry. *J. Mass Spec.* 44, 1318-1329.
- Huntington, K.W., Lechler, A.R., 2015. Carbonate clumped isotope thermometry in continental tectonics. *Tectonophysics* 647-648, 1-20.
- Imber, J., Holdsworth, R.E., Smith, S.A., Jefferies, S.P., Collettini, C., 2008. Frictional-viscous flow, seismicity and the geology of weak faults: a review and future directions. In: Wibberly, C.A., Kurz, W., Imber, J., Holdsworth, R.E., Collettini, C., (Eds.), *The internal structure of fault zones: Implications for mechanical and fluid-flow properties*. *The Geo. Soc. Lond.* 299, 151-173.
- Johnson, P.A., Mc Evilly, T.V., 1995. Parkfield seismicity: fluid driven? *J. Geophys. Res.*, 100, B7, 12937-12950.
- Kawabe, I., 1978. Calculation of oxygen-isotope fractionation in quartz-water system with special reference to the low temperature fractionation. *Geochim. Cosmochim. Acta* 42, 613-621.

- Kennedy, B.M., Kharaka, Y.K., Evans, W.C., Ellwood, A., DePaolo, D.J., Thordsen, J., Ambats, G., Mariner, R.H., 1997. Mantle fluids in the San Andreas Fault System, California. *Science* 278, 1278-1280.
- Kharaka, Y.K., Berry, A.F., 1973. Isotopic composition of oil-field brines from Kettleman North Dome, California, and their geologic implications. *Geochim. Cosmochim. Acta* 37, 1899-1908.
- Kharaka, Y.K., Thordsen, J.J., Evans, W., 1999. Geochemistry and hydromechanical interactions of fluids associated with the San Andreas Fault system, California. *Am. Geophys. Union, Geophysical Monograph* 113, 129-148.
- Kirby, S.H., Wang, K., Brocher, T.M., 2014. A large mantle water source for the northern San Andreas fault system: a ghost of subduction past. *Earth, Planets, and Space* 66, 1-18.
- Kirschner, D.L., Masson, H., Sharp, Z.D., 1999. Fluid migration through thrust faults in the Helvetic nappes (Western Swiss Alps). *Contrib. Mineral. Petrol.*, 136, 169-183.
- Kirschner, D.L., Kennedy, L.A., 2001. Limited syntectonic fluid flow in carbonate-hosted thrust faults of the Front Ranges, Canadian Rockies, inferred from stable isotope data and structures. *J. Geophys. Res.* 106, B6, 8827-8840.
- Kluge, T., John, C.M., Jourdan, A-L., Davis, S., Crawshaw, J., 2015. Laboratory calibration of the calcium carbonate thermometer in the 25-250 °C temperature range. *Geochim. Cosmochim. Acta* 157, 213-227.
- Lachenbruch A.H., Sass, J.H., 1980. Heat flow energetics of the San Andreas Fault Zone. *J. Geophys. Res.* 85, 6185-6222.

- Laubach, S.E., Diaz-Tushman, K., 2009. Laurentian paleostress trajectories and ephemeral fracture permeability, Cambrian Eriboll Formation sandstones west of the Moine Thrust Zone, NW Scotland. *J. Geol. Soc.* 166, 349-362.
- Lewicki, J.L., Evans, W.C., Hilley, G.E., Sorey, M.L., Rogie, J.D., Brantley, S.L., 2003. Shallow soil CO₂ flow along the San Andreas and Calaveras Faults, California.
- Lockner, D. A., Morrow, C., Moore, D., Hickman, S., 2011. Low strength of deep San Andreas fault gouge from SAFOD core. *Nature*. doi:10.1038/nature09927.
- Loyd, S.J., Dickson, J.A.D., Scholle, P.A., Tripathi, A.K., 2013. Extensive, uplift-related and non-fault-controlled spar precipitation in the Permian Capitan Formation. *Sedimentary Geol.* 298, 17-27, doi: 10.1016/j.sedgeo.2013.10.001.
- Margaritz, M., Taylor, H.P., 1976. Oxygen, hydrogen, and carbon isotope studies of the Franciscan formation, Coast Ranges, California. *Geochim. Cosmochim. Acta* 40, 215-234.
- Marrett, R., Laubach, S.E., 1997. Diagenetic controls on fracture permeability and sealing. *Int. J. Rock Mech. & Min. Sci.* 34, 3-4, Paper No. 204.
- Mittempergher, S., Di Toro, G., Gratier, J.P., Hadizadeh, J., Smith, S.A.F., Spiess, R., 2011. Evidence of transient increases of fluid pressure in SAFOD phase III cores. *Geophys. Res. Lett.* 38, L03301.
- Moore, D.E. and Rymer, M.J., 2007. Talc-bearing serpentinite and the creeping section of the San Andreas fault. *Nature*, 448, 795-797.
- Moore, D.E., and Rymer, M.J. (2012), Correlation of clayey gouge in a surface exposure of serpentinite in the San Andreas Fault with gouge from the San Andreas Fault Observatory at Depth (SAFOD). *J. Struct. Geol.*, 38, 51-60, doi:10.1016/j.jsg.2011.11.014.

- Morrow, C.A., Lockner, D.A., Moore, D.E., Hickman, S., 2014. Deep permeability of the San Andreas Fault from San Andreas Fault Observatory at Depth (SAFOD) core samples. *J. Struct. Geol.* 64, 99-114.
- Noda, H., Dunham, E.M., Rice, J.R., 2009. Earthquake ruptures with thermal weakening and the operation of major faults at low overall stress levels. *J. Geophys. Res.* 114, B07302.
- O'Neil, J.R., Clayton, R.N., Mayeda, T.K., 1969. Oxygen isotope fractionation in divalent metal carbonates. *J. Chem. Phys.* 51, 5547-5558.
- Pili, É, Poitrasson, F., Gratier, J-P., 2002. Carbon-oxygen isotope and trace element constraints on how fluids percolate faulted limestones from the San Andreas Faults system: partitioning of fluid sources and pathways. *Chem. Geol.* 190, 231-250.
- Pili, É, Kennedy, B.M., Conrad, M.E., Gratier, J.-P., 2011. Isotopic evidence for the infiltration of mantle and metamorphic CO₂-H₂O fluids from below in faulted rocks from the San Andreas Fault system. *Chem. Geol.* 281, 242-252.
- Rice, J.R., 1992. Fault stress states, pore pressure distributions, and the weakness of the San Andreas fault, in Evans, B., and Wong, T.F., eds., *Earthquake mechanics and transport properties of rocks*: London, Academic Press, 475-503.
- Richard, J., Gratier, J-P., Doan, M-L., Boullier, A-M., Renard, F., 2014. Rock and mineral transformations in a fault zone leading to permanent creep: Interactions between brittle and viscous mechanisms in the San Andreas Fault. *J. Geophys. Res.* 119, 8132-8153.
- Rutter, E. H. 1976. The kinetics of rock deformation by pressure solution. *Phil. Trans. R. Soc. Lond.* 1976;A283:203-219.

- Rybacki, E., Janssen, C., Wirth, R., Chen, K., Wenk, H.-R., Stromeyer, D., Dresen, G., 2011. Low-temperature deformation in calcite veins of SAFOD core samples (San Andreas Fault) - Microstructural analysis and implications for fault rheology. *Tectonophysics* 509, 107-119.
- Sadofsky, S.J., Bebout, G.E., 2004. Field and isotopic evidence for fluid mobility in the Franciscan Complex: forearc paleohydrology to depths of 30 kilometers. *Int. Geol. Rev.* 46, 1053-1088.
- Schauble, E.A., Ghosh, P., Eiler, J.M., 2006. Preferential formation of ^{13}C - ^{18}O bonds in carbonate minerals, estimated using first-principles lattice dynamics. *Geochim. Cosmochim. Acta* 70, 2510-2529.
- Schleicher, A.M., Tourscher, S.N., van der Pluijm, B.A., Warr, L.N., 2009. Constraints on mineralization, fluid-rock interaction, and mass transfer during faulting at 2-3 km depth from the SAFOD drill hole. *J. Geophys. Res.* 114, B04202.
- Schleicher, A.M., van der Pluijm, B.A., War, L.N., 2010. Nanocoatings of clay and creep of the San Andreas fault at Parkfield, California. *Geology* 38, 667-670.
- Sleep, N.H., and Blanpied, M.L., 1992. Creep, compaction and the weak rheology of major faults. *Nature* 359, 687-692.
- Sibson, R.H., 1990. Conditions for fault-valve behavior. *Geol. Soc. Lond. Spec. Pub.* 54, 12-28.
- Sibson, R.H., 1992. Implications of fault-valve behavior for rupture nucleation and recurrence. *Tectonophysics*, 211, 283-293.
- Suchecki, R.K., Land, L.S., 1983. Isotopic geochemistry of burial-metamorphosed volcanogenic sediments, Great Valley sequence, northern California. *Geochim. Cosmochim. Acta* 47, 1487-1499.

- Swanson, E.A., Wernicke, B.P., Eiler, J.M., Losh, S., 2012. Temperatures and fluids on faults based on carbonate clumped-isotope thermometry. *Am. J. Sci.* 312, 1-21.
- Thordsen, J.J., Evans, W.C., & Kharaka, Y.K., 2010. Geochemistry of formation fluids from the SAFOD wells, Parkfield, California. *Eos Trans. AGU, Fall Meet. Suppl.* Abstract T41A-2098.
- Thordsen, J.J., Evans W.C., Kharaka, Y.K., Kennedy, B.M., & van Soest, M., 2005. Chemical and isotopic composition of water and gases from the SAFOD wells: implications to the dynamics of the San Andreas Fault at Parkfield, California. *Eos Trans. AGU, Fall Meet. Suppl.* Abstract T23E-08.
- Thompson, J.M., & White, L.D., 1991. Chemical analysis of water from the GTA-1 well, Parkfield, California, and other nearby spring and well waters. *USGS OFR 91-0003.*
- Titus, S.J., Dyson, M., DeMets, C., Tikoff, B., Rolandone, F., Bürgmann, R., 2011. Geologic versus geodetic deformation adjacent to the San Andreas fault, central California. *Bull. Geo. Soc. Am.* 123, 794-820.
- Vrolijk, P., and van der Pluijm, B.A., 1999. Clay gouge. *J. Struct. Geol.* 21, 1039-1048.
- Wiersberg, T., and Erzinger, J., 2008. Origin and spatial distribution of gas at seismogenic depths of the San Andreas Fault from drill-mud gas analysis. *Appl. Geochem.* 23, 1675-1690.
- Wiersberg, T., and Erzinger, J., 2011. Chemical and isotope compositions of drilling mud gas from the San Andreas Fault Observatory at Depth (SAFOD) boreholes: Implications on gas migration and the permeability structure of the San Andreas Fault. *Chem. Geol.* 284, 148-159.
- Wintsch, R.P., Cristoffersen, R., Kronenberg, A.K., 1995. Fluid-rock reaction weakening of fault zones. *J. Geophys. Res.* 100, 13021-13032.

- Wood, J.R., Boles., J.R., 1991. Evidence for episodic cementation and diagenetic recording of seismic pumping events, North Coles Levee, California, U.S.A. *Appl. Geochem.* 6, 509-521.
- Wycherly, H., Fleet, A., Shaw, H., 1999. Some observations on the origins of large volumes of carbon dioxide accumulations in sedimentary basins. *Mar. and Petrol. Geol.* 16, 489-494.
- Zheng, Y.-F., 1993. Calculation of oxygen isotope fractionation in hydroxyl-bearing silicates. *Earth Planet. Sci. Lett.* 120, 247-263.
- Zoback, M.D., Zoback, M.L., Mount, V.S., Suppe, J., Eaton J.P., Healy, J.H., Oppenheimer, D., Reasenber, P., Jones, L., Raleigh, C.B., Wong, I.G., Scotti, O., Wentworth, C., 1987. New evidence on the state of stress of the San Andreas fault. *Science* 238, 1105-1111.
- Zoback, M.D., Hickman, S.H., Ellsworth, B., 2010. Scientific drilling into the San Andreas fault zone. *Eos: Transactions of the American Geophysical Union* 91 (22), 197-199.
- Zoback, M.D., Hickman, S., Ellsworth, W., SAFOD Science Team, 2011. Scientific drilling into the San Andreas Fault Zone - An overview of SAFOD's first five years: *Scientific Drilling*, no. 11, 14-28.

Fig. 1. Geologic setting of the SAFOD drilling site and the studied deforming zones.

(a) The SAFOD borehole is located just north of Parkfield, California, at the transition between a creeping segment of the fault to the north and a locked segment of the fault to the south. (b) Generalized cross-section with the borehole geometry (modified from Bradbury et al., 2011 and Mitterpergher et al., 2011). Major faults intersected include the Buzzard canyon fault (BCF) and the two active traces of the SAF. Circles containing an X indicates plate motion away from the reader and circles containing a dot indicates plate motion towards the reader. (c) Downhole geophysical logs showing the low velocity damage zone containing both the “Southern Deforming Zone” (SDZ) and “Central Deforming Zone” (CDZ) (Zoback et al. 2010). Samples in this study come from both

Phase II cuttings (open circles) and Phase III core (filled circles) from about 3186 to 3945 meters measured depth (MD). The depths shown here, and on all other figures, are for phase 3 drilling and do not agree with phase 2 drilling depths. Phase 2 drilling depths can be calculated by (1) subtracting 5.03 m from runs 1-3, and (2) adding 3.96 m to runs 4-6 (Zoback et al., 2010).

Fig. 2. $\delta_{18}\text{O}$ and $\delta_{13}\text{C}$ values of carbonate veins and host rocks from the SAFOD borehole *cuttings* and *drillcores*. (a) The isotopic composition of the samples cluster into three populations. (shown as I, II, and III). (b) $\delta_{18}\text{O}$ and $\delta_{13}\text{C}$ values of carbonate veins and host rock *cuttings* plotted as a function of depth. In general, vein samples with low $\delta_{18}\text{O}$ are not in oxygen isotope equilibrium with their host rocks consistent with precipitation from, or exchange with, an externally-derived fluid. Populations I (grey boxes) and III are shown. All stable isotope values are reported in per mil relative to Vienna Pee Dee Belemnite (VPDB).

Fig. 3. Stable isotope and temperature data for calcite veins and host rocks obtained from the SAFOD borehole plotted as a function of depth. See Fig. 2 for symbol identification. Error bars are standard error (1 SE) for temperature. Data are also shown on a photo of a serpentinite clast from the “Southern Deforming Zone” (SDZ) (Zoback et al., 2010) section of the Phase III core.

Fig. 4. Plots of the O- and C-isotopic composition of waters, CO_2 and CH_4 (see Fig. 2 for symbol legend) that would be in isotopic equilibrium with calcite veins at present-day borehole temperatures or measured clumped isotope temperatures. Grey triangles represent the measured isotopic values of modern groundwater, well waters and oil field brines (Thompson and White, 1991), SAFOD borehole waters (Thorsden et al., 2005; 2010), SAFOD borehole mud gas CO_2, CH_4 (Wiersberg and Erzinger, 2008; 2011), Parkfield soil CO_2 (Lewicki et al., 2003). Dashed and solid lines represent the extrapolated equilibrium isotopic fractionations of water buffered by various minerals: quartz (Margaritz and Taylor, 1976); serpentinite (Barnes et al., 2013); illite-smectite (Suchecky and Land, 1983); and carbonates (Pili et al, 2011). Values for $\delta_{18}\text{O}$ are reported in per mil relative to Vienna Standard Mean Ocean Water.

Fig. 5. The measured and calculated $\delta_{18}\text{O}$ values for a subset of veins and parent fluids (filled circles, see Fig. 2) as a function of temperature. These values are compared to the predicted $\delta_{18}\text{O}$ evolution for fluids and veins during both closed-system (rock-buffered) and open-system (fluid-buffered) heating. Modern $\delta_{18}\text{O}$ water for spring and well waters (Thompson and White, 1991) and SAFOD borehole fluids (Thorsden et al., 2005; 2010) are shown (grey triangles). Lines are contoured for water-to-rock ratio (W/R, weight %) for carbonates (red lines) and waters (blue lines). The data are consistent with vein precipitation from evolved meteoric fluids in a rock-dominated system with W/R from about 0.01 to 0.25.

Fig. 6. Model of fluid flow near the two actively deforming traces of the San Andreas Fault. (a) Cross-section of San Andreas Fault, modified from Thayer and Arrowsmith (2005), illustrating possible fluid/gas sources and migration pathways. (b) Episodic fracturing stage with gouge seals intact: Optimally oriented fractures open and introduce fluids into the damage zones proximal to the SDZ and CDZ. $\delta_{18}\text{O}$ and $\delta_{13}\text{C}$ values are

consistent with infiltration of meteoric fluids (blue shading and arrows) along the damage zone associated with the SDZ to ~3194 m MD, and evolved meteoric fluids or basin brines (red arrows and shading) NE of the CDZ. (c) Local fracturing stage allows crossfault fluid flow: Water-rock chemical disequilibrium promoting formation of illite-smectite and metal oxides on newly formed fracture surfaces. Possible improved flow of mantle volatiles hydrocarbons. (d) Fracture sealing stage that reestablishes permeability barriers at the gouge zones: Fractures become occluded and compartmentalize the fault zone. Rock-dominated system favors replacement of K-feldspar and illite by chlorite-smectite. Continued local production of hydrocarbons creates a reducing environment leading to the precipitation of metal-sulfides. Diffusion of mantle volatiles and hydrocarbons is likely restricted to permeable country rock in the North American Plate and local zones of enhanced permeability during both the pre-seismic and inter-seismic periods consistent with the observations of Kennedy et al. (1997) and Wiersberg and Erzinger (2011).

Fig. 1

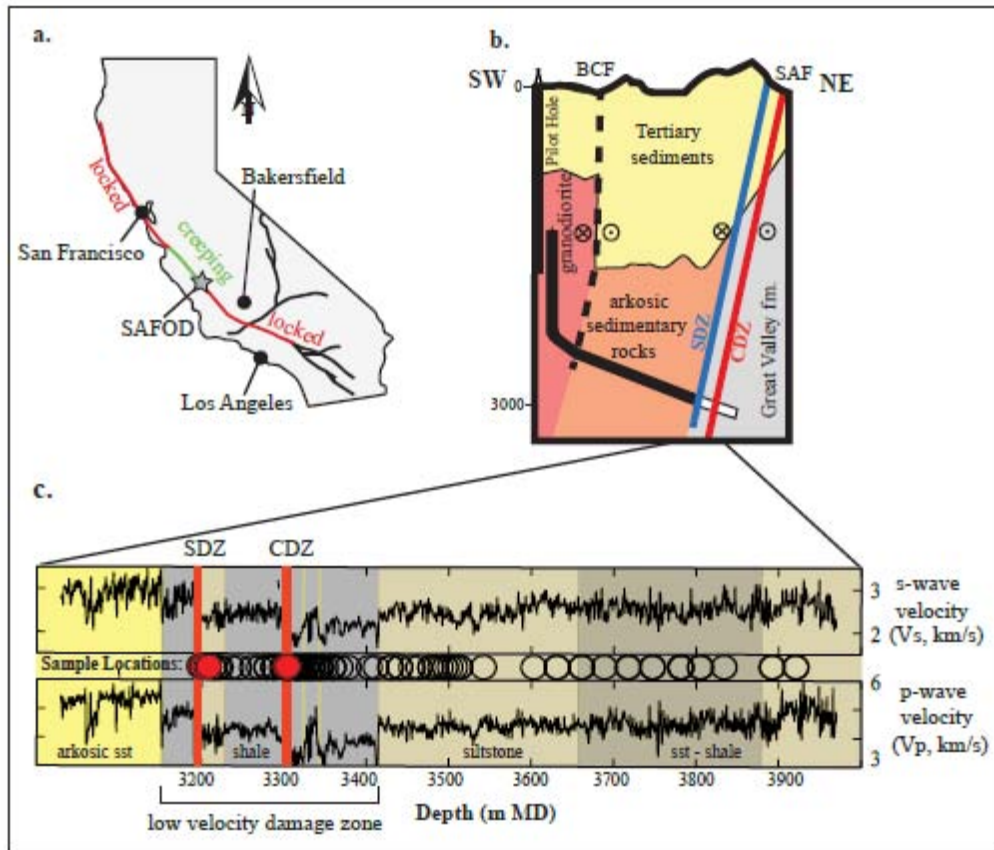


Fig. 2

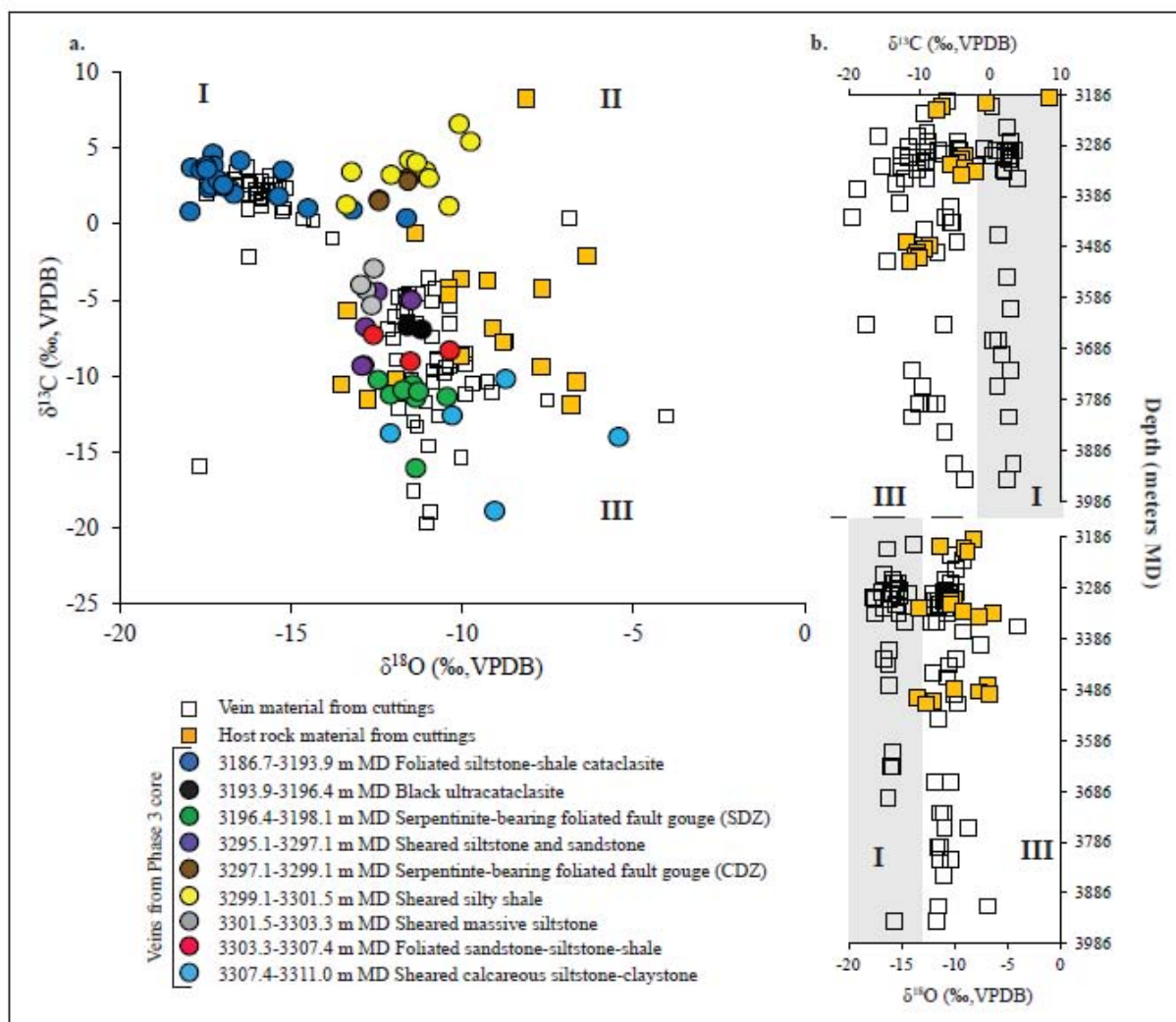


Fig. 3

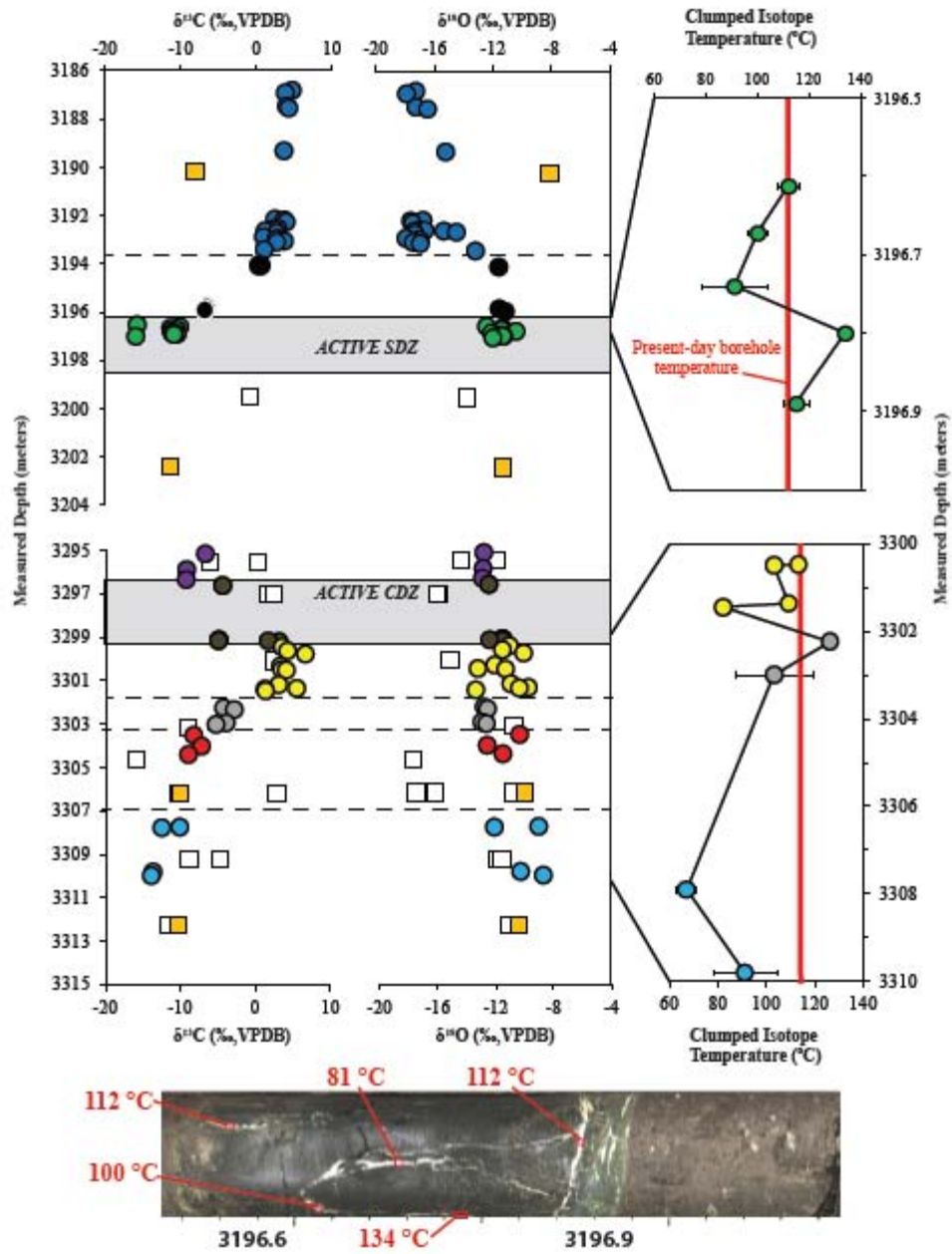


Fig. 4

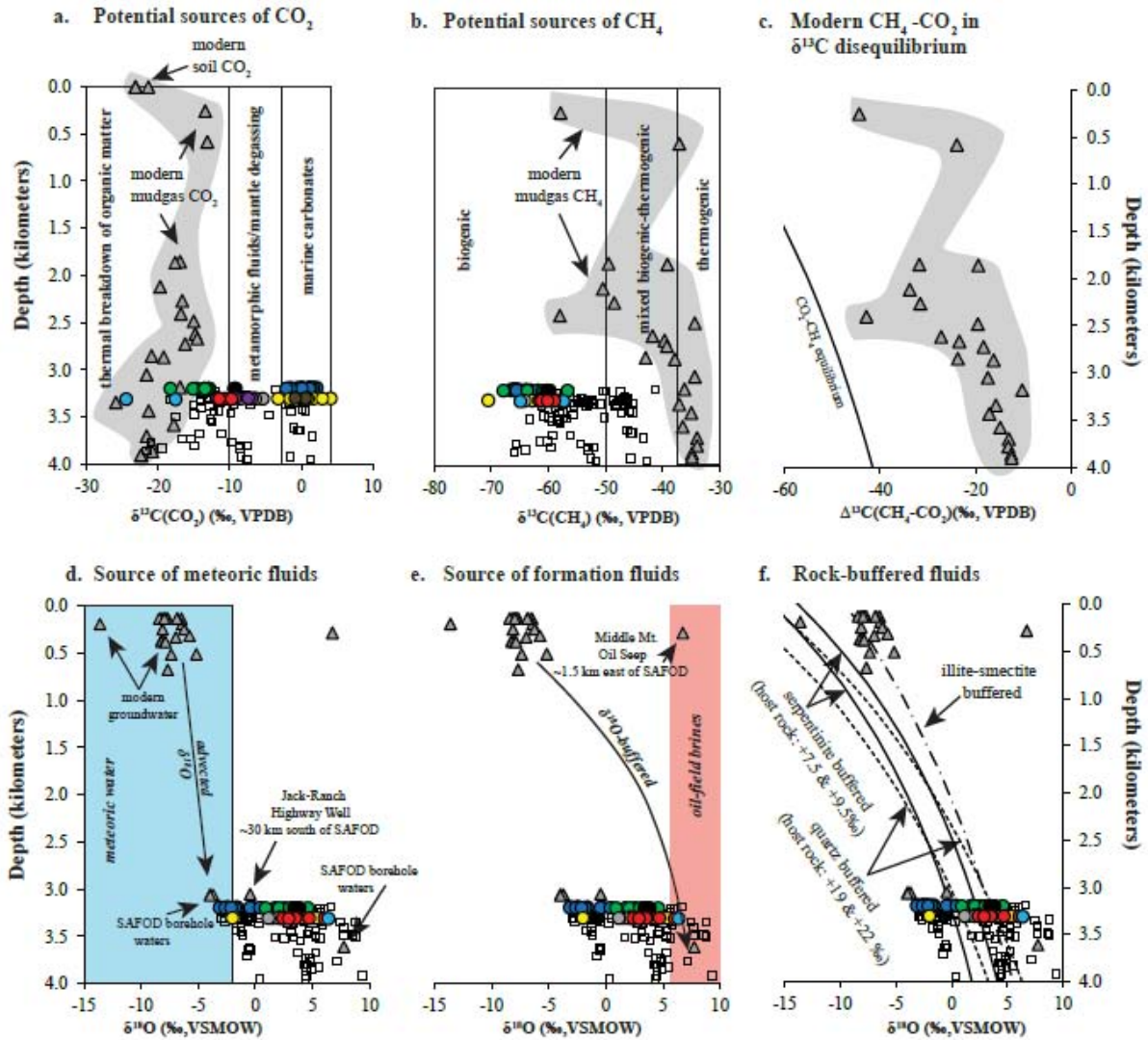
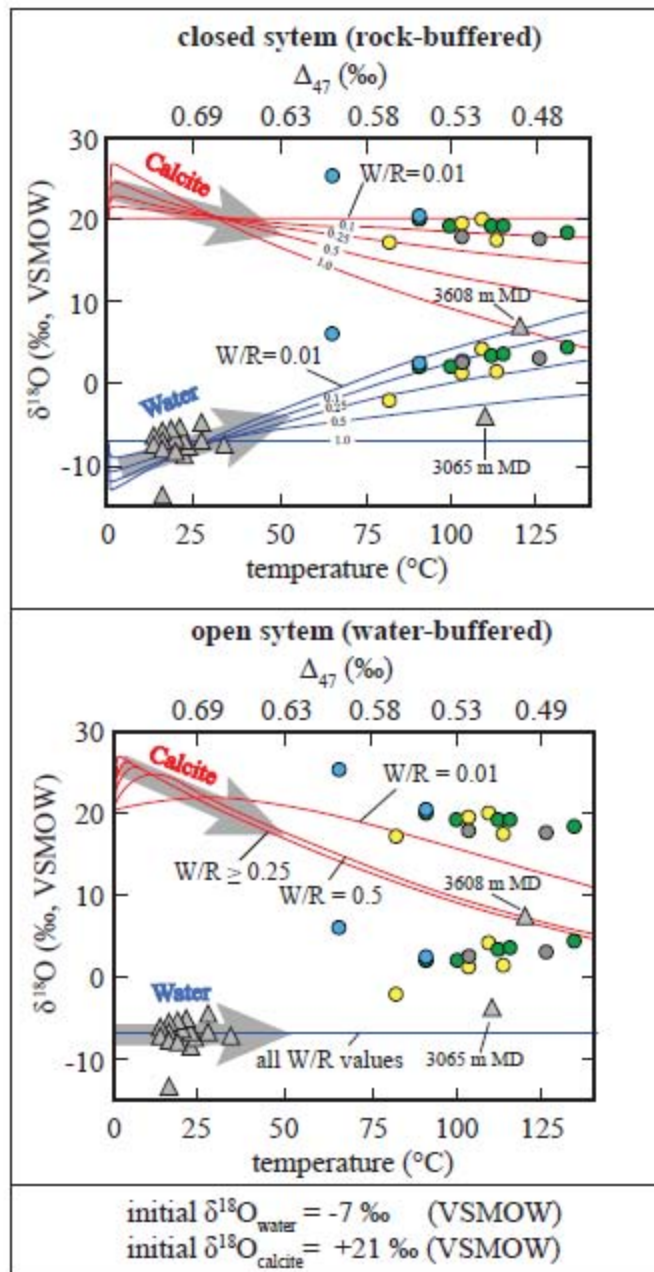
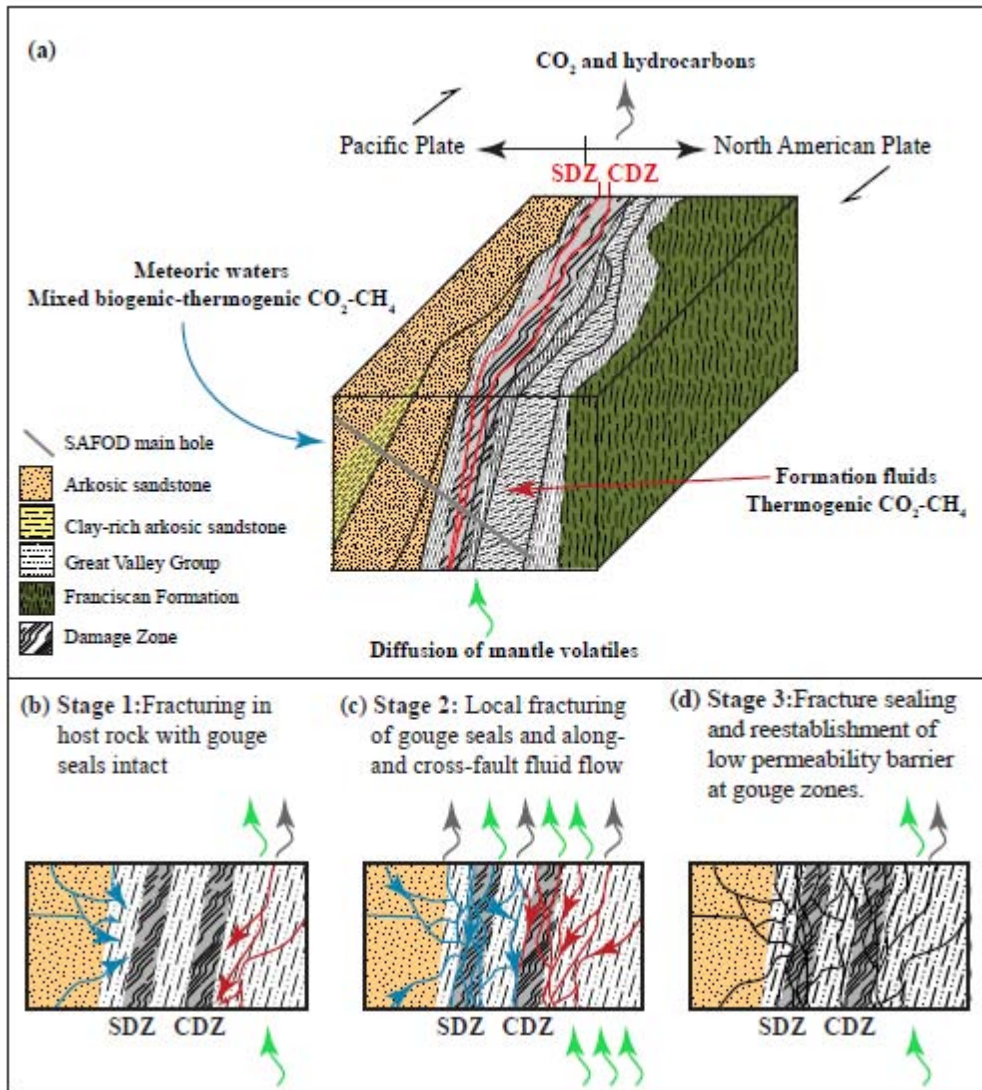


Fig. 5



SCRIPT

Fig. 6



ACCEPTED MANUSCRIPT

- Clumped-isotope thermometry of calcite veins of the SAFOD borehole..
- Calcite vein growth temperatures vary from 81 to 134 °C.
- Infiltration of meteoric fluids into actively-deforming zones.
- Meteoric fluids could favor formation of low-strength phyllosilicate fault rocks.

ACCEPTED MANUSCRIPT